NTNU
Det skapende universitet

Nanomekanisk prøving av stål

Er mindre alltid sterkere?

Veronica Gausel Haugen

Produktutvikling og produksjon
Innlevert: Juni 2012
Hovedveileder: Christian Thaulow, IPM
Medveileder: Odd Magne Akselsen, SINTEF

Norges teknisk-naturvitenskapelige universitet
Institutt for produktutvikling og materialer

Problemtext

MASTER THESIS SPRING 2012
FOR
STUD.TECHN. VERONICA GAUSEL HAUGEN
NANOMECHANICAL TESTING OF STEEL
Nanomekanisk prøving av stål

Nanomechanical testing of materials open up for new insight into the local material properties and gives also a tool to fundamental understanding of how specimen size/nanocompression will influence upon the test results. The testing of iron and steel is performed by machining pillars with Focused ion Beam and subsequently perform compression testing with nanoindentation equipment. The candidate has gained much experience with this kind of testing during her project work, and she has developed advanced experience in the selection of appropriate parameters for FIB. The Master thesis continues on the project work, and three steel-systems have been selected for the investigations:

1. Further investigations of the MA phases of the F70 steel
   Downsize the pillar: To he sure that the desired MA-particle is captured within the pillar, without being affected by particles from the matrix, and reduce the possibility of interstitial impurities, the pillar diameter should he reduced to a minimum. The minimum diameter should he estimated in collaboration with the size effect, so that the possible size effect is taken under consideration. During this project. tour small sized pillars were fabricated. The diameter range from 100 to 200 nm. They were not tested in the nanoindenter, because they buckled on the way from the FIB to the Indenter. But the results is promising. and indicates the pillar sizes down to 100 nm are within reach.

2. Pure iron
   Pure iron test material will soon he available, and will he a very interesting material for understanding the fundamental mechanisms and to compare the testing with atomistic modeling. One interesting parameter is the size effect. Is small always strongest?
   At a critical diameter of the pillar, the Frank Reed source will not have enough volume to produce multiple dislocations. When an initiated dislocation is arrested by a free surface, before it has enclosed and moved out of the source, the hardening of the material is activated by the phenomenon of dislocation starvation. This process requires an increased

stress field, due to initiation of new dislocations before the previous dislocation has been enclosed. Below this critical diameter, the yield strength increase rapidly. The critical diameter should he investigated from 100nm - 5um

3. High strength steels for automotive
   Through an EU project we have received trial batches of very high strength steels ftr the future cars. The main task in the project is to understand the degradation mechanisms with respect to hydrogen, but the first step will he to quantify the nanomechanical properties without hydrogen charging. Four steels have been selected, with a clear microstructure and alloying with and without Ti and Nb. The steels have about 50% ferrite and 50% martensite and will he good candidates to he compared with the MA phases and the pure iron.

The thesis should include the signed problem text, and he written as a research report with summary both in English and Norwegian, conclusion, literature references, table of contents, etc. During preparation of the text, the candidate should make efforts to create a well arranged and well written report.
To ease the evaluation of the thesis, it is important to cross-reference text, tables and figures. For evaluation of the work a thorough discussion of results is appreciated.
Three weeks after start of the thesis work, an A3 sheet illustrating the work is to he handed in. A template for this presentation is available on the IPMs web site under the menu Undervisning. This sheet should he updated when the Masters thesis is submitted. The thesis shall he submitted electronically via DAIM, NTNUs system for Digital Archiving and Submission of Masters thesis.

Contact persons
Bjørn Rune Sørås Rogne, NTNU
Odd M Akselsen, SINTEF/NTNU

Torgeir Welo
Head of Division

Navn på faglærer
Professor/Supervisor

Abstrakt

Gjennom dette arbeidet, er nanomekaniske kompresjonsegenskaper undersøkt for tre forskjellige materialer: To stål legeringer og et renjern. Pilarer av varierende størrelse, fra diameter 100nm til 2um, er fabrikkert ved bruk av FIB (Focused Ion Beam) i NTNU Nanolab, etterfulgt av kompresjonstesting. Hvorvidt størrelsen til pilarene påvirker de mekaniske egenskapene, er gjennomgående undersøkt for alle tre materialene, med spesielt hovedvekt på en-krystall renjern. Small is Stronger, er et velkjent utsagn i den sub-micro skalerte verden, og er diskutert videre her for hvert materiale.

F70 er en arktisk multifase ståltype, hvorpå lokale egenskaper i korngrense og matrix er undersøkt. Lokale soner i dette stålet er korngrenser bestående av MA-partikler (Martensitt og rest-Austenitt) og matriksen, som består av fraksjoner av bainitt, martensitt, feritt og rest-austenitt. Stålet er varmebehandlet i to sykluser for å simulere ICCGHAZ i sveisesoner, hvorpå avkjølingshastigheten i temperatureintervallet $\Delta T_{8/5}$ er satt til 5 sekund for en prøve, og 10 sekund for en annen prøve. Avkjølingshastigheten avgjører således de bruddmekaniske egenskapene, som er undersøkt ved nanomekanisk kompresjons testing. Pilar størrelsen er 250nm, 450nm og 1um. Resultatet indikerer at 5 sekunds prøven utviser høyere styrke og seighet. Størrelseseffekten er ikke fremtredende før en kritisk pilar diameter på 250nm er nådd. Dette stålet er undersøkt som en del av prosjektet Arctic Materials Group på SINTEF.

Et to-fase stål bestående av martensittkorn i en matriks av feritt, er undersøkt som en del av EU-prosjektet ved NTNU. To forskjellige prøver er undersøkt, hvorpå forskjellen skyldes legeringsinnhold av 0.05wt% Nb i den ene prøven, og ingenting i den andre. Legeringselementet øker både duktile egenskaper og styrken, på grunn av finfordelte utfellinger av karbider og redusering av kornvekst. Single-slip orienteringen (5 2 11) i feritt fasen er i hovedfokus, men martensitt fasen er også undersøkt. Fra resultatene kan det konkluderes med at innhold av Nb hever styrken og duktiliteten til materialet markant. Pillar diameter testet er 500nm og 1um. Størrelseseffekten kan ikke påvises eller avkreftes, da det ikke er undersøkt nok pilar størrelser til å trekke en absolutt konklusjon.

Tre forskjellige orienteringer av 99.998% rent bcc-Jern er undersøkt: Multi-slip orientering (111) og (110), sammen med en single-slip orientering (235). Hovedfokuset ligger i å undersøke størrelseseffekten av en-krystall bcc-Fe, og om effekten av single-slip i forhold til multi-slip systemer påvirker resultatene. Kompresjons testing avslører at det er en fremtredende størrelseseffekt

tilstede i alle tre orienteringer. Styrken til (111) orienteringen er høyere jevnt over sammenlignet med de to andre orienteringene, selv om størrelseseffekten er mest fremtredende i (235). Den økte styrken som de minste pillarene utviser, er således ikke påvirket av mengden av tilgjengelige slip-systemer. En beskrivende ligning for størrelses-effekt sensitiviteten er $\tau = D^{-n}$, hvor størrelsen på n indikerer sensitiviteten. For dette renjernet ligger verdien av n i samme området som for fcc metaller, altså en markant størrelseseffekt. Skjønt, er deformasjons mekanismen i fcc og bcc grunnleggende forskjellige. Den observerte styrkeøkningen, konkluderes å være forårsaket av atermale prosesser, eller ved skru-dislokasjoners grad av mobilitet. Pilar størrelsen varierer fra 100nm, 500nm, 1um og 2um. Det kan derfor konkluderes med at det er en sterk størrelse effekt i bcc-Fe.

For å kunne forstå de lokale egenskapene i komplekse mikrostrukturer, er det først og fremst avgjørende å forstå deformasjonsmekanismen i rene en-krystaller. En god teori for plastisk deformasion på sub-mikro nivå er fremdeles ikke fremkommet og validert både eksperimentelt og data simulert. Når dette skjer, kan man være i stand til å forstå effekten av komplekse gitterstrukturer og legeringsinnhold, på nanomekaniske plastiske egenskaper. Med andre ord, man må tilnærme seg problemet fra en bottom-up perspektiv. Koblingen mellom datasimuleringer og eksperimentell testing på sub-mikronivå, må gjøres sterkere. Inntil dags dato, er mye av dette universet fremdeles uutforsket, og kun mindre forstått. Derfor kan du bruke denne oppgaven som ditt springbrett inn i verden av nanoskalerte materialeventyr!

Abstract

In the present work, three different materials have been investigated due to nanomechanical compression properties: Two alloying types of steel and one pure bcc-Fe. Pillars of varying diameter, 100nm to 2um, are fabricated with FIB, followed by compression testing with a nanoindenter tip. The size effect is also investigated, for which statement Small equals Strong is discussed for each material.

F70 steel is a multi phase forged material. Local properties are investigated. Local zones are grain boundaries of MA-phases and a matrix consisting of fractions of bainite, martensite, ferrite and retained austenite. The steel is heat treated in two cycles with two different cooling rates, $\Delta T_{8/5} = 5$ sec and 10 sec, to simulate the ICCGHAZ of weldings. The fracture mechanical effect of the two different cooling rates is investigated by nanomechanical compression testing. Pillar sizes range from 250nm, 450nm to 1um. The compression result indicate that the 5 sec sample exhibit higher strength and toughness. The size effect is not prominent until a critical pillar diameter of 250nm is reached. This steel is investigated as a part of the project Arctic Materials Group at SINTEF.

Two different samples of the Dual Phase steel from the EU project at NTNU, consisting of martensite and ferrite, is investigated. The sample difference is due to an alloying amount of 0.05wt%Nb in one of the samples, while the other one is free of Nb. This alloying element increase both the ductile properties and strength, due to fine dispersiod carbides and grain refinement. The single slip orientation (5 2 11) in the ferrite phase is the main focus, although the martensite phase is also investigated. From the present compression test results, it can be concluded that content of Nb is the superior alloying composition, due to mechanical properties. Nb5 is far more ductile, and shows higher yield strength. Pillar diameter range from 500nm to 1um. The presence of any size effect can though not be confirmed or disproved due to few sample sizes.

Three different orientations of 99.998% pure bcc-Fe is investigated: Multi slip orientations (111) and (110), together with the single-slip orientation (235). The main focus is to investigate the size effect of single crystal bcc-Fe, and if the effect of single slip or multi slip affects the results. Compression testing reveals that there is a prominent size effect present in all three orientations. The increased strength at small pillar sizes is thus not affected by the amount of available slip systems. The fitting curve power exponent n approaches that for fcc metals, though, the deformation mechanism in fcc and bcc is fundamental different. The observable strength increase

is concluded to be caused by athermal processes, or by the mobility of screw dislocations. The pillar sizes varies from 100nm, 500nm, 1um and 2um. It can thus be concluded that there is a strong size effect in bcc-Fe.

To be able to understand the local properties of complex microstructures, it is first of all crucial to understand the deformation mechanism in pure single crystals. As a proper theory can be opposed and validated both experimentally and simulated, the effect on mechanical properties, due to a material composition of different lattice structures and alloying elements, can be evaluated. In other words, one needs to approach the problem from a bottom-up perspective. The link between computational simulations and experimental testing at sub-micro level needs to be stronger. To the present day, much of this universe is still unexplored and just slightly understood, at which you can use this thesis as your platform and jump into the world of nanoscale adventures!

A huge appreciation and thanks goes to PhD. Bjørn Rune Rogne and PhD. Adina Basa, who has helped me with absolutely everything from being a good discussion partner, asking the good questions, set up instruments and build up guide lines. Dr.Christer Ersland has done computer simulations which are used in this thesis. My supervisor Prof. Christian Thaulow for just being him and all his ideas and innovative thinking which is very inspiring. Post Doc. Afroos Barnoush, in the participatio of the EU project, and his clever ideas and concerns about EBSD. Senoir Scientist Odd Magne Akselsen and Scientist Erling Østby for their participation in the Arctic Material Group, and for inspire and guide my working progress. Prof. Wilhelm Dall also needs to have a thank because of his good mood and his EBSD knowledge.

Contents

Chapter 1

Introduction

While dislocation motion in crystals is known as the fundamental mechanism of plastic deformation under a wide range of conditions, a quantitative connection between the collective dynamics of dislocations and the plastic strength of the crystal is still lacking. For bulk crystals, plastic strength such as flow stress can be measured experimentally and considered as a size-independent material property. However, as the size of the material decreases to micro and nano scales, the measured plastic strength is found to be size dependent, hence the size effect.

Several nanocompression tests of FIB fabricated single crystal pillars have shown a strength dependency due to the pillar size. The dependency can be fit to a power law,

$$\tau_{CRSS} \propto D^n, \tag{1.1}$$

where the exponent n describes the size effect dependency. Both theoretical, experimental and simulations have been done to investigate the cause of this observed size effect. By analyzing the stress-strain response subsequent to compression, as well as the deformation morphology for single slip and multiple slip systems in bcc-Fe, the effect of orientation is investigated due to the size effect. Do this power law fit also to pillars of a more complex alloying microstrucure?

It is the defects in the materials which often give rise to most of the important and interesting properties. How do material deform and react under very severe inviornment? Under what condition is the material ductile and when does it transform to a brittle behavior? And what causes this transition?

One of the underlying principles in materials science is that properties can be deduced from a knowledge of the microstructure. By microstructure we mean the crystalline structure and all imperfections, including their size, shape, orientation, composition, spatial distribution, etc. A list of the types of imperfections would include point defects (vacancies, interstitial and substitutional solutes and impurities), line defects (edge and screw dislocations) and planar defects (stacking faults, grain boundaries), second phase particles and dispersoids or relatively large amounts of other phases. With so many factors to consider it would seem that finding this structure-properties relationship would be impossible. But selecting the type of material to use

in the study (pure/alloy, single crystal/polycrystalline, single/multi-phase) one can eliminate many factors and concentrate on the ones of interest. In this work, a single-crystal bcc-Fe is used in the investigation of the influence of sample size on mechanical properties. The small-scale well-known statement: Smaller is Stronger is a red line throughout this thesis, whereby the mechanical properties of a multiphase arctic steel, as well as a dual phase automobile alloying steel is investigated. The main focus is based on experimentally observed mechanical properties due to plastic deformation. Other important concerns are the relationship between sample size and yield strength, the alloying components, the effect of heat treatment, the microsturcure and also considerations and suggestions based on proposed plastic deformation theories at sub-micro level found in literature.

Regarding features of plasticity, BCC lattice structure and Martensite is mainly in focus in the present paper, as BCC (α-Fe) is a component within all three materials investigated, and martensite is a component of two materials investigated.

Chapter 2

Theoretical background

2.1 Continuum versus Discrete Plasticity Theory

When explaining the nature of plastic deformation at macro scale, the materials are viewed as rigid bodies. Several well-established plastic theories are simple, and can only predict features of the material behavior in a limited length scale. Physically, all materials consists of vibrating molecules and atoms and even smaller particles. Thus all materials are discrete in nature. When the volume scale or dimension of the considered material is large, compared to that for molecules and atoms, the discrete nature of the material is ignored, as in classic plasticity theory. The considered material is treated as a continuum body, consisting of particles distributed continuously in space. This idealization of matter is thus called a continuum. In other words, continuum theory has a top-bottom aspect when regarding nature. That is to conduct a fracture mechanical analysis at macroscale, followed by proposing a theory explaining the situation at the micro scale. Complementary to the continuum plasticity theory, there is instead a bottom-up approach to the matter of nature and its features. This discrete theory can be called the crystal plasticity theory. The aim for this approach is to explain and describe theories at a microscopic scale, and thereby be able to link and predict material behavior at a macro scale. The problem is to come up with proper approximation procedures to be able to link the microscopic state variables to its macroscopic counterparts. One of the problems involved, is the strain hardening mechanism. As continuum plasticity use an approximation due to Kocks or Voce to describe plastic shearing, there are still few discrete theories describing the different stages of slip mechanism within the crystal due to its orientations and textures. Conventional continuum plasticity models assume that the stress at a point of the material, is a function of the state of strain at the same point. This assumption is adequate as long as the deformation field is larger than the local micro scale length of the material. Conventional theory are thus size independent, and unable to predict size-effects which are observed at experiments at micro- and nanoscale. However, when the two length scales, the deformation field and the grain size, are comparable in size, the continuum theory is questionable, because the material behavior at a point is influenced by the deformation of neighboring points ([**?**]).Though, the physical length scales that control the strengthening are not clearly established. Thus, discrete dislocation theory may be regarded as an effective compromise between linear-elastic dislocation theory and full atomistic simulations based on

empirical potentials.

In fig. 2.1, mechanical properties of a material is approached at different length scales; atomistic-, nano-, micro- and macroscale.

The gap between atomistic and nano/micro scale needs to be enclosed. If atomistic simulation could be verified experimentally at the nano/micro scale, the plastic deformation theory would be one step further to completed.

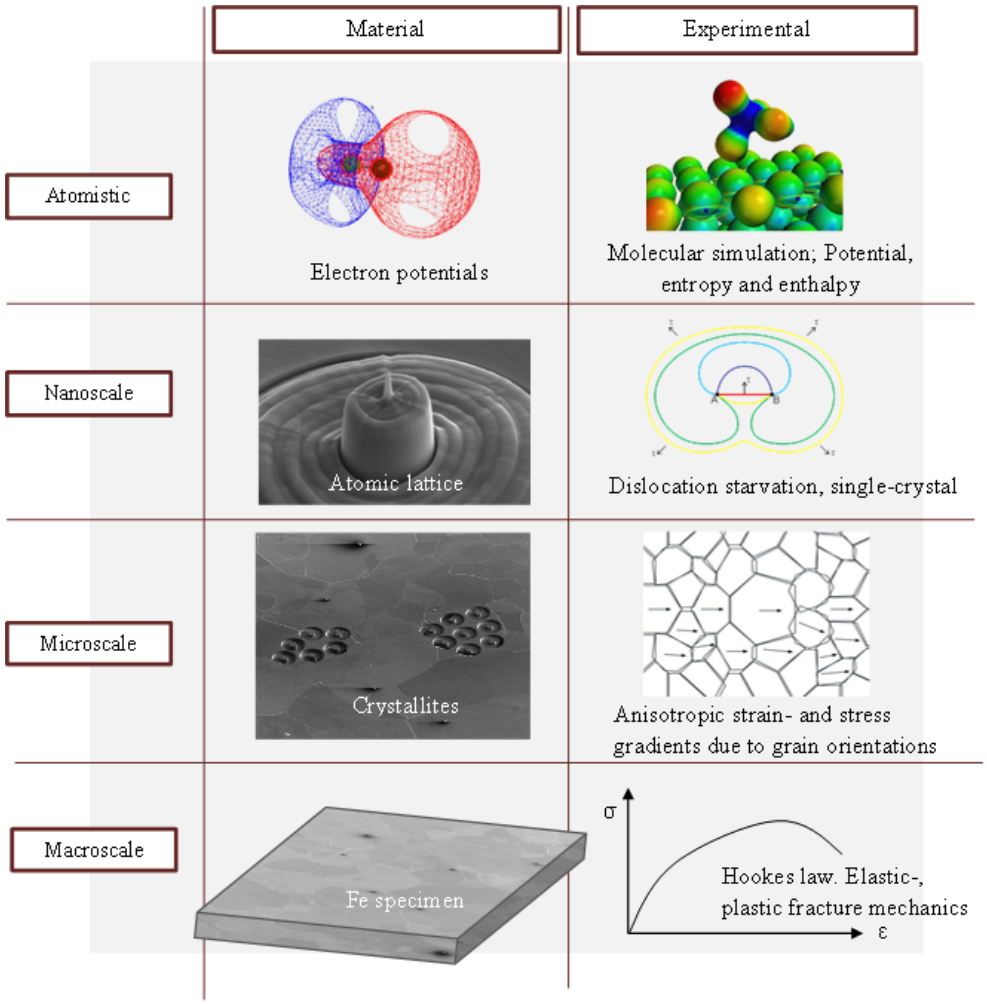

Figure 2.1: Multiscale modeling of material behavior

2.2 Single Crystal and Polycrystalline materials

The fundamental difference between a single crystal and a polycrystalline material is the length scale over which the atoms are related to one another by translational symmetry. Translational symmetry means the periodicity or long-range order of the atomic bonding structure. An ideal single crystal has an atomic structure that repeats periodically across its whole volume. A polycrystalline consists of many individual grains or crystallites. Each grain can be thought of as a single crystal, within which the atomic structure has long-range order. In an isotropic polycrystalline material, there is no relationship between neighbouring grains. Therefore, on a large enough length scale, there is no periodicity across a polycrystalline sample, despite the fact that each individual grain exhibits anisotropic features.

Single crystal
A single crystal often has distinct plane faces and symmetry. The shape of the crystal will be determined by the amount of crystallising material available, and by interference with other crystals. The angles between the faces will though be the main characteristic of the material and defines the ideal shape. The mechanical properties of a single-crystal is directionally dependent, due to anisotropy. While the strength of the lattice can be high in one direction, it can exhibit weakness in another direction. A single-crystal is formed by the growth of a crystal nucleus without secondary nucleation or impingement on other crystals.

Polycrystalline
A polycrystal is made up of many crystals. The properties are notably different from those of a single crystal. The properties of polycrystalline samples can be completely isotropic or strongly anisotropic depending on the nature of the material and the way in which it was formed. The individual crystallites are referred to as grains and the junctions between these grains are known as grain boundaries. Crystallization starts from a number of nuclei. These developing crystals grow until they meet. After crystallization, the solid tends to reduce the boundary area, and hence the internal energy, by grain growth. This can only happen by a process of atomic diffusion within the solid. Such diffusion is more rapid at a higher temperature since it is thermally activated. Thus the grain size of a polycrystalline can be controlled according to heat treatment, time and alloying elements.

Single- and Dual-phase
Materials like metal may consist of one, two or multiple different phases. An example of a single phase metal, would be α-iron, while a multiphase metal would be a combination of ferrite, austenite, martensite, bainite or perlite. The volume fraction of each phase controls its strength and plasticity properties. A dual phase material commonly experience a greater amount of strain hardening, than for what a single crystal do. This is because the two phases are not equally easy to deform. One component shows greater plastic deformation than the other, so that gradients of strain builds up at the interfaces between the phases, impeding line defects (dislocation lines) to move. By investigating properties of each individual phase, the interaction between the two phases can be understood, and then the macroscopical mechanical behavior can be described.

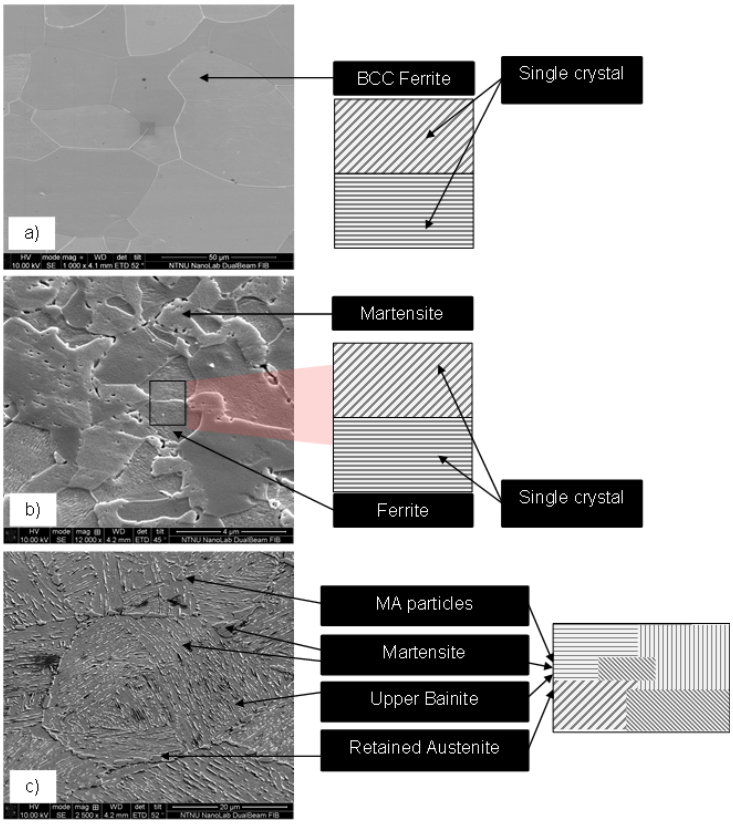

Figure 2.2: a) Pure Iron Sample: Single phase (BCC Ferrite) b) Nb5 Sample: Dual phase (Ferrite and Martensite) b) F70 Sample: Multiphase (Martensite, Retained Austenite, Bainite)

In fig 2.2 a), an SE image of a single phase iron microstructure is shown. At macro level, the specimen exhibit isotropic behavior, while each individual grain is anisotropic. The lattice structure is homogeneous and strictly aligned in different BCC orientations within each separate grain. The phase is ferrite. In b), an SE image of a dual phase steel (MutliHy Nb5) is shown. The microstructure is composed of ferrite and martensite grains, in which the crystallographic orientation within each (ferrite) grain is homogeneous. The individual grains can thus be considered as discrete single anisotropic crystals, though the material exhibit isotropic properties at a larger length scale. In c), a SE image of the F70 steel sample is shown. This is a multiphase material, composed of martensite, upper bainite and retained austenite. Within each high-angle grain, there are packets of different crystallographic orientations. Each packet is also multiphased, due to small islands of MA-particles. These grains are therefore not considered to be single crystals.

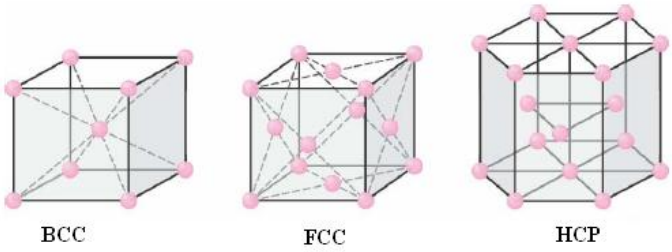

Figure 2.3: Unit cell geometries: Body Centered Cubic, Face Centered Cubic, Hexagonal Closed Pack

2.3 Planes, Directions and Poles

To understand the nature of material behavior, it is crucial to understand the effect of crystallographic orientations in relation to observed mechanical properties. The smallest possible part of crystal lattice, determining the structure, is called primitive unit cell. The unit cell can take on different geometries, see fig. 2.3.

Examples of materials which naturally exhibit BCC structure is Fe, V and Nb, FCC is Al, Ni and Cu and HCP is Ti, Zn and Mg. Different unit cell geometries contain a variable amount of available slip planes. Low Miller indicies planes exhibit multiple slip systems, while high Miller Indicies planes may contain only one single slip system.

Crystal Plane and Direction
A plane with Miller indices (hkl) passes through the three points (a/h,0,0), (0, b/k,0) and (0,0, c/l) on the edges of the unit cell, as shown in fig.2.4. The set of parallel lattice planes passes through all similar points in the lattice. In materials with cubic symmetry the crystal direction [uvw] and the normal to the plane (uvw) are parallel.The family of symmetrically related directions [uvw] is shown by the notation $\langle uvw \rangle$ and the family of symmetrically related planes (hkl) is shown by the notation {hkl}. A family of directions includes any directions that are equivalent in length and types of atoms encountered. For example, in a cubic lattice, the [100], [010], and [001] directions all belong to the $\langle 100 \rangle$ family of planes because they are equivalent. If the cubic lattice were rotated 90 °, the a, b, and c directions would remain indistinguishable, and there would be no way of telling on which crystallographic positions the atoms are situated, so the family of directions is the same. For the unit cell of BCC, there are no closed pack planes, as in FCC and HCP, but there is a closed pack direction, $\langle 111 \rangle$, as the linear atomic density is at a maxiumum in this direction. However, there are three types of planes with the highest packing density, which are nearly closed packed. They are {110}, {321} and {211}. Thus, the following slip systems in BCC crystals are:

- 6 {110} planes each with 2 $\langle 111 \rangle$ directions.
- 24 {321} planes each with 1 $\langle 111 \rangle$ direction.
- 12 {211} planes each with 1 $\langle 111 \rangle$ direction,

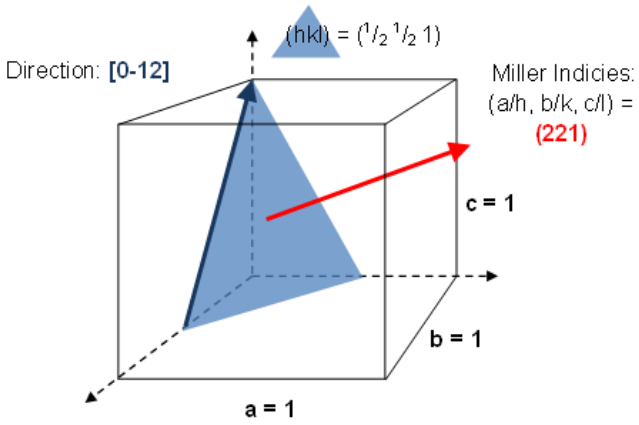

Figure 2.4: Crystal plane (221) and direction [0-12]

which in all gives a total of 48 slip systems for BCC crystals. Because there are so many available slip systems intersecting the ⟨111⟩ direction, there can occure cross-slipping (see section Dislocation Mechanism).

Crystallographic Poles

Directions in three dimensions can be represented in two dimensions with a stereographic projection. The sample normal is the center of the projection. If a unit cell with cubic symmetry is placed at the centre of the projection sphere, then the crystal directions and plane normals can be projected onto the equatorial plane and the directions represented as a stereographic projection, see fig. 2.5. In this figure, the one of the eight (111) plane normals are shown wihtin a BCC crystal, a). This plane normal corresponds to the projected blue point in the stereographic sphere, b). Because of crystal symmetry, an equal point would appear in each triangle, thus only one triangle is necessary to investigate. This inverse pole figure, c), thus corresponds to points of crystal orientations.

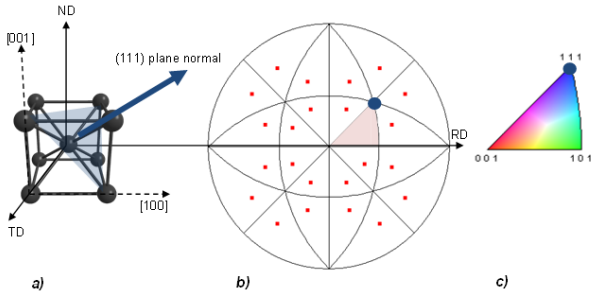

Figure 2.5: a) BCC (111) plane b) Stereographic projection sphere c) Inverse Pole Figure

2.4 Dislocation Mechanism

In a polycrystalline material, the grain boundaries act as pinning points impeding further dislocation propagation. Since the lattice structure of adjacent grains differs in orientation, it requires more energy for a dislocation to change directions and move into the adjacent grain. The grain boundary is also much more disordered than inside the grain, which also prevents the dislocations from moving in a continuous slip plane. Impeding this dislocation movement will hinder the onset of plasticity and hence increase the yield strength of the material. The central idea is that dislocations are forced to pile up at grain boundaries, either because there is a barrier to crossing over into the next grain, or because a source must be activated in the next grain.

A dislocation represents an obstacle in the packing order of the crystal. The atoms near the core of the dislocation are displaced from their thermal equilibrium positions and thus have a higher energy. In order to keep the total energy as low as possible, the dislocation tries to be as short as possible. When analyzing the strain fields near the dislocation, it can be found that the internal energy per unit length due to a dislocation is given as follows:

$$U = \frac{Gb^2}{2} = \frac{E}{2(1+v)} \tag{2.1}$$

The internal energy of a dislocation can be taught of as line tension. Dislocations are formed to minimize this energy. Since U is proportional to b^2, the burger vector, it is apparent that dislocations with minimum $\mid b \mid$ are the most stable. Thus, slip occurs along the plane of the shortest Burgers vector. This justifies why dislocations usually move in close-packed planes in close-packed directions. The amount of dislocation line segments will typically determine the strain hardening properties of the material. The volume density of these line segments, or dislocations, can be expressed as the total length of dislocations, divided by the containing material volume, or as the number of dislocations intersecting a unit area of a random section.

The burgers vector is a characteristic entity of a dislocation.

$$\mid b \mid = \frac{a}{2}\sqrt{h^2+k^2+l^2} \tag{2.2}$$

where a is the unit cell length of the crystal, $\mid b \mid$ is the magnitude of Burgers vector h, k, and l are the components of Burgers vector, b = $\langle hkl \rangle$.

There are two general types of line defects: Edge and screw dislocations. It is common that a combination of these two mechanisms appear in materials, and together with point defects, can cause a complex dislocation movement, which behavior is not yet easy to predict and simulate.

An edge dislocation introduces an extra half-plane of atoms mid way through the crystal, distorting nearby planes of atoms (see fig. 2.6).This makes the atoms above the dislocation line in compression, while the atoms below the line are in tension. When applied shear stress exceeds the atomic equilibrium bonding energy, this extra plane passes through planes of atoms by a distance b, Burgers vector, breaking incremental bonds and joining bonds with new atoms until it reaches the grain boundary. The energy required to break a single bond is far less than that

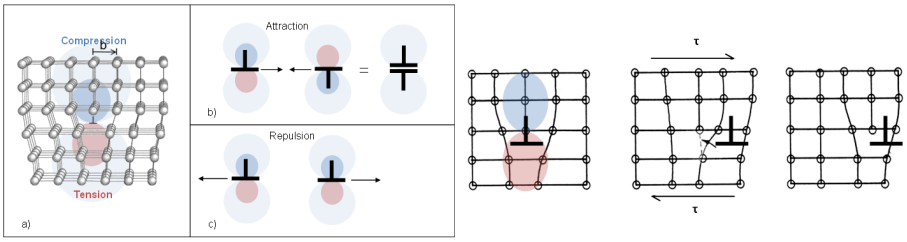

Figure 2.6: Edge Dislocation

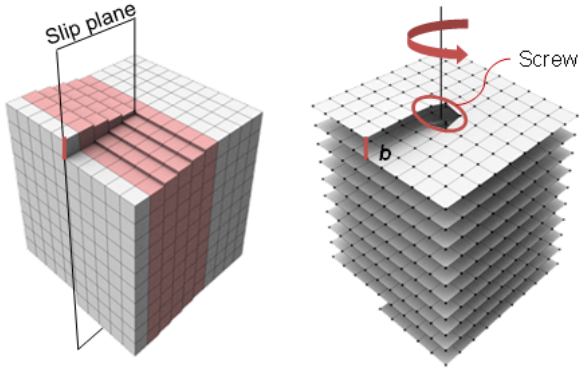

Figure 2.7: Screw Dislocation

required to break all the bonds on an entire plane of atoms at once. Thus, the movement of the line defect will not behave like it would theoretically do in a perfect crystal, where the whole slip plane would move one increment of a burger vector and join new bonds. The ideal strength of a material is the stress at which the lattice itself becomes unstable and, hence, sets a firm upper bound on the mechanical strength the material can have. In edge dislocation, burger vector is perpendicular to dislocation line, so there is only one plane in which the dislocation can slip.

For screw dislocations (fig.2.7), the Burgers vector lies in the direction of the dislocation line, so the dislocation may slip in any plane containing the dislocation. Therefore, it is comparatively easy for screw dislocations to change glide planes. The mechanism by which this happens is called cross-slip. In contrast to dislocations with an edge component of Burgers vector it takes place in a conservative way, that is, without having to add or subtract atoms at the dislocation core. As dislocations multiply they begin to pile up at obstacles. Internal stress rises, and eventually secondary slip systems get activated. Primary and secondary slip systems interact with themselves and with one another, thus the stress needed to produce additional plastic deformation rises. Finally, internal stress levels become high enough for large-scale cross-slip to occur. By this mechanism dislocations can escape from their locked positions, and screw dislocations of opposite sign meet and annihilate, reducing dislocation density and relaxing internal stress. By triggering secondary slip systems and therefore producing additional obstacles for the primary slip system, cross-slipping acts as an indirect hardening mechanism.

Cross- slip is thus the change from one slip plane to another, when the shear stress on the

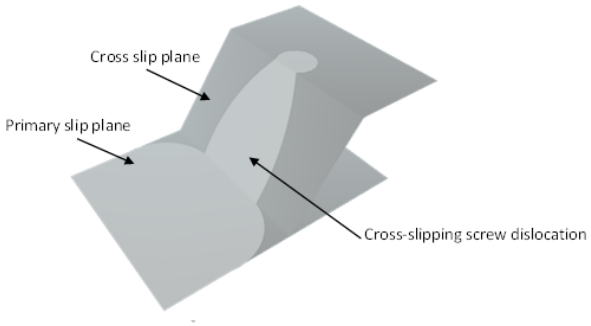

Figure 2.8: Cross-slip dislocation movement

second plane is sufficient to cause the dislocation to glide on it and the burger vector is equal. It is commonly observed BCC metals.

Among different obstacles for screw dislocations, the Lomer Cottrell dislocation (LC lock) is considered to be the most prominent factor. These sessile locks are investigated and found to be apparent in FCC crystals. It is not found to describe the mechanism in BCC crystals. LC locks are formed when two attractive dislocations moving on intersecting {111} FCC planes, combine. Since they can dissociate into the two intersecting {111} planes, they are sessile and form barriers impeding screw dislocations in {111} planes. Because LC locks are of pure edge character, which is not the prominent dislocation character found to dominate in bcc metals, it will not be considered and discussed further.

Within a single crystal or grain, the crystal structure is not perfect. The structure contains both point- and line defects. Crystal defects are important in determining many material properties, such as the rate of atomic diffusion and mechanical strength. Grain boundaries in polycrystals can be considered as line defects in the perfect crystal lattice, where the perfection of the structure is disrupted along a line. Grain size strengthening (or Hall Petch strengthening) is a method of strengthening materials by changing their average grain size. Grain boundaries impede dislocation movement. The amount of dislocations within a grain have an effect on how easily dislocations can traverse grain boundaries and travel from grain to grain. So, by changing grain size one can influence dislocation movement and yield strength. Obstacles impeding line defect movement, are point defects within the lattice structure. Point defects are vacancy, interstitials and impurity atoms:

- Vacancy - An atom is vacant in the long-range order lattice.
- Interstitials - an atom is locked inside the crystal at a point intermediate between normal lattice positions.
- Impurity - An atom of a foreign matter, which is present in the lattice, resulting in local disturbance.

Dislocation interaction with large incoherent particles depends on interparticle spacing. If an interparticle spacing is less than $\gamma = aGb/t$ (where a is constant, G is shear modulus, b is the

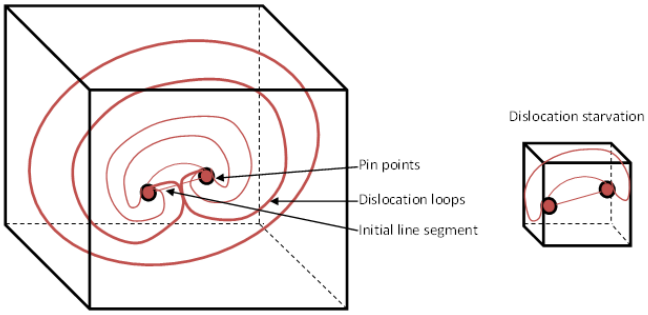

Figure 2.9: Frank-Read source: Left: Multiple dislocation loops. Right: Dislocation starvation

magnitude of the Burgers vector and τ is the applied shear stress), a dislocation will tend to move through the particles and finally bisect them. If an interparticle spacing is above γ, a dislocation will tend to bend between the particles and bypass them having left the particles surrounded by dislocation loops. Particle cutting will require increasing stresses with particle strength increase due to composition effect on interatomic bond strength and lattice type; and particle size increase, as particle coherency with the matrix generally decreases as particle size increases. In both cases the defect energy of crystal structure increases, either by increase in particle-matrix surface or total dislocation length. In terms of macroscopic deformation, to increase the internal energy, greater external loading is needed. Thus the yield stress increases due to precipitation of alloying elements.

A dislocation segment has to initiate from somewhere, either the free surface or from within the interior. Different initiation points are mentioned above, but what about if none of these obstacles are present?
Kink-formation at the free surface is found to initiate multiple dislocations within a bcc lattice. Another source is the well known Frank-Read source, which is anchored in two points in each end of the dislocation line segment. Its behavior looks like that of two single pole sources with opposite Burgers vectors which turn around their anchoring points. The dislocation segment first bows out between the pinning points, reaches a semi-circular shape and rapidly expands until the two opposite curves annihilate. The initial segment is restored, leaving a fresh dislocation loop in the slip plane. For a Frank-Read source to be able to multiply and thus increase strength within the material, enough material volume needs to be available. If the volume of the material is less than the initial dislocation line segment for which the source points are pinned, the dislocations can not enclose and expand, and will thus be arrested at an early stage by the free surface. The question is then, what causes strengthening in a material at the scales of less than the dislocation line segments? Several theories has been put forward these last years, concerning the plastic deformation mechanism in different lattice structures. Because FCC and BCC structures are fundamental different due to microstructural properties and mechanisms, different theories attributed to these structures are suggested.

Cottrell suggests that plastic deformation is the transition from an unslipped to a slipped

state by overcoming an energy barrier δE. This energy barrier is also called a Perierls barrier: The mobility of dislocations are highly dependent on the pinning mechanisms. Dislocations may be pinned by imperfections of the crystal structure (impurities, interstitials, vacancy etc). Though, even within a perfect crystal, there will exist barriers for dislocation motion, caused by the discreteness of their crystal lattices. These barriers are called Peierls barriers, which corresponds to the thermal energy required for a dislocation segment to overcome an obstacle at 0K. The magnitude of the line segment can be characterized by the Peierls stress, i.e. the resistance of the pinning point and crystal structure, per unit length of the dislocation line. As the temperature increase, the vibration energy from the atoms is alone enough to overcome this energy barrier, and is called the critical temperature, T_c. Above this athermal temperature, the shear strength and strain rate is nearly unaffected by the temperature. The critical temperature for Fe, is estimated to be 340K, or 67°C. The Peierls stress is hence highly material dependent, because it is directly connected to the electron bonding, the atomic bonding and stability and the lattice structure. The dislocation mobility is thus highly dominated by the Peierls barriers, which result in the fact that the mechanical properties of materials depend on such fundamental characteristics.

It is well known that at low temperatures, the flow stress in α-Fe, like other bcc metals, exhibits strong temperature dependence. This dependence arises from the motion of screw dislocations between local energetic minima (Peierls valleys), a process which is initiated by the nucleation and motion of kink pairs along the dislocation. The motion of a dislocation along its glide plane can hence be described by the kink mechanism. Kinks nucleate and annihilate in pairs of opposite sense. The Peierls barrier is here associated with both the energy required to form a double kink and to move the individual kinks [1]. Under the combined effects from the image stress (i.e. surface stress) and dislocation core structure, a dislocation nucleated from the surface of a bcc pillar initiates one or more dislocations moving in the opposite direction before it exits from the surface. The process is repeating itself, hence, a self-replication process, so that a single nucleation is able to produce a much larger amount of plastic deformation than what a fcc metal is able to do (assuming dislocation starvation process in fcc).

2.4.1 Hall-Petch Relation

Under an applied stress, existing dislocations and dislocations generated by FrankReed Sources will move through a crystalline lattice until encountering a grain boundary, where the large atomic mismatch between different grains creates a repulsive stress field to hinder continued dislocation motion. As more dislocations propagate to this boundary, dislocation pile-ups occurs as a cluster of dislocations are unable to move past the boundary. As dislocations generate repulsive stress fields, each successive dislocation will apply a repulsive force to the dislocation incident with the grain boundary. These repulsive forces act as a driving force to reduce the energetic barrier for diffusion across the boundary, such that additional pile up causes dislocation diffusion across the grain boundary, allowing further deformation in the material. Decreasing grain size decreases the amount of possible pile up at the boundary, increasing the amount of applied stress necessary to move a dislocation across a grain boundary. The higher the applied stress to move the dislocation, the higher the yield strength. Thus, there is then an inverse relationship between grain size and yield strength. This relationship is described mathematical by the Hall Petch relation:

$$\sigma_y = \sigma_0 + \frac{k_y}{\sqrt{d}}, \tag{2.3}$$

where σ_y is the yield stress for which slip across grain bounday occur, σ_0 is a material constant for the starting stress for dislocation movement (or the resistance of the lattice to dislocation motion), k_y is the strengthening coefficient (a constant unique to each material), and d is the average grain size.

The essence of the argument is that the stress increases as the number of dislocations increases. Thus the larger the grain size, the more quickly is the critical stress reached at which slip is initiated in the neighboring grain. The theory also states that more grain boundaries create more opposition to dislocation movement and in turn strengthens the material.

Theoretically, a material could be made infinitely strong if the grains are made infinitely small. This is impossible though, because the lower limit of grain size is a single unit cell of the material. Even then, if the grains of a material are the size of a single unit cell, then the material is in fact amorphous, not crystalline, since there is no long range order of lattice structure, and dislocations can not be defined in an amorphous material.

Inverse Hall Petch relation: It has long been theorized that there is a lower limit to the grain size for the Hall- Petch effect. Below this grain size, dislocations cannot bow out between obstacles without touching a boundary, and there is not enough space for pile-ups to form. Once the grain size drops below the equilibrium distance between dislocations in a pileup, pileups are no longer possible, and the Hall-Petch relation should cease to be valid. It is, however, not clear how the yield stress should depend on the grain size below that point.

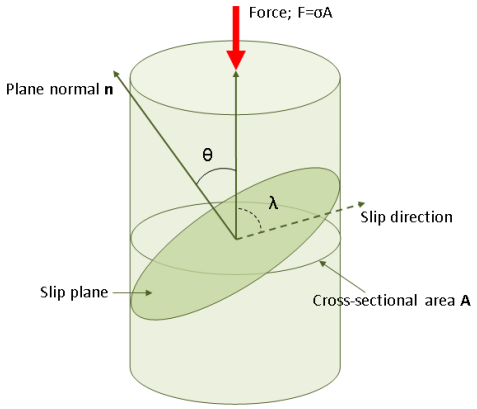

Figure 2.10: Sylindrical compression specimen

2.4.2 Schmids Law

To move dislocations, a certain stress must be applied to overcome the resistance to dislocation motion. The applied axial force on a macroscale specimen surface, will activate slip systems at microscale due to shear stress, τ (see fig.2.10) [**?**]. Slip thus occur when the shear stress, τ, acting in the slip direction on the slip plane, reaches a critical value. It is found that the value of tR at which slip occurs in a given material with specified dislocation density and purity is a constant, known as the critical resolved shear stress τ_{CRSS}. This is Schmid's Law.

Schmid's law thus defines the relationship between shear stress, the applied stress, and the orientation of the slip system. It is an equation for finding the stress in the slip plane given an axial force and the angle of the slip plane.

The quantity cos θ cos λ is called the Schmid factor, often labeled s. The tensile stress at which the crystal starts to slip is known as the yield stress σ_y, and corresponds to the quantity F/A in the above equation.

Symbolically, therefore, Schmid's Law can be written:

$$\tau_{CRSS} = \sigma_y cos\theta cos\lambda \tag{2.4}$$

In a given crystal, like BCC, there may be many available slip systems. As the tensile load is increased, the resolved shear stress on each system increases until eventually τ_c is reached on one system. The crystal begins to plastically deform by slip on this system, known as the primary slip system. The stress required to cause slip on the primary slip system is the yield stress of the single crystal. As the load is increased further, τ_c may be reached on other slip systems; these then begin to operate.

2.5 Determination of flow curves

Because the interface contact between the flat indentertip and the pillar top is unstable at the point of initial loading, the resulting loading curves exhibit an initial artifact. The slope of the curves does not represent the material behavior at this point, and is therefore excluded in the following results. For each curve, the steepest slope of the linear elastic region, is manually found. The new slope intersects the x-axis, creating an offset region for where the point of 2% flow strain and initial slip is determined. This artifact is shown in the figure below. A linear red line is plotted to visualize the offset point of one of the curves.

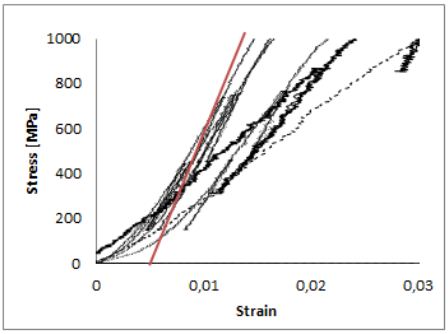

The stresses are calculated by dividing the measured load by the initial area, using the assumption of constant plastic volume. The diameter of the pillar is determined at $h/4$ from the pillar top.

$$\sigma = \frac{F}{A_0} = \frac{F}{\pi r^2} = \frac{4F}{\pi d_0^2} \tag{2.5}$$

2.6 Strain Gradient Plasticity Theory and Size Effect

Dislocations are classically divided in two categories: statistically stored dislocations (SSD), which trap each other in a random way, and geometrically necessary dislocations (GND), which is associated with the local incompatibility (heterogenity) of the crystal lattice and are thus related to plastic strain gradients.

The size effect is attempted to be explained in different theories and relations. In the case of plastic deformation of crystalline materials, the high-angle energy barrier at the boundaries of the grains, or intergranular inhomogeneous regions, can result in gradients of plastic strain. Because grain boundaries represent an obstacle which is impeding further dislocation movement, the strain will increase due to a gradient, until a critical value is reached. At the critical point, energy is released, and the dislocation can cross the obstacle and impose further movement. This subsequently results in the formation of Geometrical Necessary Dislocations, GNDs, which are required for the compatible deformations of different parts of the grains. Hence, when a crystal is subjected to a plastic strain gradient, it has to store GNDs. These dislocations are hence formed because of the geometry of the sample, or that the material itself is plastically inhomogeneous, i.e. anisotropic properties. The latter would be caused by non-deforming phases or particles, like hard MA-particles at grain boundaries in F70 steel. These geometrically stored dislocations provide additional macroscopic strengthening caused by formation of jogs. The spacing between dislocation obstacles might be the length scale parameter dominating the size effect in multiple crystalline materials. ([2] [?] [?])

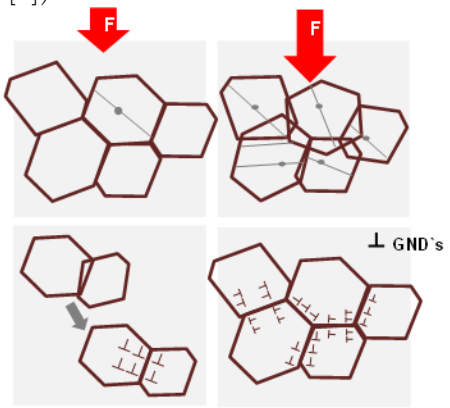

A single crystal strained uniformly, do not need to store dislocations. Though, dislocations accumulate by random trapping, referred to as Statistically Stored Dislocations, SSDs. The dislocations are trapped as dipoles with short range stress fields. Two dislocations of opposite sign move in neighbouring glide planes and form a dipolar configuration. When the stress is large enough, such dipole is destroyed and dislocation are free to glide again. These dipoles acts as a forest of sessile locks, where hardening is associated with the increasing yield stress required to cut the dipoles.

Dislocations generated due to plastic deformation, will either move toward the free surface forming slip lines, or stored within the structure in regular patterns to harden the material.

Fleck et al. suggested that dislocations become stored for two reasons: "they accumulate by trapping each other in a random way or they are required for compatible deformation of various parts of the crystal. The dislocation which trap each other randomly are referred to as statistically stored dislocations...gradients of plastic shear result in the storage of geometrically necessary dislocations." [3]

The process of hardening is hence due to the combination of GNDs and SSDs. GNDs are associated with a plastic strain gradient while SSDs are associated with plastic strain. Strain gradients are inversely proportional to the length scale of where plastic strain occurs. Thus, strain gradient effects are prominent and an important factor when the sample size is decreased to sub micro scale. At these scales, the dislocations must be treated like discrete entities. Conventional plasticity theory is sufficient at larger scales, because the strain gradient effects can be neglected.

2.6.1 Why is smaller stronger?

As a consequence of small-scale researching these last years, a question has emerged up on to the ground, making scientists all over the world scratch their head, because they get the same experimental results: Why is the material strength increased as my pillar size is reduced? A number different theories have been proposed throughout the years, but still, up on today, there has not been an agreement of the mechanisms causing these observed size effects.

It is accepted by several scientists, the fact that there is a fundamental different deformation mechanism dominating at small-scale testing, compared to that for bulk material behavior. The majority of experimentations and simulations are done with fcc materials, leaving the unresolved deformation mechanism in bcc as an open question to be further investigated. Several theories have been put forward, describing various causes of the observed size effect in both fcc and bcc materials.

The dislocation starvation theory was put forward by Greer and Nix, who investigated the strength at nanoscale for Au-fcc pillars. According to this theory, nucleated dislocations escape to the free surface faster than for new dislocations to be produced, when the surface to volume ratio is high. The volume is said to be at a starved dislocation state, whereby an increased amount of applied strength is needed to initiate dislocations [4].

The theory of dislocation starvation is widely axepted as the dislocation mechanism at small scales for fcc materials.

The dislocation density, ρ, is inversely proportional to the grain size, D:

$$\rho = \frac{1}{D} \tag{2.6}$$

From the Taylor eq., and the Hall-Petch eq. the yield stress can be linked to the dislocation density as followed:

$$\sigma_y = \sigma_0 + \alpha G b \frac{k}{\sqrt{D}} = \sigma_0 + \frac{k}{\sqrt{D}} \tag{2.7}$$

Once grain sizes drop below the equilibrium distance between dislocations, though, this relationship should no longer be valid. Nevertheless, it is not entirely clear what exactly the dependency of yield stress should be on grain sizes below this point. Different theories are explored and explained in the chapter of results.

2.7 F70 steel

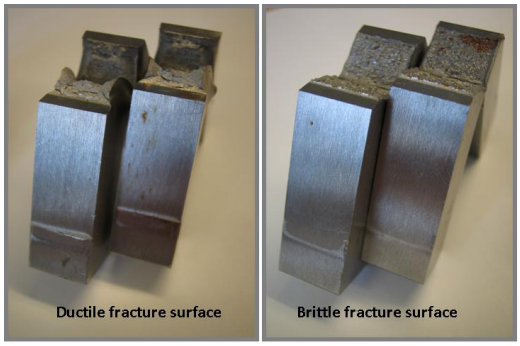

Figure 2.11: F70 Charpy notched test specimens: Fracture surface. Left: 5sec Right: 10sec

Increased working loads, reliability requirements, extreme temperature and chemically aggressive environments lead to an increased demand for high strength, combined with high toughness, in offshore steels. The use of welding as a joining method requires good weldability, for which the carbon content in a steel composition should be decreased. A decrease in carbon content results in strength decrease, due to a decrease in the amount of the second phase. To overcome this strength drop, additions of titanium, niobium and vanadium microalloying elements, have been used to provide precipitation strengthening and grain size refinement.
The steel used in this investigation was forged F70 steel rings. It should be designed to operate under harsh arctic environmental conditions, at temperatures as low as $-60°$C. At these temperatures, the ductile-brittle transition is a crucial factor, as it decrease the fracture toughness of the welding joints. Charpy V-Notched and tensile tested bars were cut at the fracture surface with dimensions of 10x10x4mm, indicating a bulk yield strength of 540MPa. Two different samples are investigated in the present work. The difference is due to the heat treatment.

2.7.1 Microstructure and Chemical Composition

The grain interior consists of upper bainite, with fractions of bulk martensite islands. The high-angle grain boundaries are blocky martensite-austenite, whereby MA-particles are present at prior austenite grain boundaries. The microstructure can be seen in fig. 2.12, where the 5 sec sample is placed to the left, and the 10 sec sample to the right. The MA-phase in the grain boundary is expected to be the critical fracture initiation zone, because it is more brittle than the microstructure within the grain inetrior. Within each high-angle grain boundary, there are low-angle grains, or packets, for wich the misorientation angle between the packets are less than $15°$. The microstructural orientation within each packet is homogeneous. Because each packet has different orientations, the high-angle grain is hence isotropic.
Depending upon the carbon content of the parent austenite phase, either lath (low-carbon) or blocky (high-carbon) martensite may form. In general, lath martensite is associated with high toughness and ductility but low strength, while plate martensite structures exhibit much higher

strength, which again enhance brittle and non-ductile properties. Plate martensite frequently contains microcracks from the impact of one plate into a previously formed plate. These cracks can initiate subsequent failures.

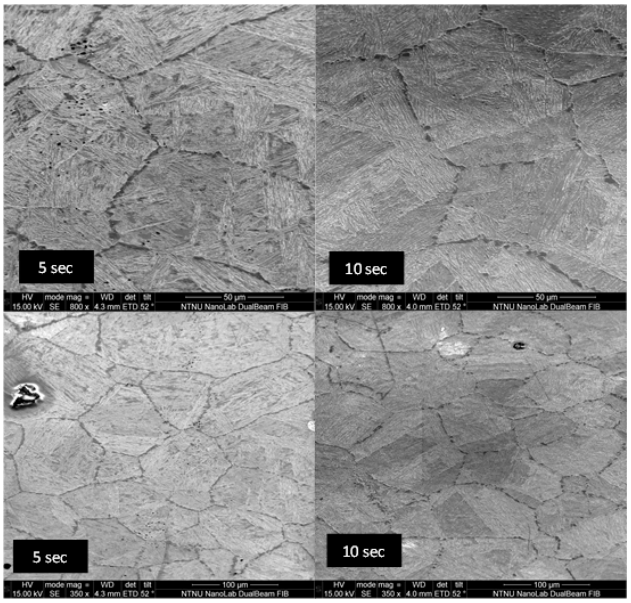

Figure 2.12: F70 Microstructure of the 5sec and 10sec sample

Increasing the carbon content of the austenite also depresses the martensite start (M_s) temperature and the martensite finish (M_f) temperature, which leads to difficulties in converting all of the austenite to martensite. When this happens, we have retained austenite, which may be either extremely detrimental or desirable under certain conditions.

2.7.2 Sample Preparation

See the authors Project work for autumn 2011, [5].

2.8 EU Project MultiHy: Dual Phase Steel

A large number of engineering alloys consist of two or multiple phases. Whenever a material consisting of two or more component phases with different properties, is subjected to stress, the phases deform differently. This results in additional interaction stresses and strains, wich magnitude depends on factors as the property difference between the phases, and the morphology and volume fraction of each phase. Due to these complexities, the properties of two-phase materials, in general, cannot be predicted on the basis of simple laws such as the law of mixtures for composites (matrix/fiber volume fraction and directional dependent E-modulus). Most important deformation mechanism is slip, which involves the movement of dislocations in the crystal. Slip occurs most easily on certain crystallographic planes in specific directions. The operating slip systems in two-phase materials depend on the applied stress and the elastic interaction stresses.

Dual Phase steel is commonly used in the automobile industry. Because the steel is exposed to very variable weather conditions, the properties should favour enhanced corrosion resistance, high toughness and strength and be light in weight. It is therefore necessary to know how different alloying components affect the steel. The main goal of the present work, is to investigate the effect of alloying composition to withstand hydrogen embrittlement and cracking of material. Two samples from Voestalpine are investigated, one with 0,05wt% Nb, and one with 0wt% Nb. Micropillar compression is employed to determine the mechanical properties of local zones in ferrite and martensite. Martensite phase will have lower Charpy Impact Energy than ferrite, and will thus be the more brittle phase. In combination with ferrite, which has a high toughness, but a low strength, the result can be a material with high strength. The amount of alloying components will determine in which degree hydrogen charging will decrease this strength. It is therefore crucial to investigate steel samples with and without Niobium. This hydrogen study is carried out by PhD. Adina Basa.

2.8.1 Microstructure and Chemical Compostition

The microstructure of VA_1200_DP mainly consist of a dual phase of martensite grains with a matrix of ferrite. Area fraction of ferrite and martensite is measured to be about 25% and 75% respectively of both samples. As the steel is cooled from the phase of austenite and ferrite, austenite converts into martensite. A transformation which is known to cause high dislocation density in the ferrite-martensite interface. The quenching is carried out at approximately the speed of sound, which is too fast for the carbon atoms to diffuse out of solution in the crystal lattice. As carbon is retained in the crystal structure, each unit cell is expanded in volume, inducing internal strain gradients. The resulting distortion of the unit cell hence induce a huge amount of lattice dislocations in each crystal. These dislocations makes the crystal structure extremely resistant to shear stress. Martensite is hence more or less ferrite, which is supersaturated with carbon.

Retained austenite occurs in small fractions (0,2wt% in 0% Nb and 0,7wt% in 0,05wt% Nb). Martensite imparts strength, while ferrite imparts ductility, and the fraction of each phase will thus determine the resulting mechanical properties. The grain size varies with a mean size of about 10 um. Niob (Nb) is the only alloying component which amount makes out the different

between the two samples. Nb is an effective microalloying element for steel. Adding nb to the steel causes the formation of niobium carbide and niobium nitride within the structure of the steel. These compounds improve the grain refining, retardation of recrystallization, and precipitation hardening of the steel. These effects in turn increase the toughness, strength, formability, and weldability. It is an important alloy addition to high strength low alloy steels which are widely used as structural components in modern automobiles.

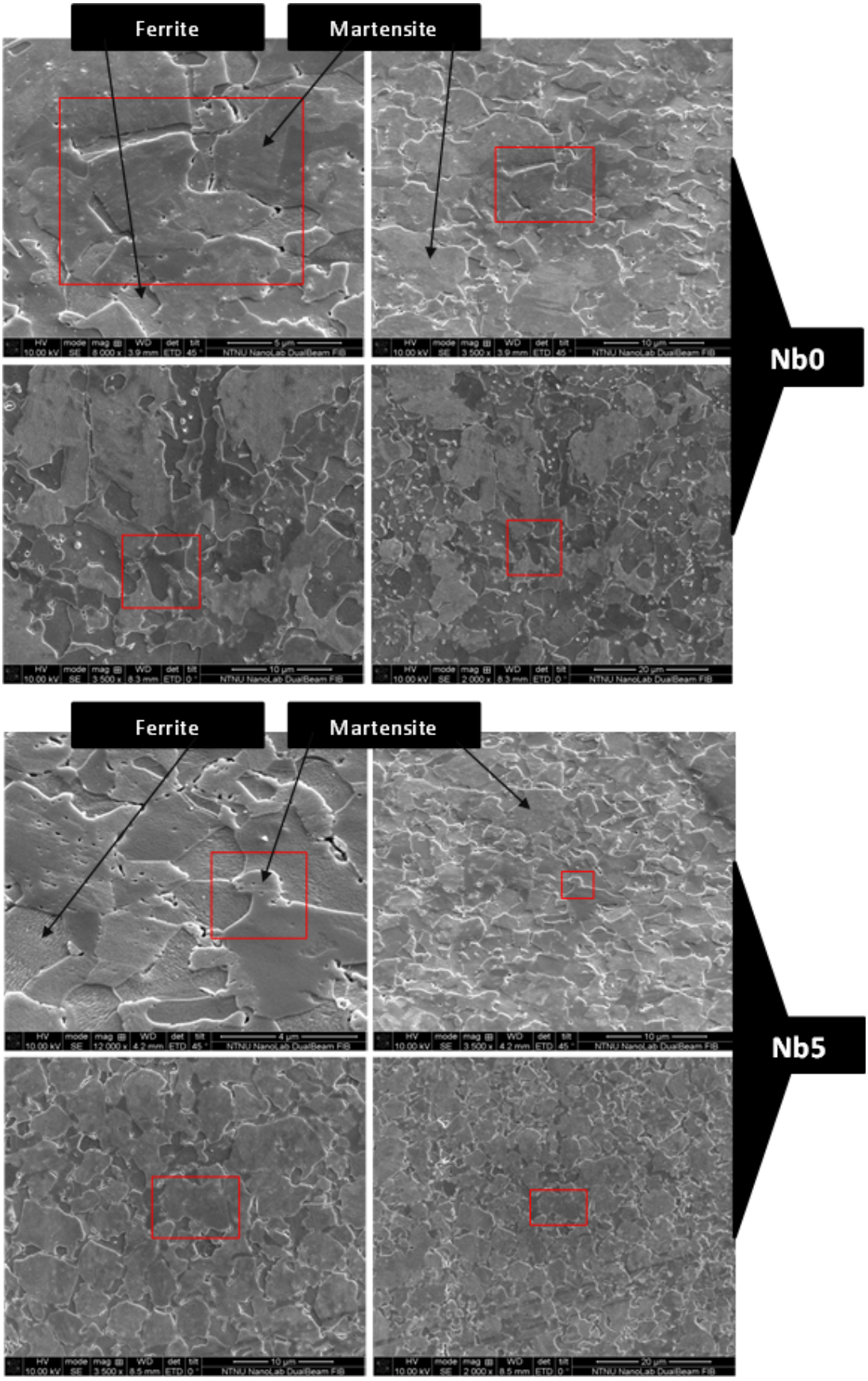

Figure 2.13: Microstructure for Nb0 above, and Nb5 below. Notice the reduced grain size for Nb5

2.8.2 Sample Preparation

In agreement of the customer, two samples (DP) was selected to be further investigated by nano mechanical compression.

The preparation was done with help from PhD. Bjørn Rune Rogne and PhD Adina Basa. Grinding was done mechanical in 5 steps. It was started with coarse particle naps, and stepwise finer grained naps. The sample surface was relative even and flat after grinding, which was also aimed for. Between each step of grinding, the samples were cleaned with ethanol and put to dry in a heat chamber. Followed after grinding, the polishing was done in 3 steps. Naps of diamond 3 um particles was used for 3 min. After cleaning, the particle size was reduced to 1 um, and the samples polished for 1,5 min. This leaves the surface blank and clean. To make the micro structure visible in SEM and in the optic microscope, chemical polishing was used. Chemical polishing was done with operational variables as followed: Voltage 20 V, etch rate 8, time 15 sec. The function of successful etch procedure was satisfying, and the system variables used at chemical polishing can be seen in the picture below.

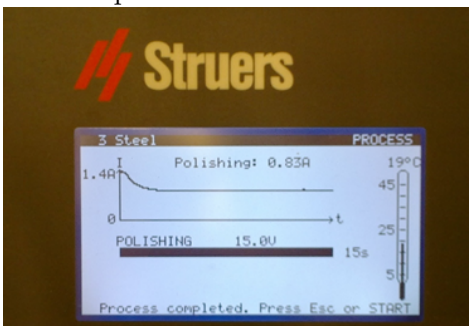

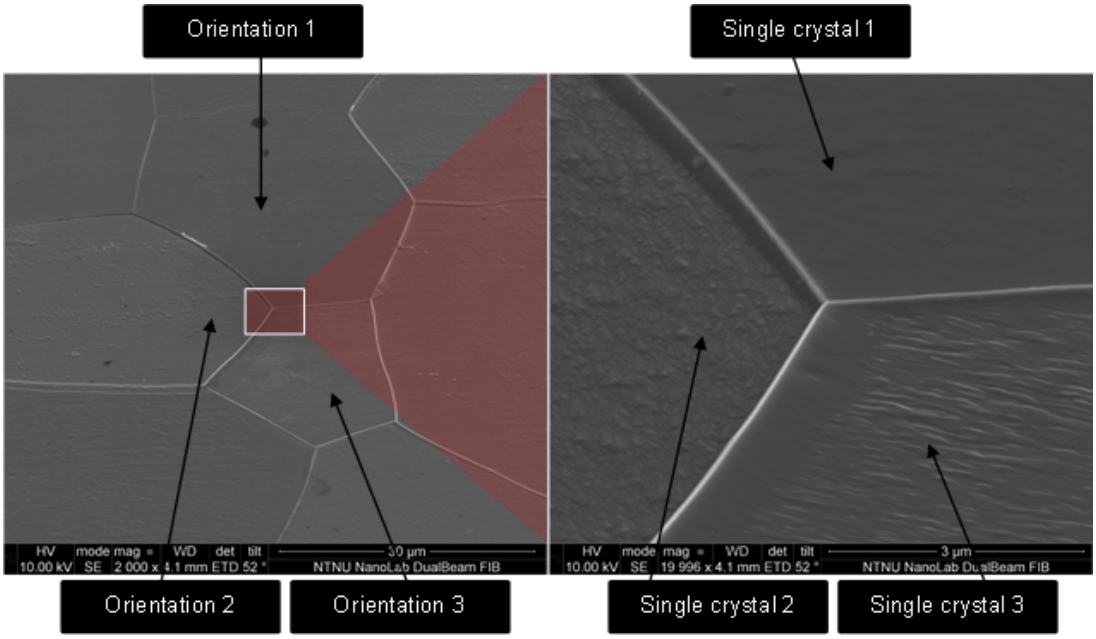

Figure 2.14: Microstructure of single phase BCC pure iron

2.9 Pure Iron

Iron is a polycrystalline single-phase material.

Throughout this study, single-phase iron was investigated. By placing pillars within the same grain orientation, the activated fracture planes should have similar Schmid factors, and thus similar fracture mechanisms. The grain boundary limitations are also excluded, resulting in a single-crystalline dislocation situation. To place pillars of various sizes within the same orientation, one can determine if there is a size effect, by excluding orientation dependent variables.

2.9.1 Microstructure and Chemical Composition

The sample is heat treated at 650 for 5 hours, leaving an average grain size of 40 um. The purity of the Fe is 99,998%, making the crystallographic orientation homogeneous within each grain.

2.10 Electron Backscattering Diffraction (EBSD)

Electron Backscatter Diffraction Analysis, is used to perform quantitative microstructure analysis in the Scanning Electron Microscope, on a millimetre to a nanometre scale.

2.10.1 What is EBSD?

EBSD is a microstructural-crystallographic technique to measure the crystal orientation. The electrons accelerated from the primary electron column can be diffracted by atomic layers in crystalline materials. These diffracted electrons can be detected when they hit a phosphor screen and generate visible lines, called EBSPs (electron backscatter patterns) or Hough bands. These patterns are projections of the geometry of the lattice planes in the crystal, and they give direct information about the crystalline structure and crystallographic orientation of the grain. When used together with a computer data base that includes information of phases of interest, and with software for processing the EPSPs and indexing the bands, the diffracted electron data can be used to identify phases and orientations.

In this work, all EBSD scanning was done on Hitachi SU-6600.

2.10.2 How does EBSD work?

The electron beam is accelerated with a voltage of 20kV, and strikes a 70 tilted sample. The electrons are diffracted in a spherical matter by the crystal lattice to form a pattern on a fluorescent phosphoric screen. This pattern is characteristic for the crystal structure and orientation at the specific sample region.

An EBSD detector system consists of the following components 2.15:

- A phosphor screen which is fluoresced by electrons from the sample to form the diffraction pattern.
- A charge coupled device (CCD) camera, together with optics for viewing the diffraction pattern on the phosphor screen.
- A computer to control EBSD experiments; collect and analyse the diffraction patterns as well as display results and do further processing.
- Electronic hardware that controls the SEM scanning.

The detector is a digital CCD camera, which will intersect a portion of the diffraction pattern. The cameras CCD chip is illuminated by a phosphor screen that intersects the spherical diffraction pattern. The phosphor converts the diffracted electrons into light suitable for the CCD to record. The EBSP is then analyzed. The patterns are defined by the lattice parameters of the particular crystal structure under the beam. Possible lattice structures and orientations of the crystal are matched to the EBSP until the best fit is found. The pattern is then considered indexed.

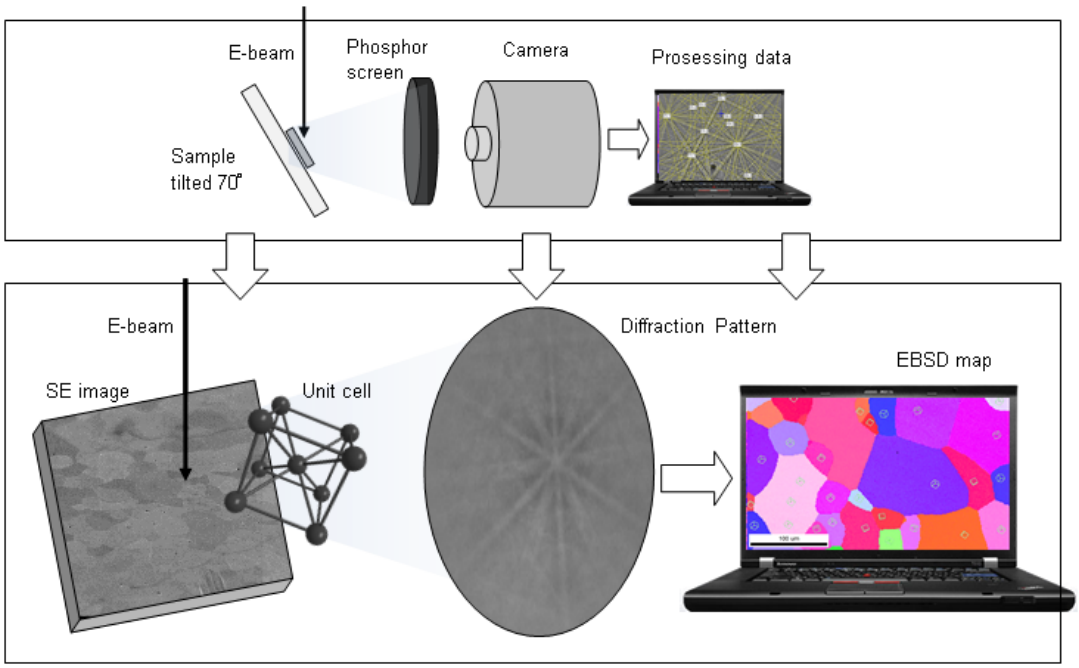

Figure 2.15: Electron backscattering diffraction system

2.10.3 Mechanical Preparation for EBSD

EBSPs are generated at very shallow depths within the sample, so appropriate samples must be free of damage to the crystal lattices at the surface of the sample. Mechanical grinding and polishing preparation of samples results in significant damage to crystal lattices near the surface of most materials. Therefore, it is necessary to perform additional chemical polishing on samples after they have been mechanical polished. The finest possible abrasive grain size of SiC-paper should be used for plane grinding. Fine grinding should be carried out with diamond on a rigid disc for maximum planeness, followed by a diamond polish with low force. The final polish is carried out by chemical electro polish.

2.10.4 Image Processing

Diffraction is a scattering phenomenon. When the electron beam are incident on crystalline solids, they are scattered in all directions. In some of these directions, the scattered beams are completely in phase and reinforce one another to form the diffracted beams. The Bragg law describes the conditions under which this would occur. It is assumed that a perfectly parallel and monochromatic e-beam beam, of wavelength λ, is incident on a crystalline sample at an angle θ.

Braggs law state that diffraction will occur if:

$$\lambda n = 2dsin\theta, \tag{2.8}$$

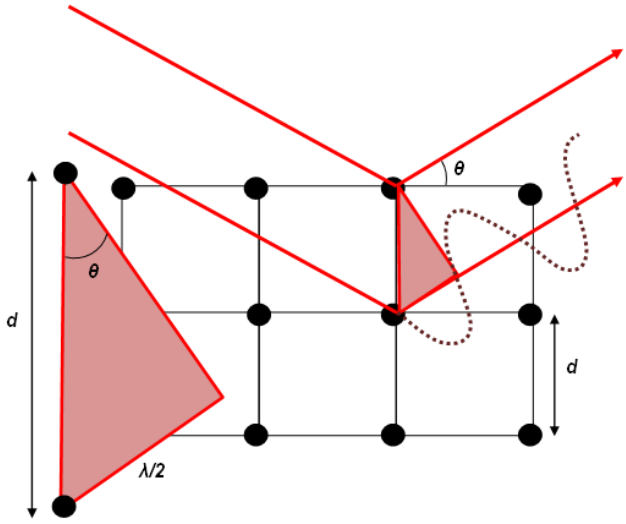

Figure 2.16: Braggs law for diffraction pattern

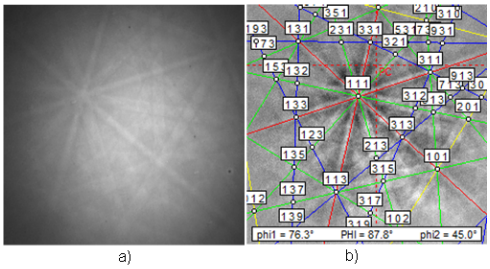

Figure 2.17: a) Kikuchi bands, b) Indexing with reference phase og α-Fe

where d is the distance between atomic planes, n an integer (1, 2, ..., n), λ the wavelength of the 20 kV electron beam which is 0.00859 nm, and θ the angle of incidence of the e-beam and the atomic planes. For a given λ of incident e-beam and interplanar spacing, d, only specific θ angles will satisfy the Bragg equation. First pattern will occur when $n = 1$. Continued rotation leads to patterns at higher order, which corresponds to $n = 2, 3, ...$ Electrons that satisfy the Bragg condition for a crystal plane are channeled and show the Kikuchi bands. Kikuchi bands are linear features that appear in an EBSP. They correspond to a difference in electron intensity from the background level. The width of a Kikuchi band is twice the Bragg angle for the relevant atomic plane.

The data collected from indexing, as location, orientation, image quality, confidence index, and phase, can be processed to create Orientation Imaging Micrographs (OIM), making a visual representation of the crystallographic microstructure. Each point can be assigned a color or gray scale value based on a variety of parameters such as orientation, image quality, confidence index, phase, etc.

For example, an orientation map 2.18 is generated by shading each point in the OIM scan

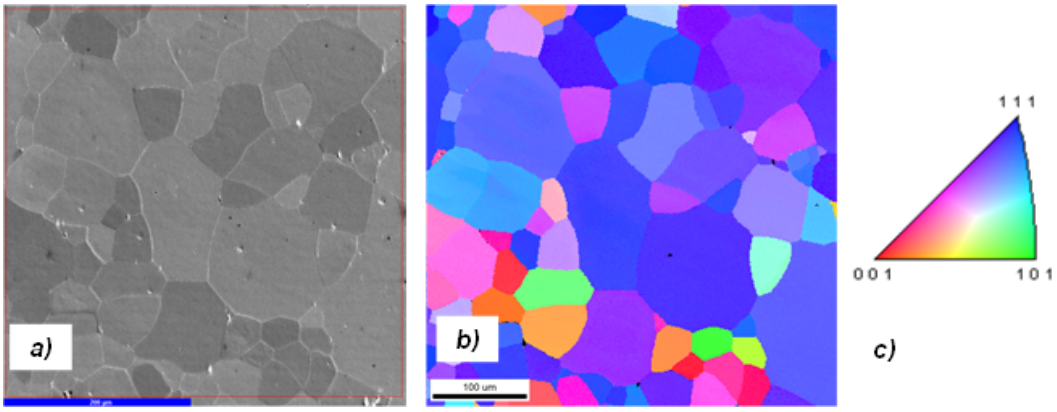

Figure 2.18: a) SEM image b) Colored IPF map c) Inverse pole figure

according to some parameter reflecting the crystallographic rotation. The map is an Inverse Pole Figure (IPF) map in which the colors correspond to the crystal orientations as shown in the projection. Crystals with their 111 axis normal to the surface of the sample will be blue, and so on.

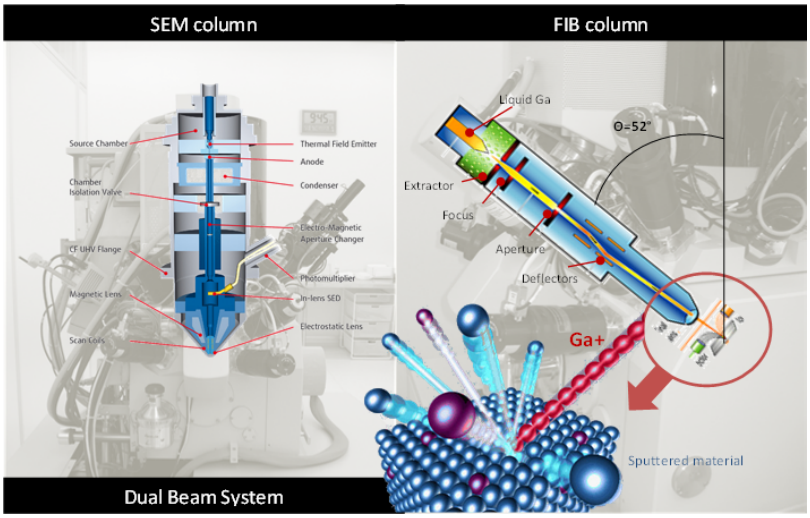

Figure 2.19: Dual Beam System

2.11 Focused Ion Beam Pillar Fabrication

During the first part of the milling procedure, when the energy of the beam current is high (9nA-20nA and 30kV), the ion beam severely impacts the fine structure of the matter. Ga atoms are implanted on the surface of the FIB-section, constituting a non-homogeneous Ga-layer, and sputtered Ga atoms and sample surface atoms redeposit on the FIB section. To reduce the possibility of Ga+ implementation within the final pillar interior, the first step in the milling process is done with an inner diameter of 7-10μm. The largest final pillars fabricated during this work, has a diameter of 2μm. Deposition of Ga+ ions do not have enough energy to implement 5-9μm, thus this is a safety layer protecting the pillars from FIB damage in the first milling step.

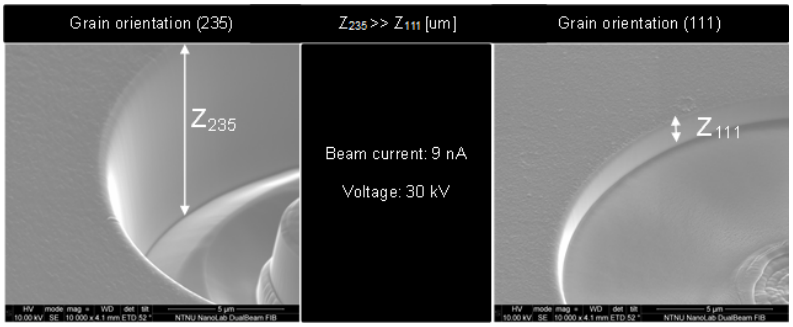

Figure 2.20: Initial milling step in Fe: Two different grain orientations, equal FIB settings, different material sputtering yield

In fig 3.24 a SE image of the coarse initial milling step in Fe is presented. The FIB settings are equal during the process (30kV, 9nA and z value of 2 μm), but the grain orientation is

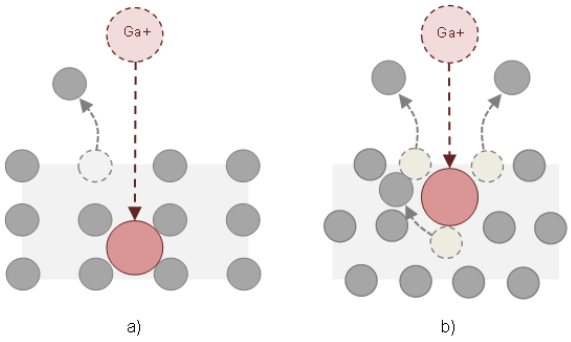

Figure 2.21: Ga+ implementation: a) Tunneling effect: Low sputtering b) No tunneling: High sputtering

different. The sputtering yield in orientation (235) is much higher than for orientation (111). This is due to the lattice orientation and the phenomena of tunneling effect.

Tunneling effect

Different grains consists of different lattice orientations. The orientation of the lattice structure (and the ion beam current and voltage) determines the amount of sputtered sample material. Ions that impinge at normal incidence onto the sample surface, at which the sample atoms are aligned in such a way that the mean free path between heavy Ga ions and sample atoms is large, that is a low collision cascade, there will be a low sputtering yield. The implementation range, or trajectories, of Ga+ is then high, see fig. 2.21 a). When the lattice is oriented in such a way that the Ga+ beam do not have a free implementation path, the amount of sputtering will be large, fig.(2.21 b).

FIB damage

The ion impact on the specimen surface not only leads to material removal by the sputtering process, but also to the formation of a damaged layer that may extend several tens of nanometers into the material. The assessment of the damage impact can be represented byy Monte-Carlo simulations. This mathematical approach permits to simulate in three dimensions the penetration of the ions into the matter and the full cascades of energy loss. These trajectories will cause initiations of dislocations, which will affect the mechanical behavior of the sample material. This is why the pillar fabrication is done without focusing the ion beam at the pillar at any time in the process. Though, implementation of heavy ions may also occur during the milling process. If the ion beam is poorly focused in the milling process, the incident angle is increased, and the distribution of ions have a larger beam diameter. This can be seen directly on the pillars, as an increased curvature on the pillar top surface and in the notch intersection with the bulk area. As the cross section of the pillar is relatively large (2μ m), the effect of the implementation is negliable. The FIB damage has been investigated earlier, by various authors, demonstrating that the use of 30 keV Ga+ ion exposure can cause extensive microstructural modification of metal samples. The depth of amorphous regions depend on non-/channeling- orientations which gives the ion range, the sample geometry and the ion current used. Until these effects are understood, caution should be used when FIB is employed to prepare samples for microstructural investigations, as even short exposures can result in unwanted changes to the sample.

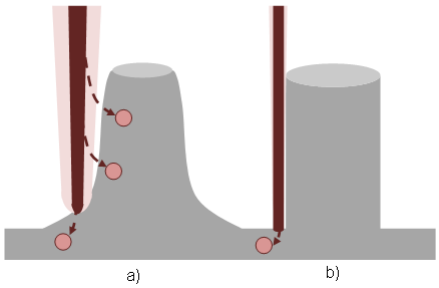

Figure 2.22: Focuse of the Ion beam: a) Ga+ implementation b) Increased focus of beam; less pillar damage

2.12 Nano Compression

The compression test is mainly used to study plasticity and to investigate mechanisms that are responsible for the higher strength of materials at micro/nanoscales. This test can be performed up to very large strains in order to investigate not only the first instants of plasticity but also the large strain behaviour and strain hardening response.

The in-situ flat tip loading results in a load [uN]/displacement [nm] curve. When converting the result to stress/strain curves, the cross section area of the pillar, and the pillar hight is needed. The cross section corresponds to the pillar diameter, at which the point of measurement was carried out at 1/4 from the pillar top. The hight was measured from SEM pictures, taking into account the tilt of 52 degrees.

The load function used in all experiments is an open loop control. As the pillars tested, have variable diameter, the loadfunction was corrected due to the loading rate and the peak load. If the LR is held constant for all diameters, this could induce an enchanced size effect, because of the possibility that increased LF incrase the yield strength. This would also just be one more variable to take into account when analyzing the post-compression results. Throughout the tests, some random compressions were done in which included two unloading procedures, in case the Elastic modulus would be of interest to measure. This did not affect the final results. The E-Modulus was not measured for any tests, because the scatter is too large to give a proper value.

Chapter 3

Results and discussion

3.1 F70 Steel

The arctic steel, F70, is heat treated in two cycles, to simulate the intercritically reheated coarce grained HAZ (ICCGHAZ), which is present in weldings. This is the critical point of the structure for which a micro crack initiates. The bulk yield strength is measured by tensile test to be 490MPa. Two different cooling rates between T=800°C and T=500°C ($\Delta T_{8/5}$) results in vastly different mechanical properties. One sample is cooled in 5 sec, $\Delta T_{8/5}$ = 5sec, the other is cooled in 10 sec, $\Delta T_{8/5}$ = 10 sec.

3.1.1 EBSD

It was attempted to make EBSD maps for the grain interior of F70 steel. Because the software is unable to index martensite, the resulting maps were useless. Stud.techn Line Rølvåg also used much time trying to index martensite, unable to succeed.

3.1.2 Pillar Fabrication

The pillars made for F70 steel has three different diameter sizes: 250nm, 450nm and 1000nm. They were localized in the grain boundary and within the grain interior. Both the 5 sec sample and the 10 sec sample were investigated. The fabrication technique was approximately equal for both samples, and also within the grain interior and the boundary. See table 5.1 and table 5.2 for further fabrication procedure parameters. The FIB procedure was done in 3 steps; 1st step with coarse, high current beam to make a large crater. This crater is 22um in diameter, to ensure enough space for the indenter tip of 10um to scan the area, and recognize the pillar top. The 2n̂d milling step is done with a lower beam current, and adjusted focus, to refine the geometry of the cylindrical pillar. The last step is done with a low current (0.026nA for the smallest pillars) to reduce the amount of Ga implementation. Examples of this 3 step procedure is presented in fig.3.2 for various pillar diameters. For pillars located in the high-angle grain boundary, the MA-particle of interest can be observed in the center of the coarse milled pillar (after the 1^{st} step).
In fig.3.1, an example of the pillar fabrication of the smallest pillars (d=220nm) in the 10 sec

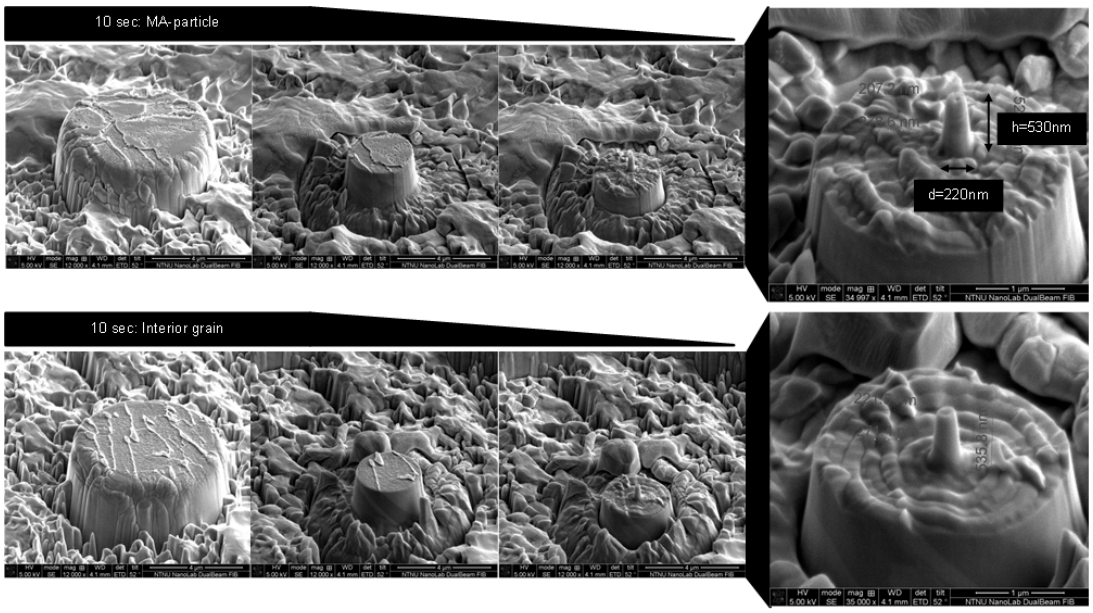

Figure 3.1: Fabrication of F70 pillar of diameter 220nm. Top: Grain Boundary. Bottom: Grain Interior

sample are presented. The MA-particle can be observed in the picture in the top, after the first step of coarse milling, while the grain interior can be observed within the pillar in the bottom. The resulting pillar can thus be located exactly in the phase of interest, and will contain this particular phase along its whole length axis. The smaller the pillar, the higher the probability that the phase is homogeneous along the hight.

3.1.3 Nanocompression

During compression testing, an open loop load function is used, where the loading rate is adjusted due to the varying pillar diameter. If this is not done, the relative loading rate (LR) can contribute to an increased size effect of the smaller pillars. The resulting stres-strain curves from this testing is shown in fig. 3.3.

Table 3.1: Load function: Open Loop

D_{pillar} $[um]$	$LoadingRate$ $[\mu N/s]$	$PeakLoad$ $[\mu N]$
1	50	2000
0.5	25	1000
0.25	6.25	500

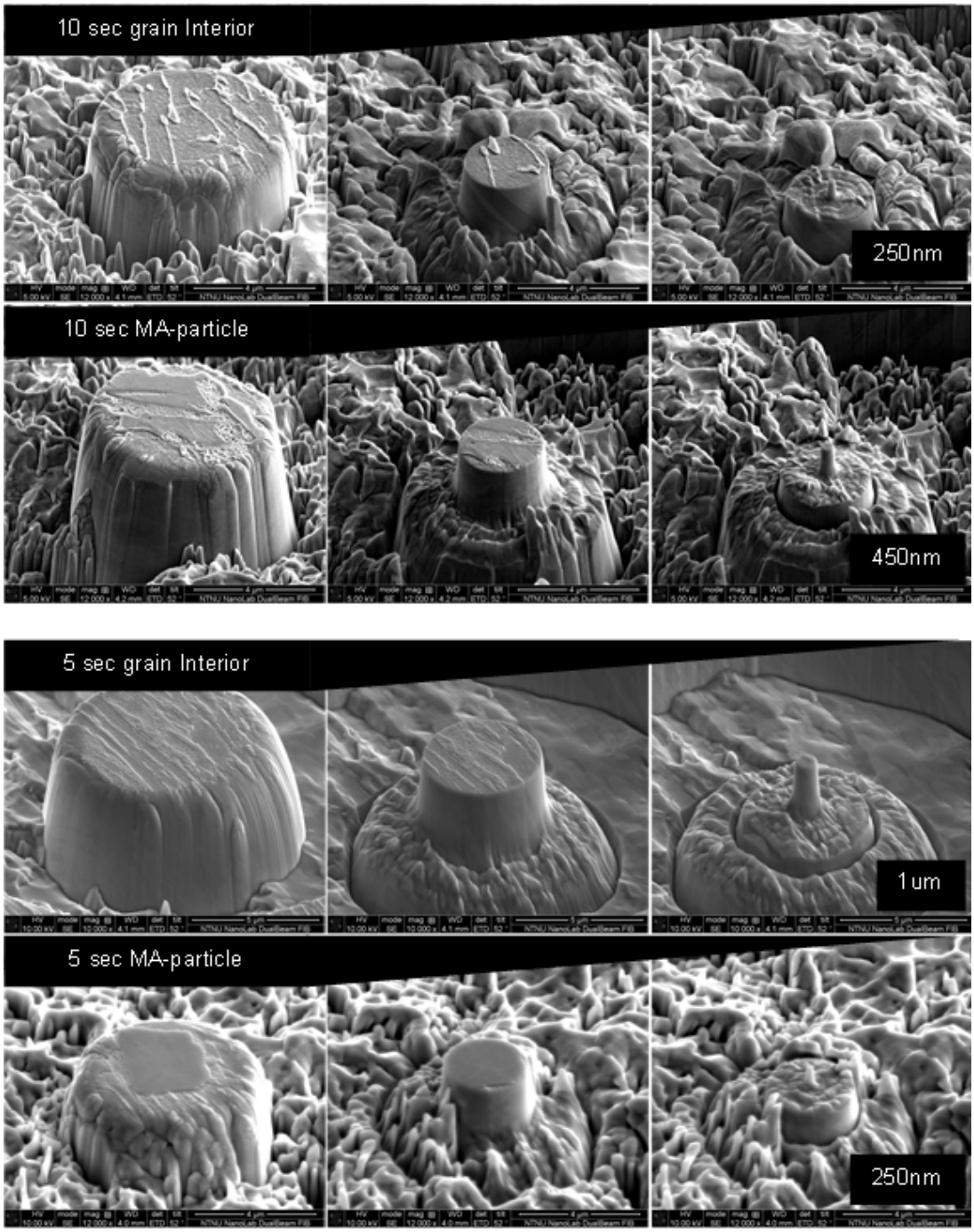

Figure 3.2: F70: Examples of FIB pillar fabrication procedure in 3 steps

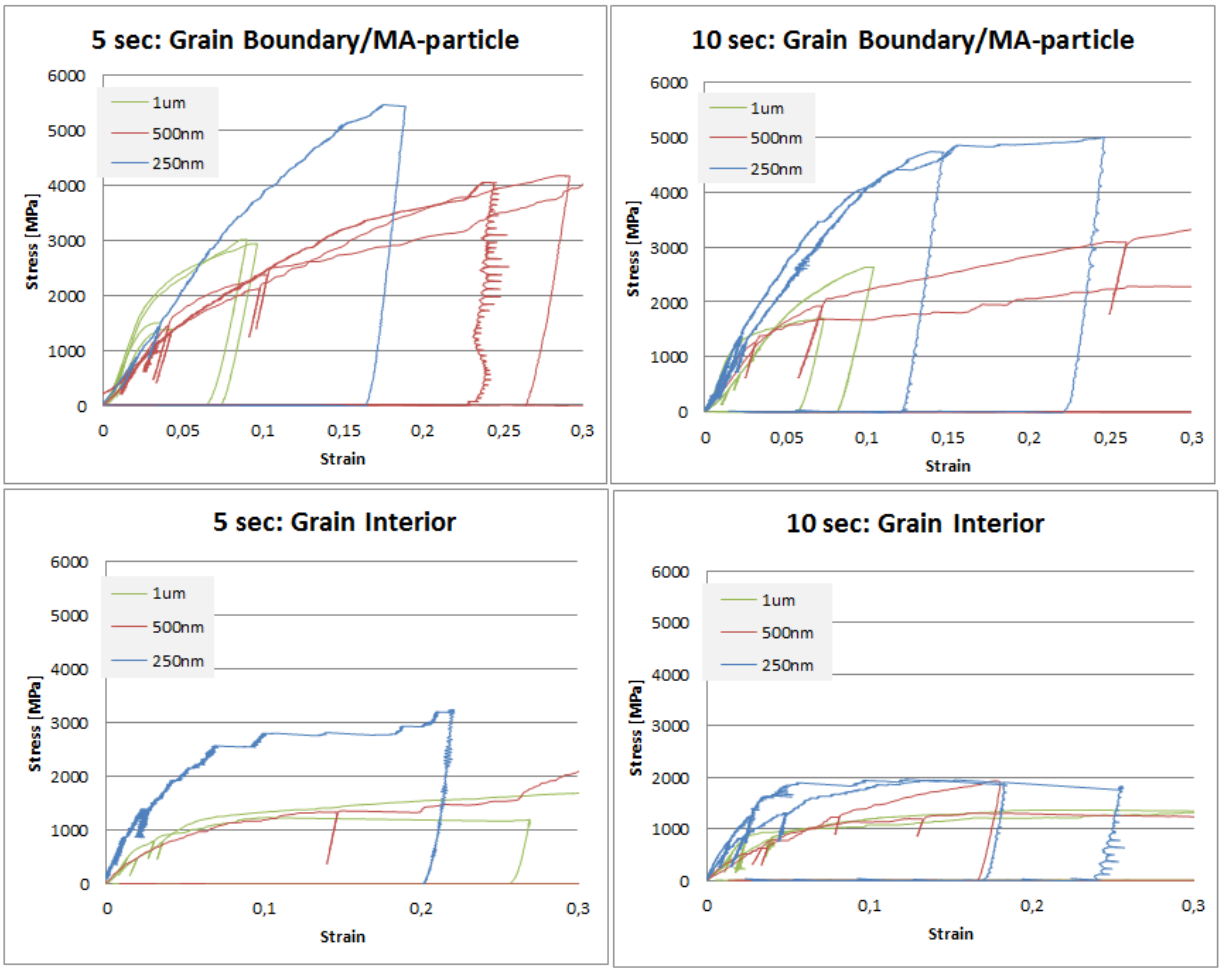

Figure 3.3: F70: Post-Compression Stress-Strain Curves

3.1.4 Results F70

In general, two different deformation mechanisms were prominent at post-compression: shear slip deformation, and an axial uniform flat deformation. These two mechanisms is presented in fig.3.4, where four pillars of d = $1\mu m$ are located in a grain boundary/MA-particle in the 5 sec sample. It is obvious that the resulting strength of the pillar depends highly on the lattice orientation within the MA-phase. All four pillars were compressed by the nanoindenter with equal system variables and load function. The result reveals two different favourable deformation systems. The two blue curves represent the shear slipping pillars, which strength is reduced compared to the two pillars represented by the green curves. The uniform axial flat deformation of the green pillars, is expected to result in both higher yield strength and strain hardening, thus the mechanism can be related to that of (111) planes in bcc α-Fe. The Schmid factor is lower for this type of deformation, while for the shear slip deformation, the factor is closer to 0.5. The scatter in all four curves are low, thus we have a reproducing behavior and reliable results. These two deformation mechanisms were prominent throughout all tests and are chosen to represent the overall behavior. The trend of deformation mechanism shows that pillars loaded within the grain interior, exhibits shear gliding, while the majority of the pillars in the MA-phase deformed in a (111) matter. Because it is not plausible to compare results from two different orientations, all pillars located in the MA-phase, which deformation mechanism is uniform axial flat, were selected and compared. These can be seen in fig.3.5. These 11 pillars range from 200nm to 1000nm, located in MA-phase of both 5 and 10 sec samples.

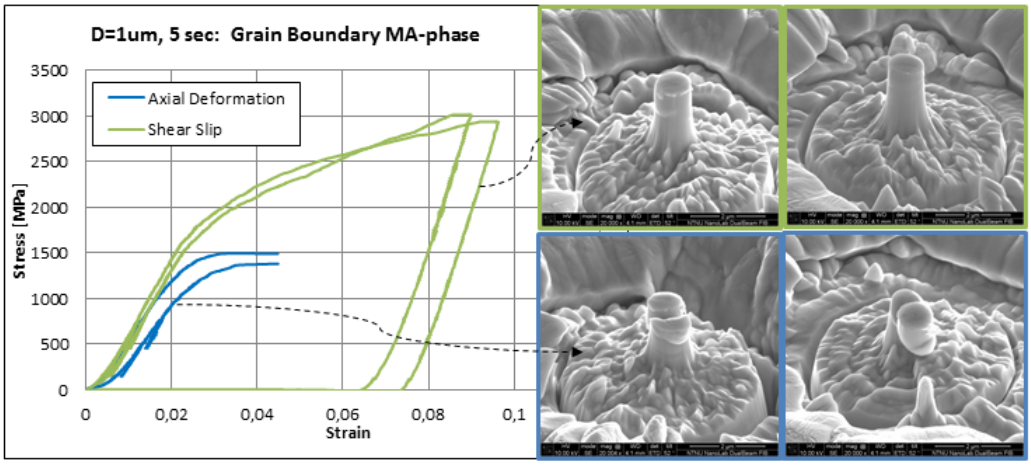

Figure 3.4: F70: D=1um, 5sec: 2 different fracture mechanisms. Green: Axial uniform deformation. Blue: Shear slip

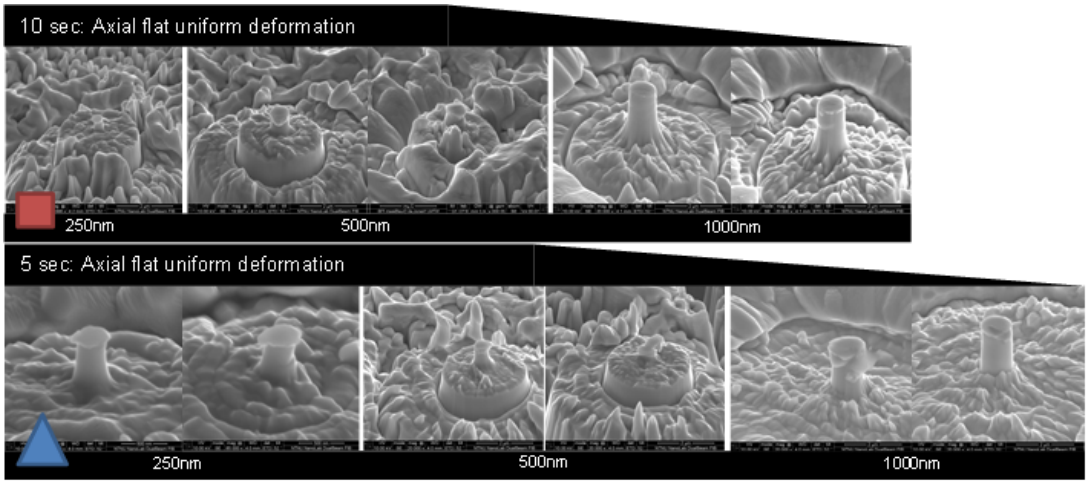

Figure 3.5: 11 pillars with uniform axial flat deformation

The MA-particles acts as hard islands surrounded by a softer matrix. By investigating SEM pictures of the microstructure, one can observe small fractions of these harder islands not only in the high-angle grain boundary, but also in the grain interior, as seen in fig. 3.6. Because these small islands is etched in the same amount and shape as the MA-particles in the high-angle grain boundary, it can be concluded that they are in the same range of hardness. The pillars fabricated in this work, were placed in between these small grain interior islands, though, it has been shown that the pillar might contain fractions of these particles. The probability of containing this phase, increase with pillar size. In the figure below, island in the grain interior is surrounding the small pillar, though the pillar, in this particular case, do not contain these islands and will thus have a reduced initial strain gradient.

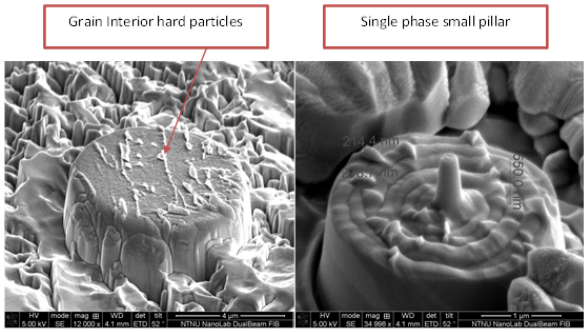

There are no pronounced visible difference in the microstructure, seen from SEM images. As the steel is reheated in the 2^{nd} cycle, the temperature reaches only the two-phase area, for which it is expected that the main difference in the phase transformation will be due to the MA-phase in the grain boundary, and not in the matrix. In the SEM images, it almost appears to be the opposite situation. The microstructure is presented in fig.3.6 and fig. 3.7. In fig. 3.6, the 5 sec sample is seen to the left, and the 10 sec sample to the right. The average distance between lines of hard islands fractions in the matrix, appear to be larger in the 10 sec sample than for

the 5 sec sample. In contradiction to this observation, the compression results indicate that the mechanical properties of the two samples are very similar, hence, the main difference must be caused by local properties of the MA-phase in the grain boundary. The MA-particles are more pronounced in the microstructure in the 10 sec sample, despite the fact that both samples were prepared and polished in a similar matter. In the MA-phase, the particle is more prominent, i.e. stands out in a topographic matter from the surface, in the 10 sec sample. This can indicate that the etching rate of the MA-particles in the 5 sec sample is higher in the 5 sec sample, which would also suggest that this phase is less hard, i.e. reduced strength compared to the 10 sec sample. Because compression tests indicate the opposite situation, the cause can be that the etching rate of the matrix in the 5 sec sample is reduced, compared to the 10 sec sample. This would indicate a higher strength of the matrix in the 5 sec sample, while the ER (etch rate) of the MA-particles in both materials are equal. In other words: It is very hard to make a proper evaluation of the difference in compression results, based on SEM images of the microstructure.

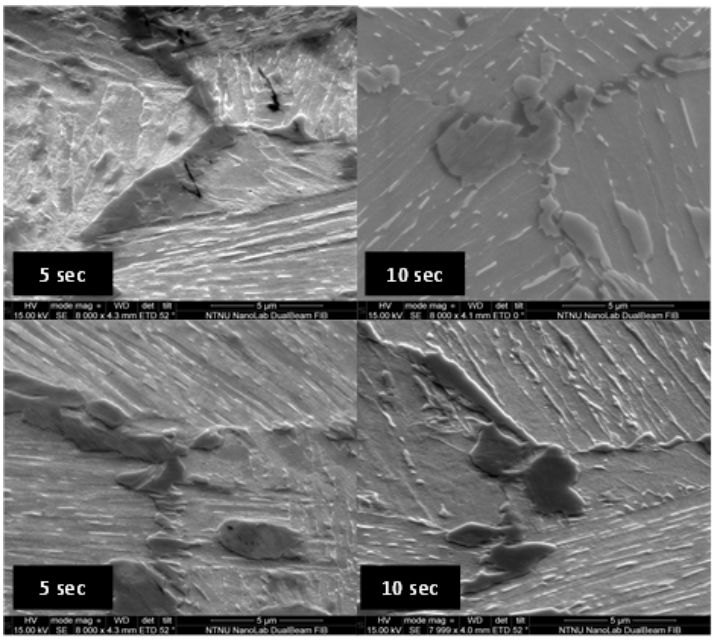

Figure 3.6: F70: Microstructure of 5sec sample to the left, and the 10 sec sample to the right. MA-particles in high-angle GB surrounded by matrix

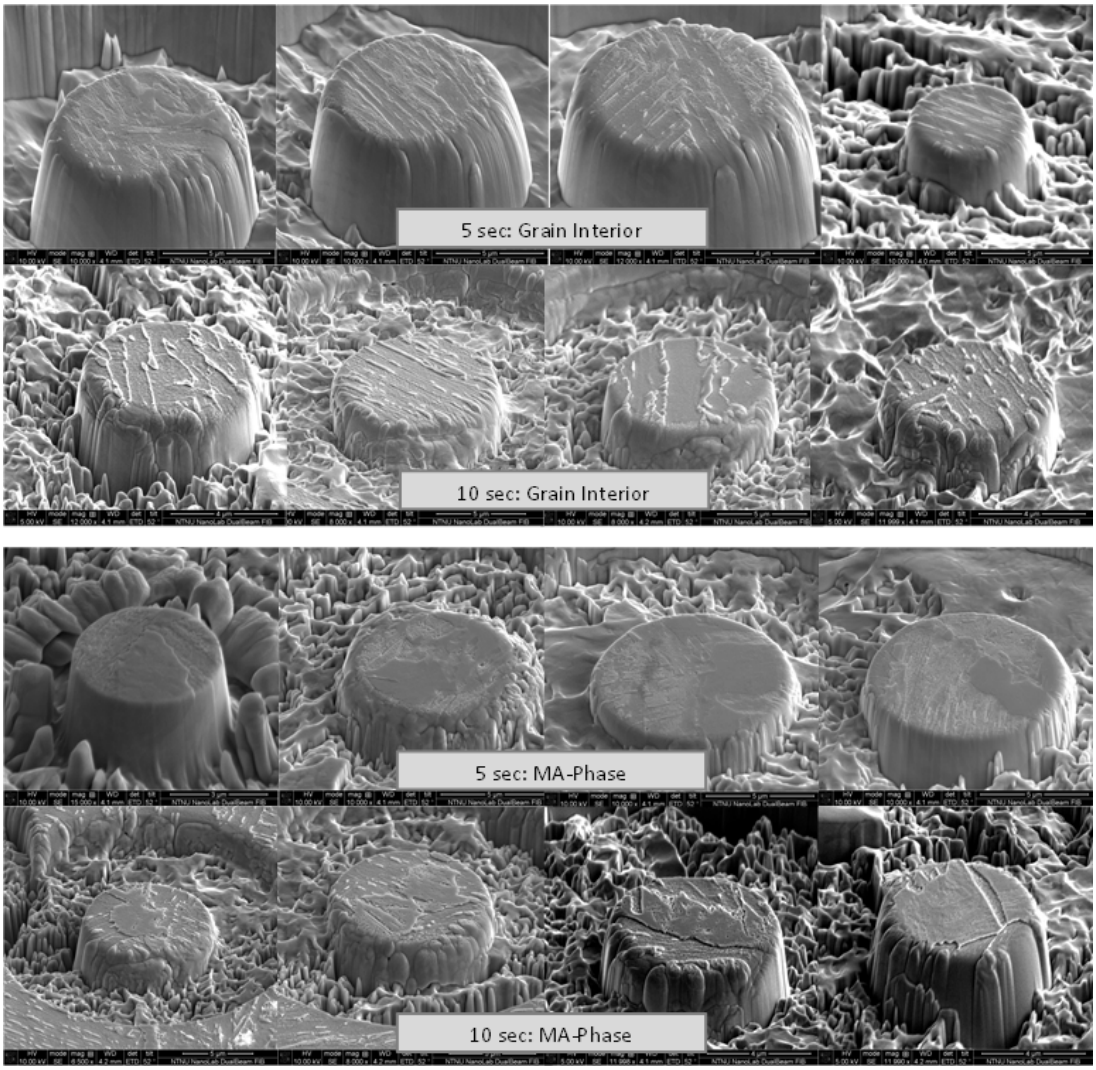

Figure 3.7: Microstructure of F70: Upper: Grain Interior of 5 and 10 sec sample. Bottom: MA-particles of 5 and 10 sec sample respectively

The result of relating the yield strength at 5% strain and 2% strain to the pillar diameter is shown in fig.3.8. The upper two curves shows the absolute values, while a corresponding lg/lg plot is shown below. Red squares represent the 5 sec sample, while the blue triangles represent the 10 sec sample. It is evidently a prominent size effect when the pillar diameter is reduced to near 200nm. For the 10 sec sample, the size effect is more pronounced than for the 5 sec sample. It is though not any prominent difference between the pillars of 500nm and 1000nm, as the 500nm pillars has a yield strength similar or lower than for its 1um counterpart. From the lg-lg plot, exponential trend curves are added, for which the R^2 values are quite low, 0.2 and 0.5 for the 5 and 10 sec sample at 5% strain respectively. This value indicate the trend-line fit to the actual plotted points, hence the fit is not good. (A prominent size effect has a value in the range of 0.7 to 1.0, as for bcc-Fe) The corresponding fitting power law exponent n, is also low, -0.22 and -0.36, indicating a low size effect sensitivity. (For comparison, values of Fe is in the range of -0.6 - -0.7. Other bcc metals as Mo and V has n-values corresponding to these measured for F70). The size effect trend is hence more prominent for the 10 sec sample, due to the high yield strength values for 1um pillars of the 5 sec sample. It is clear, from this plot, and from the corresponding stress-strain curves (which can be seen in fig. 3.3), that the 5 sec sample exhibit higher yield strength than the 10 sec sample. It is also evident that the strength is significantly increased in the high-angle grain boundary, compared to the grain interior, as expected. Because blocky martensite is present in the MA-phase, the ductility decreases and the local properties become brittle. It can be observed from the stress-strain curves for grain interior pillars, that after the point of shear gliding, the curves do not undergo significant hardening to higher stress levels. Pre-yield, the stress is more or less constant until a critical amount of strain is reached, corresponding to the point of activation of more slip planes. For pillars in the grain boundary, the yield stress is higher, hence the elastic properties are enhanced. The curves of the smallest pillars in the grain interior behave in a more jerky matter than for the corresponding curves in the MA-phase. This indicates that the deformation mechanism is different. Because the MA-phase small pillars exhibit a smooth curve without large energy exhaustions, the amount of activated glide planes in different directions locks each other from shearing at one specific plane. This as also caused by pre-dislocations available in the MA-phase. In all cases, the smaller pillars exhibit an increased strength, while the two larger sizes are more or less equal. In the matrix, the tendency of overlapping graphs of same pillar size is prominent, i.e. the scatter is reduced. The reproducable tendency is also evident in both grain boundary samples.
The measured 2% yield strength and the 5% yield strength for the representative pillars in the stress-strain curves are presented in table 3.2

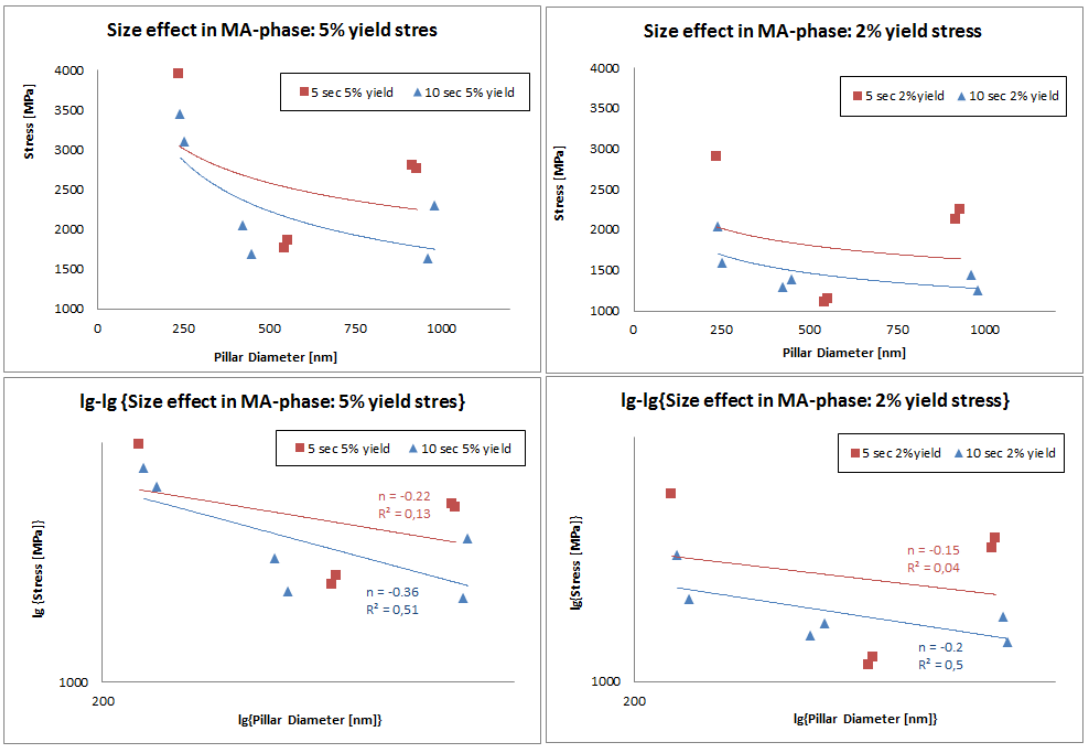

Figure 3.8: Left: 5% Yield strength of varying pillar size. Right: 2% Yield strength of corresponding pillar size. Upper: Stress-Pillar diameter. Bottom: Corresponding lg-lg plot

Table 3.2: $\sigma_{2\%}$ and $\sigma_{5\%}$

Sample	$\sigma_{2\%}$ [MPa]	$\sigma_{5\%}$ [MPa]	*Diameter*[*nm*]
5 sec	2900	3950	235
5 sec	1150	1850	553
5 sec	1100	1750	543
5 sec	2125	2800	918
5 sec	2250	2750	930
10 sec	1600	3100	253
10 sec	2050	3450	240
10 sec	1390	1690	449
10 sec	1300	2050	424
10 sec	1250	2290	981
10 sec	1450	1625	962

In fig. 3.9, a representative selected 10sec pillars are presented. From the SEM pictures, slip lines, misorientations or phase transformation can be observed as darker areas. In the figure at the top, the fabrication step before the last milling procedure is shown. In picture c), a clear line of separating phases can be observed. This indicate that the small hard islands submerged within the matrix, can induce shear deformation mechanism to the pillar, if the pillar is to cross this slip line in its axial hight. This has also happened for the case of c). The corresponding final pillar of d=200nm is shown in the bottom picture. The slip lines of different phase can be observed at the bottom of the pillar. These slip lines are present in most of the cases of fabrication of grain interior pillars. This can also be observed in the pillar of d=500nm. In the MA-phase, there are no distinct slip lines present. Picture a) indicate a more complex structure, where four lines are crossing each other and hence impeding each other. The resulting pillar is shown in the lower picture a). Present also in this pillar, which is 500nm, are some chaotic slip lines. The corresponding smaller pillar, d=200nm, in picture d), seems to be at a critical size, where the effect of these slip lines do not interfere the pillar along its hight. This can be the reason why the smaller pillars exhibit higher strength. It can also explain why two different deformation mechanisms are present in the compression results. Based on this observation, it seems that the natural deformation of a pure MA-phase would be uniaxial flat compressed, activating several planes, while the effect of crossing planes of a different orientation or phase along the pillar hight induces shear along a specific plane. As this figure represent the 10 sec sample, a similar situation is found in the 5 sec sample. In fig. 3.10, similar phase transition lines can be observed within pillars, in this particular case, the pillar size is 1um. As the pillar size is reduced, the line presence is reduced.

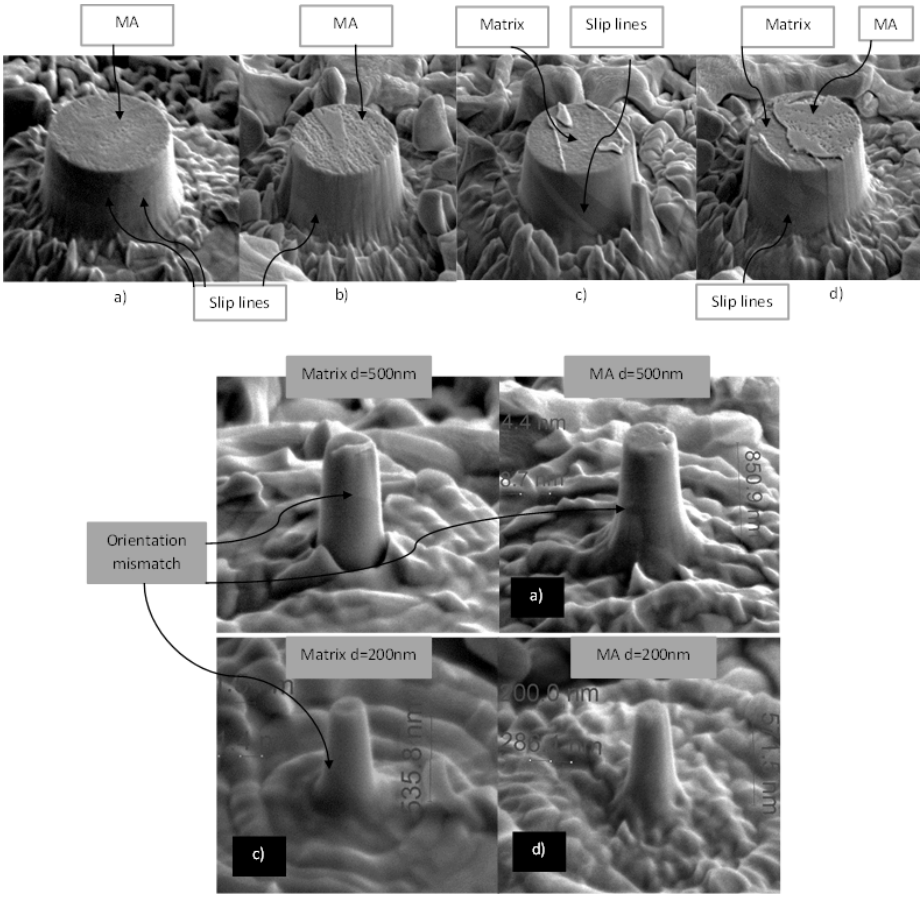

Figure 3.9: Phase transition lines in the 10 sec sample

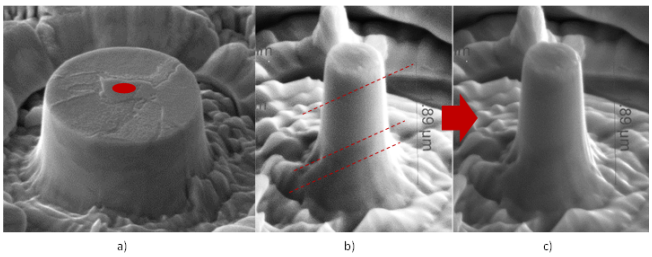

Figure 3.10: 1um Pillar located in a MA-particle of the 5 sec sample. a) Different phases can be observed. b) Highlite of phase lines c) Resulting pillar with induced strain gradients

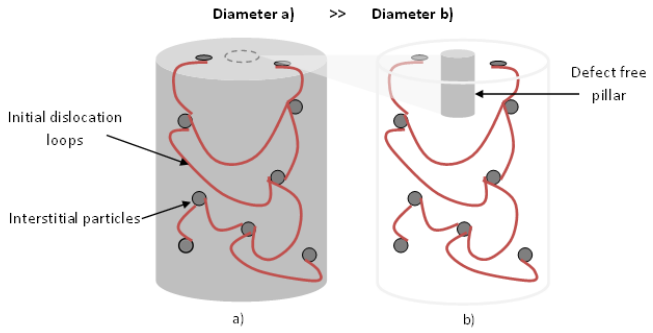

Figure 3.11: a) Particles impeding dislocation movement. b) Decreased pillar size, initial dislocation free

It is suggested that there is a critical pillar size for which below this size, the deformation mechanism is dominated by another factor than for bigger sample sizes. Different approaches to the observed size effect are oppposed and discussed below.
MA-particles are brittle and expected to increase the strength. This can also be confirmed by the stress-strain curves when comparing the MA-phase with the stress-strain curves from within the grain interior. As the depth of the MA-particle is unknown, the strength increase at small pillars can be due to the fact that the pillars are totally submerged of the MA-phase, while bigger pillars might just contain fractions as it does not submerge the hole pillar hight. Another suggestion involves the possibility of an artifact caused by implementation of Ga ions during fabrication with FIB. This will influence a thickness of some nanometers of the surface layer, and as the ratio of area to volume of the pillar gets high, the influence will begin to dominate the strengthening mechanism of the pillar. The potential influence by FIB damage is discussed earlier in this thesis.
It can be argued that dislocation starvation is dominating the sudden size effect at decreased pillar diameter. As the volume of the pillar is reduced, dislocation density is reduced, making dislocation multiplication difficult, as they escape to the surface of the pillar in an early stage after initiation, this is illustrated in fig. 3.11. As this theory is attributed to fcc metals (by Greer et al.), it has to be questioned. This is because martensite is more likely to be hexagonal closed pack, HCP, or a intermediate one, between fcc and bcc lattice, where lattice geometry constants a is unequal to b (while $a = b$ in bcc, see fig 3.12). Portions of bainite acicular microstructure can also be found, which commonly consists of cementite and dislocation-rich ferrite. The high concentration of dislocations in the ferrite present in bainite makes this ferrite harder than it normally would be. The structure is thus an intermediate one as well, neither fcc or bcc. But it is initial pre-strained by dislocations, distributed randomly within the pillar. This can in fact result in small dislocation free volumes. If some of the smaller pillars are located within this dislocation free volume, the dislocation starvation theory yields for the sudden increase in strength at reduced pillar size.

If one can assume that the interstitial islands is harder than the surrounding matrix, this would indicate an increased initial dislocation density. Because the tendency of increased strength is first pronounced in pillars of 250nm, the theory of dislocation starvation can only yield (to a certain degree) if the average dislocation spacing is found to be above 250nm, or that the smallest line segments are larger than 250nm. This would thus leave the smaller pillar in an initial dislocation free state, whereas further dislocation movement would need to be activated by new sources, e.g. Frank Read sources or kink nucleation at the pillar surface. As a result of image forces, it is suggested that dislocations are attracted to the free surface as the pillar diameter is reduced.

Because the resulting post-compressed pillars exhibit deformation mechanisms which can (in a very limited degree) be compared with two different orientations for bcc-fe ((111) and (110)), combined with the fact that the microstructure is not purely fcc, it is highly possible that the dislocation interactions are dominated by those of screw character. As edge dislocations escape quickly to the surface, screw dislocations are left within the pillar interior, moving on slip planes according to kink nucleation and cross-slip. In the MA-phase, the microstructure is complex because the lattice structure do not have a long range order. Activation of several slip planes in different directions, will intersect and impeding each other from further screw dislocation movement. A severe amount of cross-slipping, together with short dislocation line segment interactions, will increase the strength of the pillar. As there are no long-range order, the deformation mechanism will represent an average of the chaotic intersected glide planes, making the pillar compress uniformly axial. As the pillar diameter is reduced, the length of the dislocation pathway is reduced. To overcome an obstacle, i.e. the energy required for a single screw dislocation to cross-slip on to another plane, an amount of thermal energy in the form of increased applied stress, is hence necessary. There will be exhaustion of strain bursts as the applied stress reaches this critical energy for a dislocation to overcome the Peierls barrier. Because the amount of complex and available slip planes are high in the MA-phase, the strain bursts are not as prominent as for the matrix. In the matrix, the structure is less complex, due to reduced amount of MA-phase. Hence, there will be favourable slip planes, for where the screw dislocation can move to generate further deformation. The relative amount of energy required is lower in the MA-particle compared to the matrix, because of the amount of available slip systems. Though, the strength of the MA-phase is increased compared to the matrix, because the heavily amount of intersecting dislocation line segments, impeding each others further movement. The stress-strain curves for the smallest pillars located in the grain boundary thus exhibit a smoother curve, compared to the increased jerky behavior of the matrix curve. The size effect is not prominent until the pillar diameter approaches 200nm, whereas the affect of initial dislocation density is pronounced.

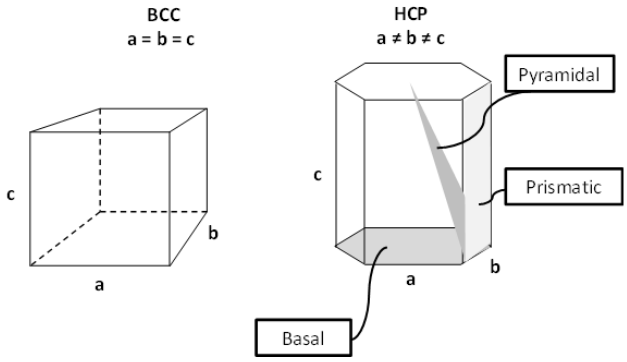

Figure 3.12: Simple lattice geometry of bcc and hcp with slip plane system of hcp

The situation is also attempted to be approached by the Geometrical Necessary Dislocation theory 2.6. This coupling leads to reduced lattice rotations and plastic strains in the region of highest heterogeneity. These regions would be close to the martensite/bainite matrix/particle interface and within the MA-phase. In the latter asessment of the dislocation mechanism, deformation was assumed to behave in a quite similar matter as bcc crystal. In this approach, the lattice structure is assumed to be an inmediate one, between bcc and fcc, i.e. a hcp like-crystal. The slip anisotropy in hcp-like crystals is significantly different from that in fcc and bcc systems because of the lattice geometry c and a, as illustrated very simply in the figure 3.12.

Hcp-type slip has differing Burgers vectors and vastly different critical resolved shear stresses. Slip hence occur on basal, prismatic and pyramidal slip systems. The maximum number of screw-type dislocation systems for the hcp crystal type is nine, if dislocations of opposite sign are not differentiated, which is less than for bcc. The number of edge-type dislocation systems is always equal to the number of active slip systems. This indicates that the deformation mechanism is dominated by an edge character, as for fcc metals. Upon cooling of the F70 steel, the mismatch in thermal expansivity between the MA-particles, the carbide particles and the matrix leads to the establishment of thermal strains and hence stresses. If the difference in expansivity is large enough, it will cause the development of plastic strains local to the particles. As a result of the heterogeneous nature of the material geometry, considerable variations in strain gradients develop. Hence, corresponding variations in lattice rotation and GND development will as a result be present. By the combination of edge dominated dislocations and an initial amount of GNDs present pre-compression, the strength of the material will increase. The edge dislocation will move according to the Peierls stress, crossing obstacles along the way, by a continously desire to lower its energy. As it has to cross from one Peierls energy minima valley, to the next, i.e. overcome an obstacle (which can be cross sectioning gliding planes within the MA-phase), it has to be attributed the Peierls barrier stress. This transition from one Peierls valley to the next, is thus called a geometrical kink. As the kink is dependent of long range order to move fast, and a symmetric position between its neighbouring plane, it will be impeded by the complexity of intersecting planes within the MA-phase. Therefore, it is expected that edge dislocations will pile up as kinks. At a critical pillar diameter, when the relative density of available edge dislocations is low, the reduced amount of geometrical necessary kinks within the pillar volume

needs to be attributed an increased amount of thermal energy to jump to the next Peierls valley.

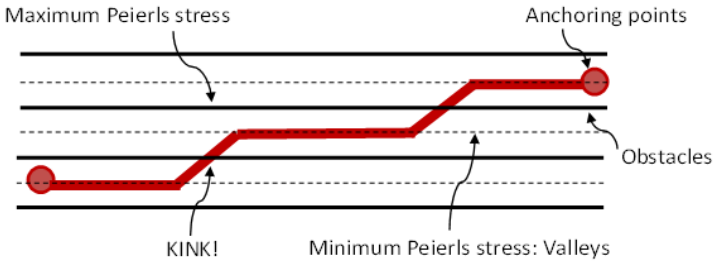

Multiple theories can be suggested to explain the feature of the post-compression stress-strain curves. When no interfaces are present, dislocation pile-ups form near the boundary surface, inhibiting further dislocation nucleation. Addditional elastic straining is required to overcome this back stress. Contrary, when the interface is more compliant, the back stress is reduced, and hence the size effect it reduced. Hence, size effects significantly reduce as interfaces become more compliant! As this steel is a complex alloying metal, it it crucial to understand the fundamental strengthening behavior at small-scale for pure materials, orientations and phases. When a reliable validated theory is well-established, both for bcc and fcc, it can be applied to more complex structures. It should then be possible to predict the complex material behavior, approaching the problem from a bottom-up perspective. Hence, the resulting conclusion of why the smaller pillars exhibit a pronounced strength increase, thus remain an unsolved question.

3.2 EU Project: MultiHy steel

Two samples for the EU project MultiHy, were investigated: one with 0.005wt% Nb and one with 0.0wt% Nb. Niobium is hence the only varying alloying component, which in turn will cause the mechanical behavior, as well as the microstructure, to differ in between each other. The steel investigated consist of two phases: martensite and ferrite. The volume fraction of each phase is measured roughly to be about 50%. The aim is to investigate the mechanical properties in single slip orientation ferrite grains, by using EBSD maps to fabricate FIB pillars. For this work, compression of ferrite pillars is the main focus. In further work, carried out by Afrooz Barnoosh, these pillars will also be hydrogen charged and compressed in electrolyte. This is to investigate the effect of hydrogen diffusion into the microstructure, and to determine wether or not Nb is beneficial due to the material strength and embrittlement.
In the present work, pillars are also been tested in the martensite phase of Nb5, to be able to compare it to its ferrite conterpart, and also to the MA-phase in F70. The ferrite phase can thus be compared to the single slip phase of bcc-Fe.
In addition, pillars of 500nm, in both Nb5 and Nb0, have been compressed with a varying loading rate of 50μN/s, 100μN/s and 500μN/s, to investigate the latter effect on the resulting strength. A size effect trend (if there is any), can hence also be investigated, though there are few tested parallels to be compared.

3.2.1 EBSD

Several EBSD maps were made, where the only grain orientation of interest is the single slip orientation of (5 2 11). The tolerance angle between adjacent grains are of 2%, which should result in very similar deformation mechanism in all the grains. The corresponding IPF and SEM map are visualized in fig. 3.13. The dark areas seen in the IQ map c), represent martensite phases, which are not indexed by the software. Because the microstructure of martensite is very chaotic and complex with no long-range order of the lattice, it is almost not possible to index. Pillars compressed in these areas will hence represent an average internal complexity, without any specific glide plane to be activated. If the pillar size is reduced, defined glide planes of high schmid factor can, though, be activated.

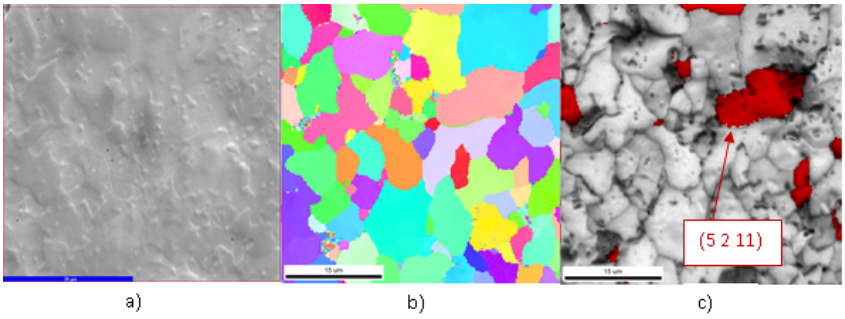

Figure 3.13: a) SEM b) IPF map c) Highlight crystal orientation

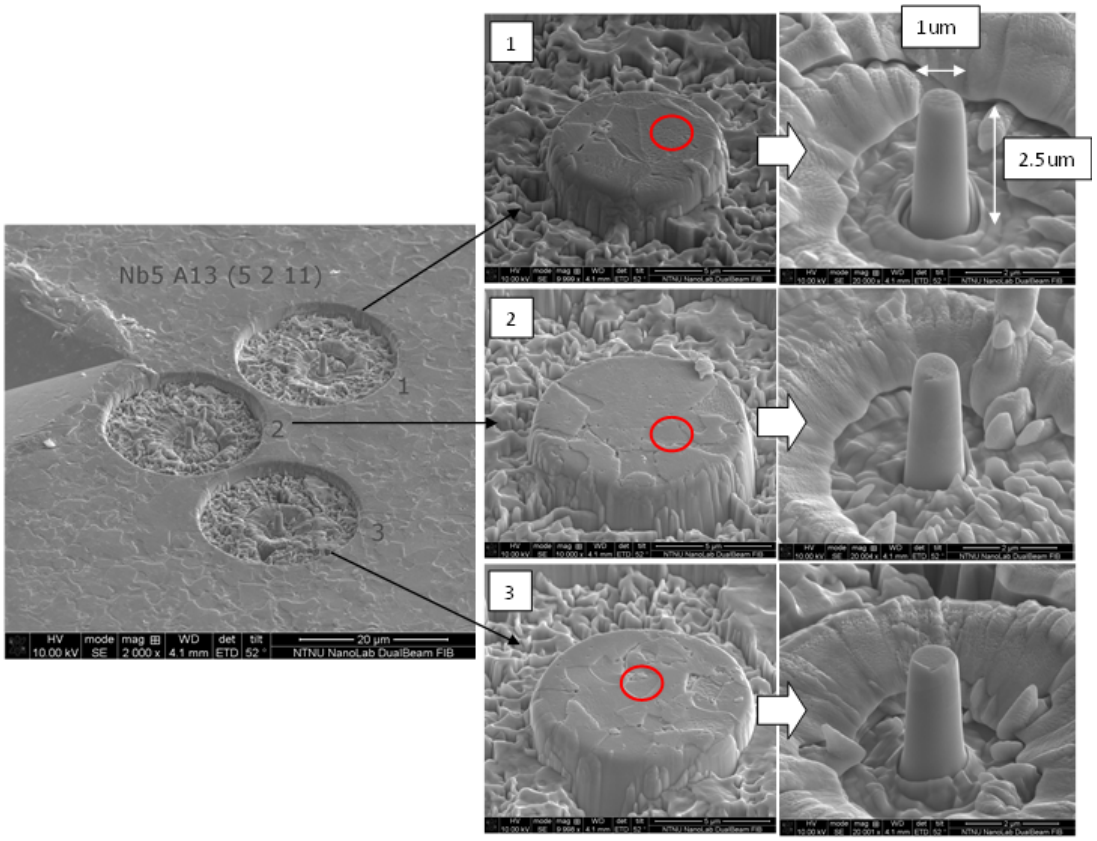

Figure 3.14: Pillar fabrication in (5 2 11) oriented ferrite grains in Nb5

3.2.2 Pillar Fabrication

Pillars located in the single slip ferrite phase of (5 2 11), are carefully placed within the correct grain of interest, as shown in fig. 3.14. In the SEM, the IQ map and IPF map are used as navigation references, so that pillars are placed in the correct grain with the correct orientation. This procedure is illustrated in fig. 3.15, where three ferrite pillars of d=1μm, and h/d ratio of 2.5, are placed within one single EBSD map, in grains of orientation (5 2 11). The system variables used for this fabrication are presented in appendix 1.

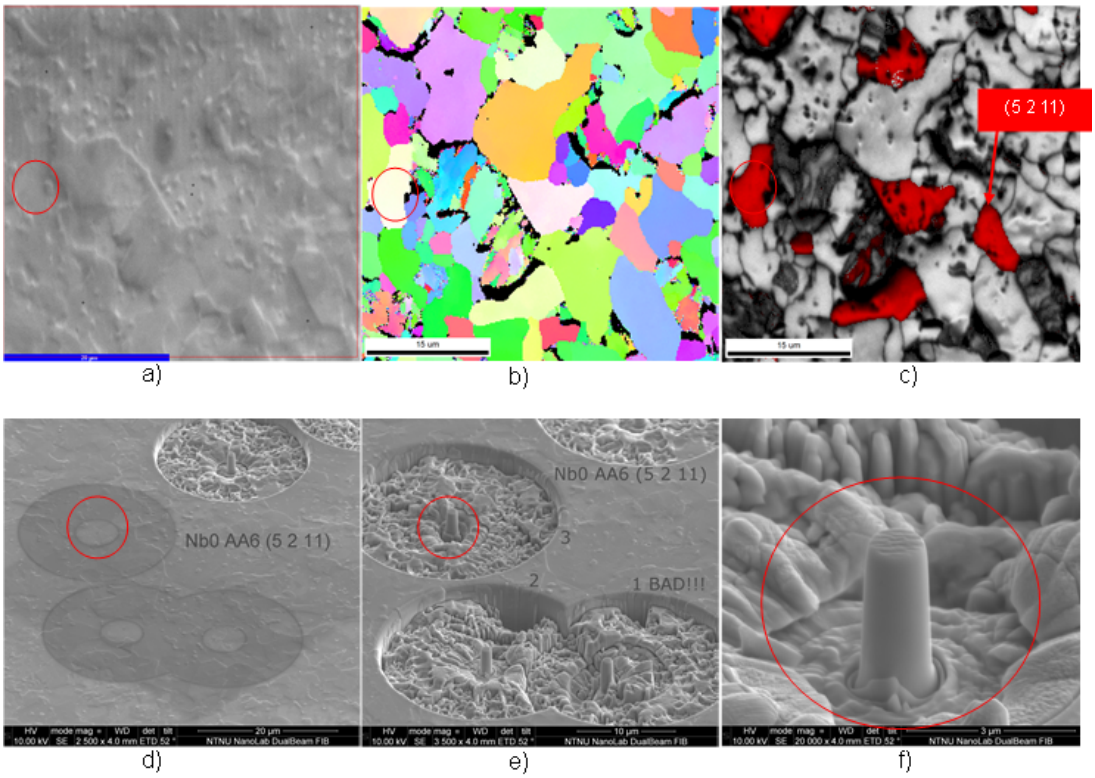

Figure 3.15: Pillar fabrication in (5 2 11) oriented ferrite grains in Nb0: a) SEM b) IPF map c) Highlight of (5 2 11) d) Pillar location e) Fabricated pillars f) Pillar

3.2.3 Results MultiHy Dual Phase Steel

The dual phase steel of hard martensite and soft ferrite, combines the ductility of ferrite with the brittleness of martensite, to form a high strength steel. Ferrite deforms as a result of plastic constraining of martensite and thus excessive load is not applied to the ferrite during plastic deformation. Hence, the ductile phase introduce a stress relief effect, which in turn increases the toughness.

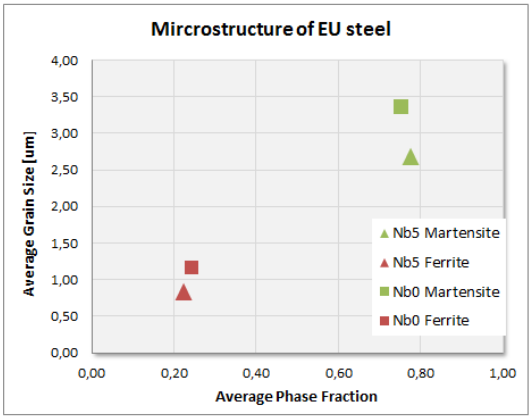

Figure 3.16: Measured grain size and phase fraction in each sample

In fig.3.16, the fraction of the two phases present in the microstructure is quite similar for both Nb0 and Nb5, about 75% martensite and 25% ferrite. It is seen that Nb5 has a slightly larger fraction of martensite and a slightly lower fraction of ferrite. Though, the main difference observed in this figure, is that the grain size is lower in both phases for Nb5. The average grain size is 2.7um in martensite and 0.8um in ferrite for Nb5, compared to 3.35um and 1.2 in Nb0 respectively.

In the present work, pillars of 1um have been investigated in both the ferrite and martensite phase. It was, in addition, carried out compression of 500nm pillars in the ferrite phase, with varying loading rates, to investigate the latter effect.

Niobioum has a high melting temperature, and it is commonly added for strengthening purposes. The strength increase is due to altering the microstructure by producing a very fine dispersion of alloy carbides in an almost pure ferrite matrix. This eliminates the toughness-reducing effect of a pearlitic volume fraction yet maintains and increases the materials strength by refining the grain size. The grain size refinement is clearly evident in fig. 3.17 for Nb5. As the amount of Nb is the only variation factor, this refinement is hence exclusively caused by this alloying element. Both the martensite grain size and the ferrite grain size is reduced due to fine Nb dispersion in the microstructure. This will enhance the material strength, as well as the ductile properties, compared to the sample without Nb. Together with the grain size difference, small rounded particles or inclusions can be observed in the ferrite phase of Nb0. These can not be observed in the Nb5, and is thus not carbides of Nb. These particles remains an open question.

The Post-Compression results from the ferrite phase of orientation (5 2 11), indicate that the strength, as well as the toughness is increased for Nb5, compared to Nb0. This result is also expected. The resulting stress-strain curves are plotted in fig. 3.18. It is clear that the ductile properties of Nb5 is significantly increased compared to Nb0, together with the increased yield strength of first slip. The slip yield stress, σ_{slip}, for Nb5 varies from 600MPa to 800 MPa, while the corresponding stress is around 500MPa for Nb0. The superior mechanical property in the fine grained Nb5 steel can be explained by the extensive strain hardening from the onset of plastic deformation by the presence of mobile dislocations with high density, including grain size independent strain gradient plasticity, i.e. GNDs.

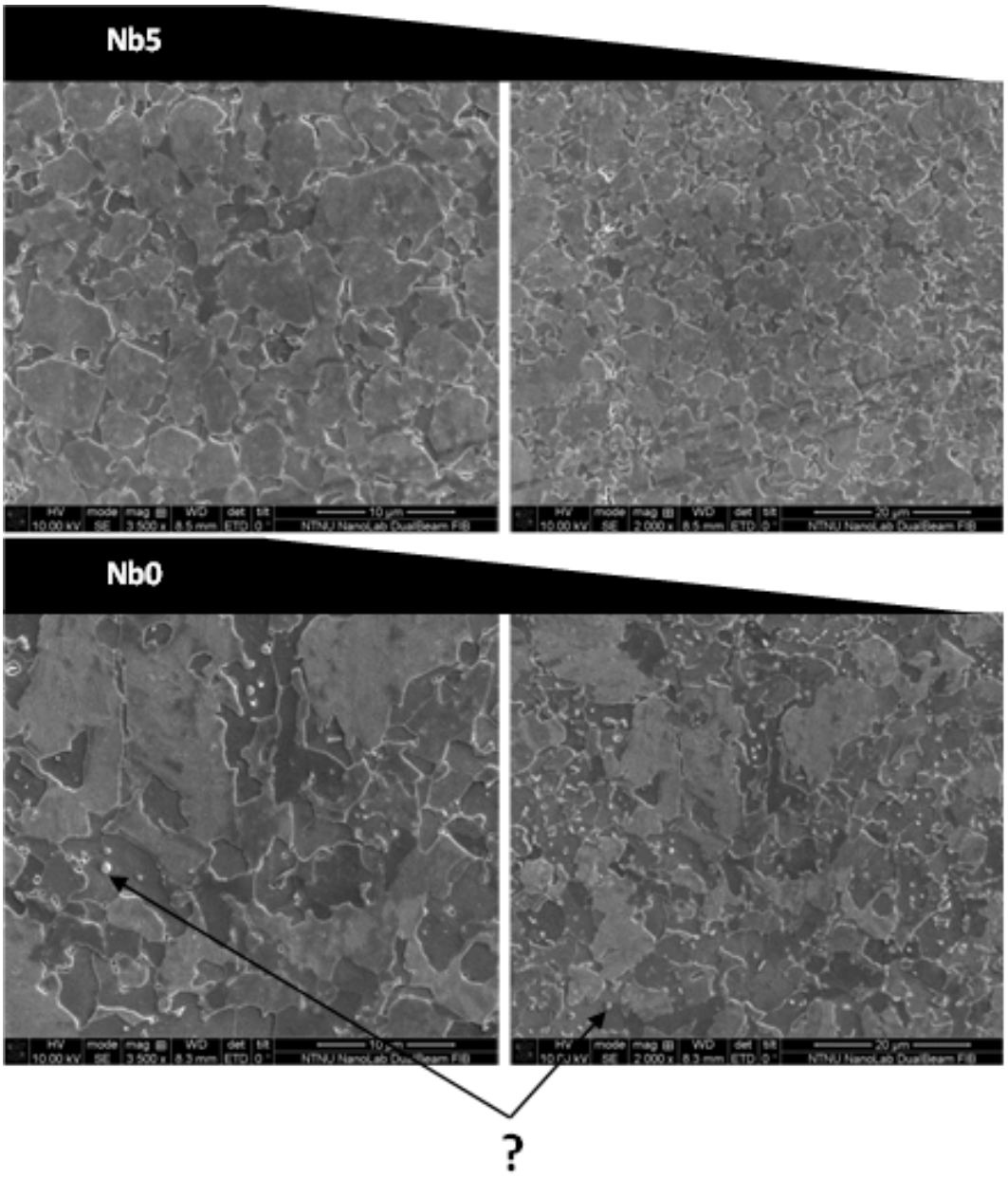

Figure 3.17: Different microstructure due to alloying Nb. What are these intermediate particles?

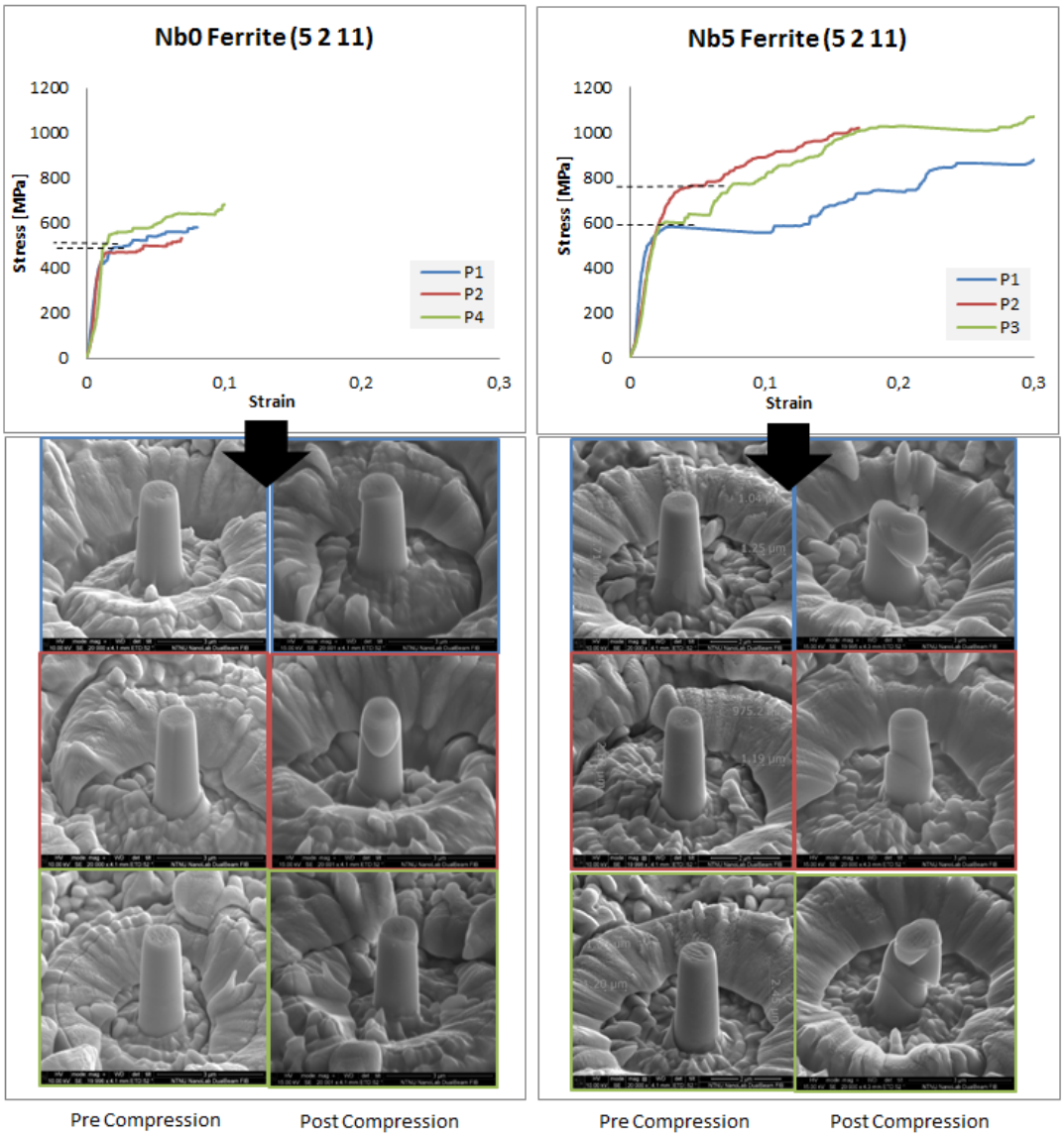

Figure 3.18: Stress-Strain Curves for Nb0 and Nb5 with d=1um, with corresponding pillars Pre- and Post-Compression

In fig. 3.19, the post-compression results for Nb5 and Nb0 are presented, at which pillar with diameter = 500nm corresponds to the red curves, while d = 1um corresponds to the green curves. In the case of Nb5, there is a slightly tendency of the smaller sizes exhibiting a higher strength than for its counterparts of 1um. The trend is not as pronounced as for Fe. The yield strength of slip is higher for the reduced pillar sizes. What makes this tendency interesting, are the results from Nb0. The situation is quite opposite: The yield strength of the smaller pillars are quite similar to their bigger counterparts but at very high strains. These two opposite situations makes it difficult to evaluate the size effect.

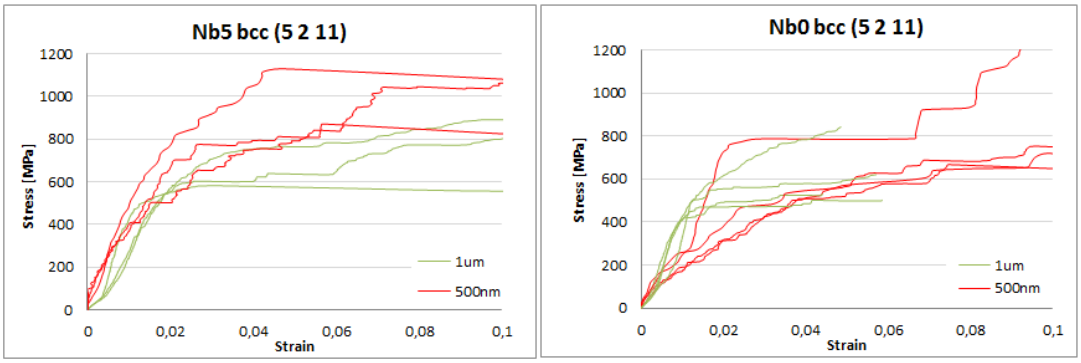

Figure 3.19: Post-Compression results for Nb0 and Nb5, with d=500nm (red) and d=1um (green)

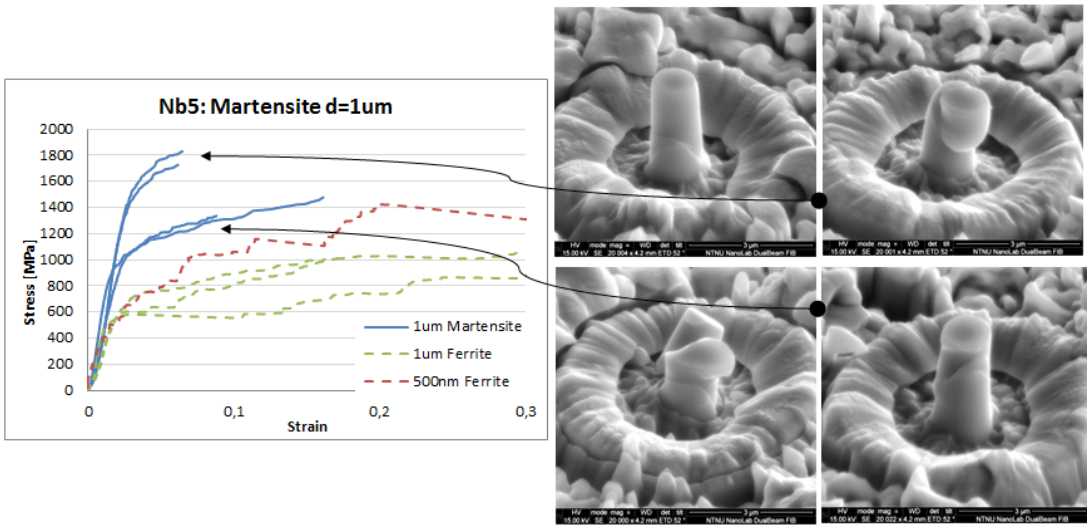

Figure 3.20: Post-Compression results in Martensite phase of Nb5, d=1um

The Post-compression results of four pillars which are located in the martensite phase of Nb5, are presented in fig. 3.20. As expected, the martensite exhibit an increased yield strength, compared to its ferrite counterpart curves. Martensite is hard and more brittle compared to the ferrite matrix. These hard islands increase the strength of the material, by introducing a complex lattice structure, which can be described as a hcp lattice. The martensitic phases introduce strain gradients and a high initial dislocation density, i.e. GNDs ([2]). The strength increase can thus be explained by the formation of sessile locks, impeding dislocation movement. Dislocations will pile up at such obstacles, which there are a lot of. The lattice structure makes it hard for dislocation movement, as they lock each other, and hence the amount of necessary thermal activation is increased.

Dual phase steel is traditionally known, in a macroscopic level, to have a high strain rate sensitivity, which means that a the higher strain rate, the more energy it absorbs. The present experiment at sub-micro scale can not support this macroscopic fact. Pillars of diameter 500nm placed in the ferrite phase, were tested with varying LR. In fig. 3.21, the results from this small experiment indicate that the strength of the pillar is not affected by the LR, though, the span of the two peak rates is only 450uN/s. These LRs are very slow, compared to atomistic (and to macro scale), hence, it is not expected that the pillars would be affected in any way by the LR in this range. For Nb5, the LR was changed from 50μN/s, 100μN/s to 500μN/s. The stress at which first observable significant slip occurs, is in fact increased at high LR, but the curves overlap each other more or less after this. At LR = 500μN/s, the slip yield is 1100MPa and 800MPa for Nb5 and Nb0 respectively. For LR = 50μN/s and 100μN/s, the corresponding slip yield is approximately 800MPa and 500MPa respectively. Though, the overall trend is that Nb5 exhibits an increased strength compared to Nb0, for diameter of 500 as well as diameter of 1μm.

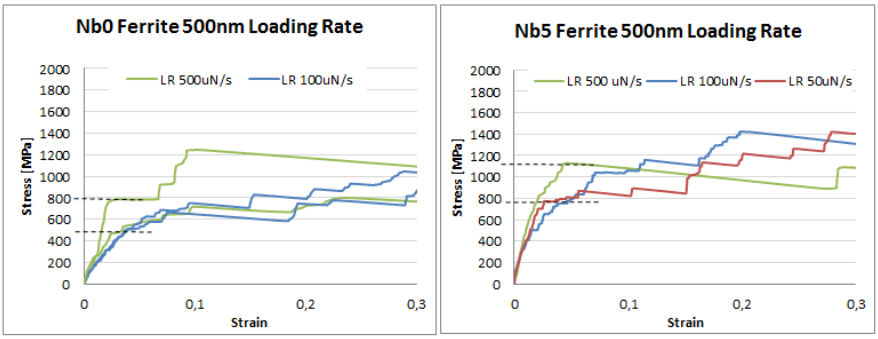

Figure 3.21: Loading Rate sensitivity

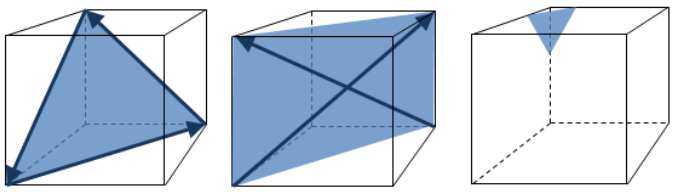

Figure 3.22: Orientations and slip system for BCC iron. a) (111) b) (110) and c) (235)

3.3 Size-Effect in Single-Crystal BCC-Fe

Four pillar diameters have been investigated: D = 100nm, 500nm, 1000nm and 2000nm. For each pillar size, three crystallographic orientations were investigated. The orientation planes are aligned parallel to the flat Bercovich indenter tip during compression. The planes compressed in the BCC lattice, are the multiple slip systems of (111) and (110) and the single slip plane (235), illustrated in fig.3.22. The material is 99.998% pure Fe. The size effect is investigated in the absence of strain gradients and hard interfaces. The effect is also investigated in correlation to single- and multislip deformation.

3.3.1 EBSD

The electropolished Fe surface was scanned by EBSD, and indexed with the reference phase of α-iron. The index of fit was around 0.8-0.9, indicating good quality indexing results. The areas scanned, were processed with OIM, where the grain orientation of interest was found and highlightened. An example of the process is shown in fig.3.23. The IPF map a), is compared with the corresponding SE image b), and the grains and areas are recognized. By creating a new IPF map, of which only grain orientation (235) is shown, is then created, c). The colour scale bar in d), indicates that darker grains are more likely to have the exact orientation of interest, where the misalignment between grain boundaries are restricted to 10 degrees.

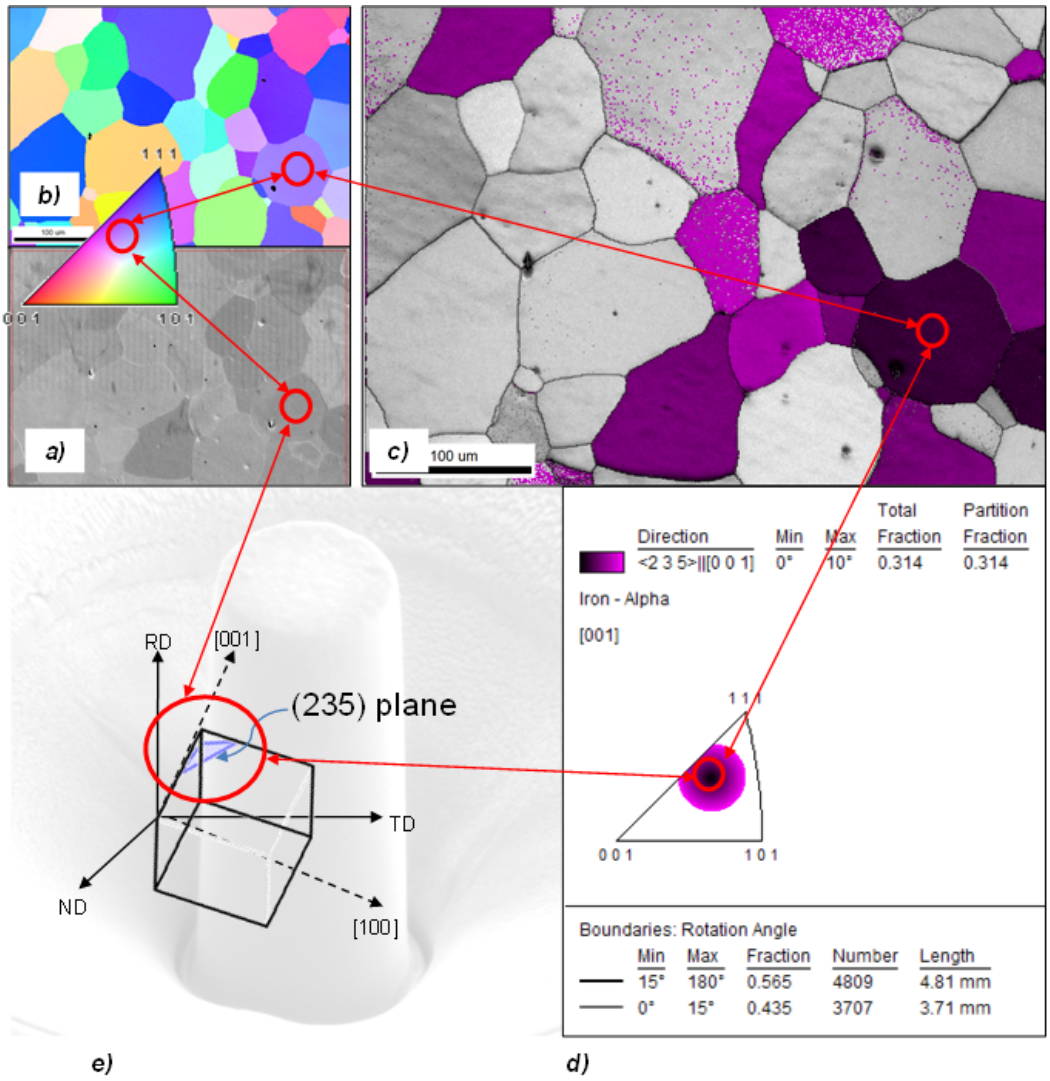

Figure 3.23: OIM: a) SEM b) IPF Map c) IPF Highlight of (235) orientation d) IPF of (235) e) Corresponding crystal plane

3.3.2 Pillar Fabrication

From the EBSD maps, where the desired grain orientation was highlighted, corresponding areas were found in SEM, where pillars then were placed in the grain of interest (fig.3.23). Different grain orientations has different sputtering yield, due to the long-range order of unit cells in space, allowing tractions of Ga ions to implement within the interior at various ranges. This was obviously observed during milling, as can be seen in fig.3.24. To the left, the exposed surface orientation is (235), while to the right, the exposed surface orientation is (111). The z value (which indicates the milling depth in μm), is decreased for the (111) orientation, indicating that the amount of implementing Ga ions are high, and the corresponding sputtering yield is low. The lattice is arranged in such a way that tunneling effect occur. These varying z-values need to

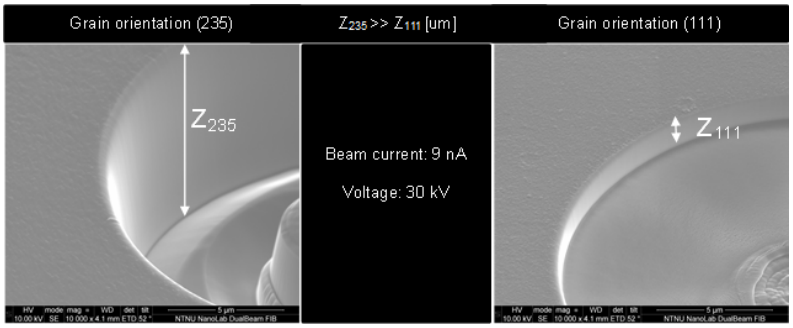

Figure 3.24: Sputtering yield within two different grain orientations

be treated separately due to fabrication process variables. The procedure is done in as few steps as possible, to reduce the probability of FIB damage. After trial and error, good procedures were established to ensure proper h/d ratios, which were desired to be 2-2.5. The procedure and corresponding system variables can be seen in Appendix 2. The pillar fabrication of four different pillar diameter sizes, compared with three different orientations, resulted in a total of 48 fabricated pillars. The typical pre-compression pillars of various sizes and orientations are presented in fig.3.25 The taper angle was measured to be . It is aimed for to be less than 2 degrees, so that the calculated stresses and deformation mechanism of the pillars are not affected by increased cross-section area along the axis of its hight. If the taper angle is large, it will affect the stress-strain curves, as shown in fig.**??** (This figure is taken with permission from the final exam results for Atomistic Modeling NTNU 2012, made by Dr. Ersland). The taper angle was measured to be in the range of 2 - 6 degrees, where increased pillar diameter results in a decreased taper angle. At reduced taper angles, pillar cross section will hence be constant due to the hight, and the resulting stress-strain curves resembles the real values. As for the small pillars, where the cross-section increase along the negative hight, the conventional stress-strain calculations done in this work, results in an enhanced size effect. The result is presented in the figure to the left.

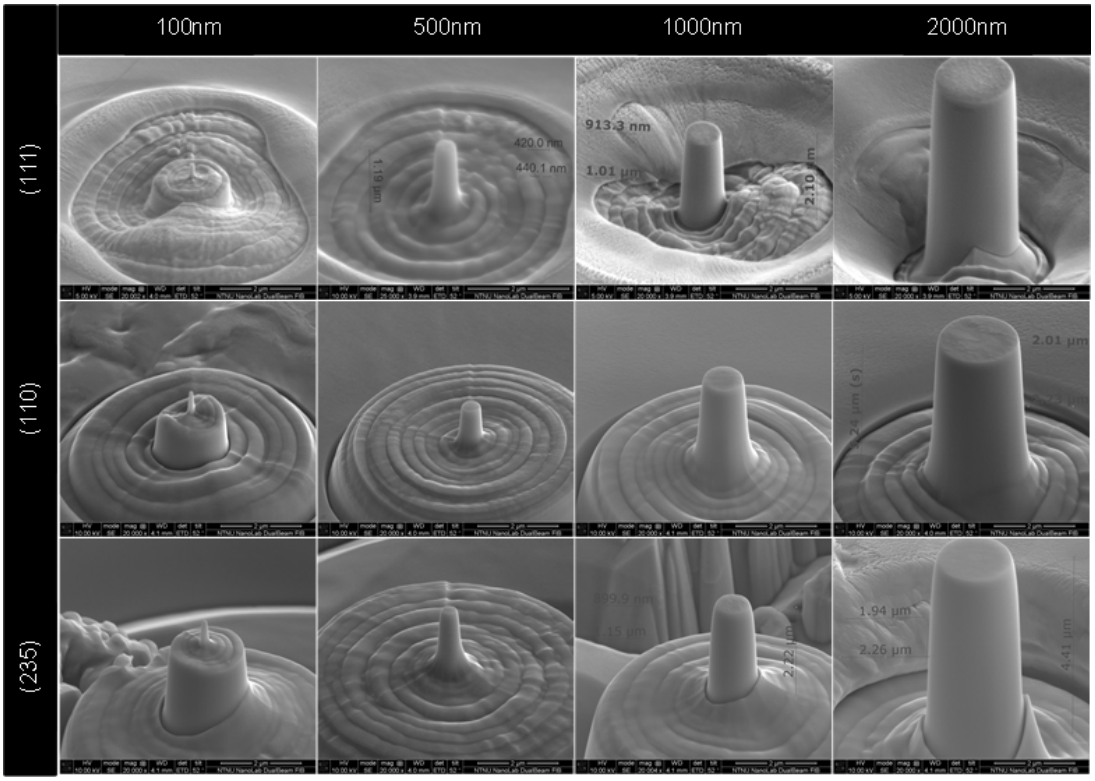

Figure 3.25: Fe Pillar fabrication with four diameter sizes and h/d ratio 2-2.5

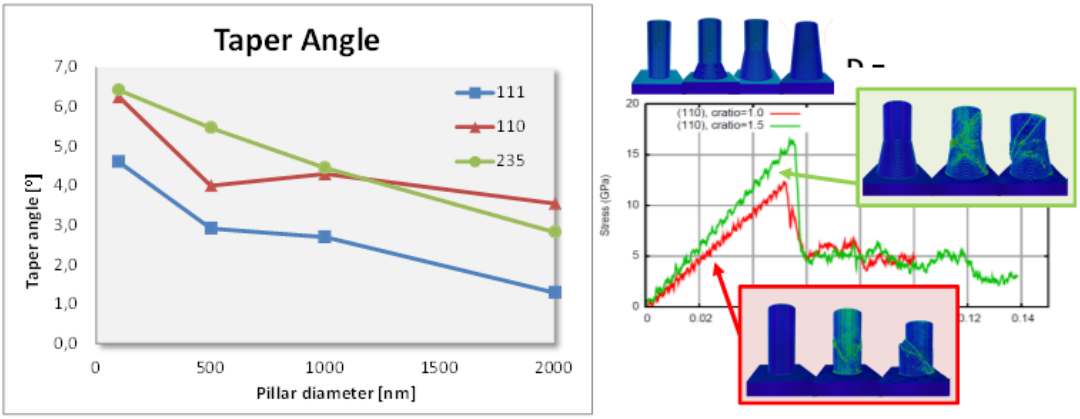

Figure 3.26: Left: Measured Taper angle of bcc-Fe pillars. Right: Atomistic simulation of compression (110) pillars with d=100Å, and different taper angles

3.3.3 Nanocompression

The post-compression results can be seen in fig.3.27.The load function used is presented in table below, 5.1. Some of the pillars were intentionally unloaded two times throughout the experiment. This did not affect the final results in any way. The uncertainty at initial loading between the

Table 3.3: Load function: Open Loop

D_{pillar} $[um]$	$LoadingRate$ $[\mu N/s]$	$PeakLoad$ $[\mu N]$
2	100	5000
1	50	2500
0.5	25	1000
0.1	10	500

pillar top and the punch tip, results in an unambiguous determination of the yield point at low strain values. As each load-displacement curve exhibit variable initial slopes at the elastic region, each individual curve was manually put to an offset strain value between 0.2-0.4% strain. This was done to eliminate the affect from initial unstable contact between pillar top and the flat punch tip. An example of this 2% yield determination is shown in fig. Within the region of elastic to plastic behavior, the yield point, $\sigma_{y2\%}$, is determined to be at 2% strain. At this point, there is full interface contact between the punch and pillar, and the stochastic nature of strain bursts do not obscure the determination. In addition to $\sigma_{y2\%}$, the point of which the first observable slip occurs, seen as strain bursts in the stress/strain curves, is determined for each pillar. The yield strain thus varies with orientation and pillar size. The yield of glide should also not have a large scatter for within each orientation and pillar size, to confirm that the results are valid and repetitive. The power law size effect has proven to be consistent for simulations and experimental compressions of fcc metals. For bcc-Fe, the following power law is used to describe the material bahvior at different pillar sizes:

$$\tau_{CRSS} \propto D^n, \tag{3.1}$$

where τ_{CRSS} is the critical resolved shear stress at which the slip system mechanism is activated, the integour n is a plasticity power law exponent, and D is the pillar diameter.

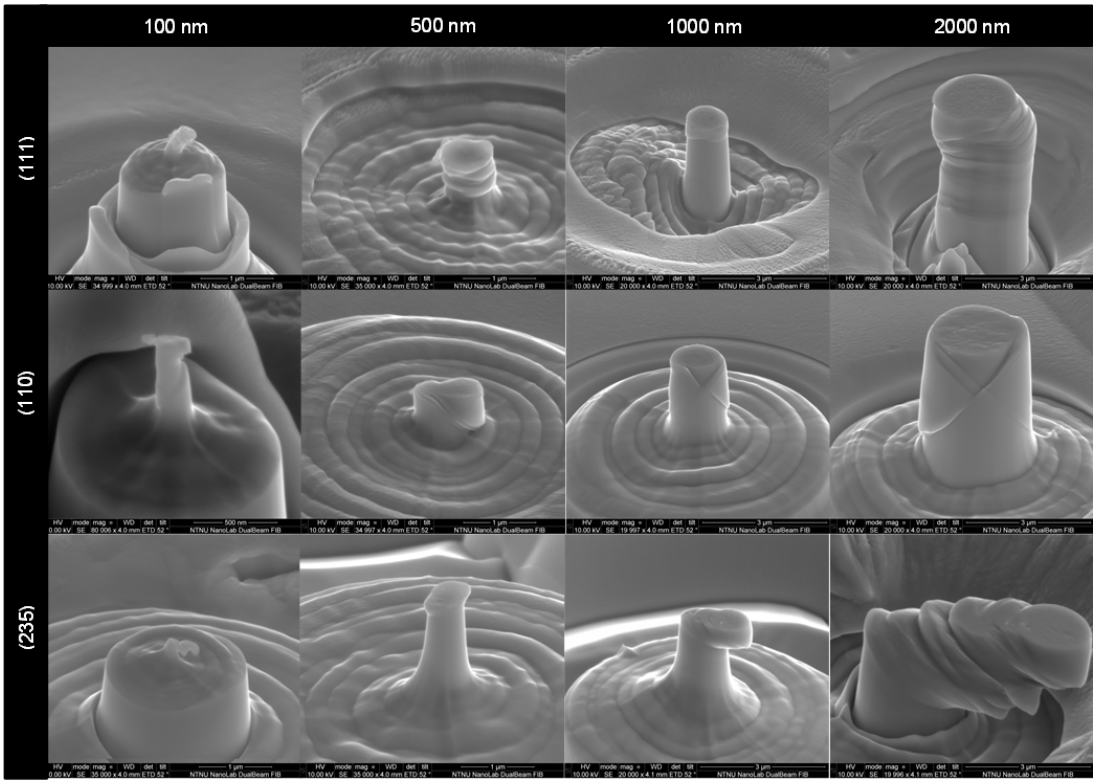

Figure 3.27: Slip mechanism for Fe pillars of (111), (110) and (235) orientations

3.3.4 Results Fe

This study on single crystalline bcc-Fe, aims to investigate the effect of orientation on the size dependence. Regardless of pillar size, the (110) and (111) pillars exhibited slip along multiple systems, while the (235) pillars exhibited primarly single slip along a preferred slip system, fig.3.27. This indicate that dislocation interaction is not the prominent dominating factor regarding strain hardening mechanism in Fe. Results from 100 nm pillar for (111) is not valid and therefore excluded from this thesis throughout further analysis. It can thus just be a speculation of how high the shear strength of these small pillars in this orientation is.

Stress at an axial strain of 2% was chosen as an representation of yield stress as it is high enough to ensure that plastic deformation has occured, but still, low enough to ensure a limitation of the effect of strain hardening. The point of strain corresponding to the first visible slip, varies. This point of primary yield, is denoted σ_{glide} in the figure, for which the strain is not constant due to different sizes and orientations. It is interesting to observe at which stress the first strain burst occurs in the small pillars, while the large pillars do not exhibit these energy exhaustions, the behavior is rather smooth, elastic-plastic transition curves. σ_{slip} is therefore equal to $\sigma_{2\%yield}$ in many cases for the larger pillars.

In table 3.4, the Schmid factors are calculated. The pillars were placed in grains, for which the grain orientation is represented by coordinates given by OIM. The family of orientations are very close to the orientation aimed for, an example is the (111){9 8 9} family. The Schmid factors are calculated for different directions, where the highest factor indicates the plane for which slip activation probably has occured. This factor can then be used to calculate the τ_{CRSS} for the actual orientation of interest. For pillars loaded on (111) planes, the highest Schmid factor is found to be 0.3576 and 0.3629 for the $\{112\}\langle111\rangle$ slip system (see table 3.4). For pillars loaded on (110) planes, the two symmetrical $\{112\}\langle111\rangle$ slip systems also has the highest Schmid factor with a value of 0.4772, 0.4895 and 0.4829, hence it is reasonable that these are the slip systems activated. For the single slip system, loaded on (235) planes, the activated slip planes with the highest Schmid factors, are the $\{110\}\langle111\rangle$ systems. The factor s is 0.4582, 0.4561. 0.4528 and 0.4917 for the latter system. These results indicate that pillars loaded in (111) planes should exhibit increased strength compared to both the(110) and (235) planes. This is also the case, when comparing the stress-strain curves. (Schmid factor values are found by PhD. Bjørn Rune Rogne) The stress-strain curves indicate that the (111) orientation is the stronger configuration, while single slip (235) and (110) has a reduced resistance to deformation. This can also be expected from the calculated Schmid factors due to the orientations.
When calculating the critical resolved shear stress, τ_{CRSS}, the activated gliding plane is thus determined to be the {112} plane for (111) and (110) and the {110} plane for (235), which value gives the higher Schmid factors: $s = 0.36$, 0.48 and 0.46 for the (111), (110) and (235) orientation respectively. The stress at which the glide plane is activated, σ_{glide}, is multiplied with the corresponding Schmid factor, to determine the critical shear stress for when plastic deformation occurs. The size effect is presented as a function of τ_{CRSS} and pillar diameter in fig.3.30.

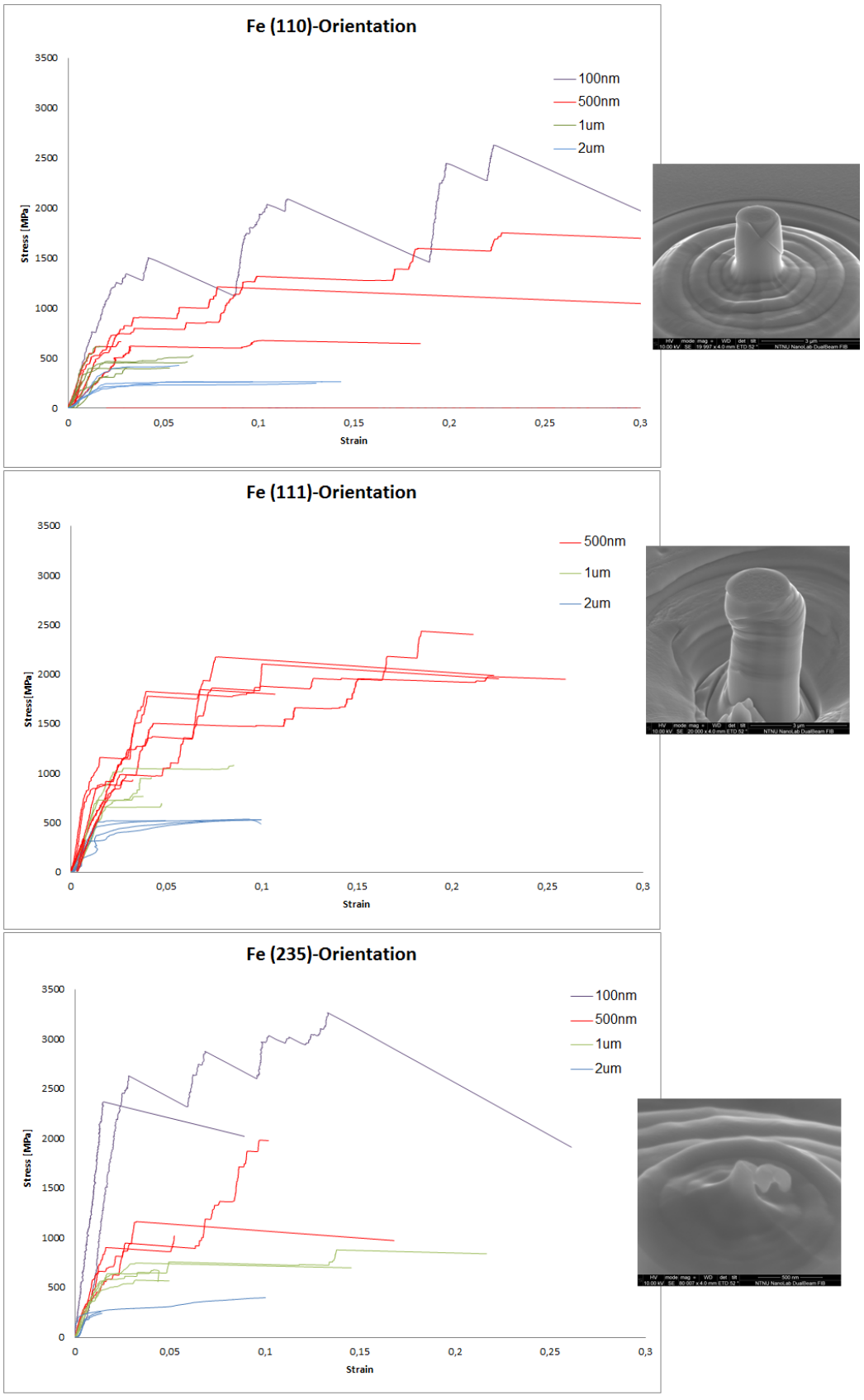

Figure 3.28: Post-Compression results for bcc-Fe and corresponding deformation mechanism

A third and last stress-point of interest, is the point corresponding to the ultimate compression strength, σ_{UCS}. This is to compare the amount of strain hardening from 2% yield and up to a point of where the pillar is nearly totally deformed according to the associated slip plane. In fig.3.29 the amount of strain hardening is presented as $\sigma_{UCS}/\sigma_{y2\%}$. It can be observed that the strain hardening increase as the pillar diameter is decreased. A factor of nearly 1.0 indicates a elastic-ideal plastic behavior, which can be seen for pillars of diameter $\rangle$ 1um.

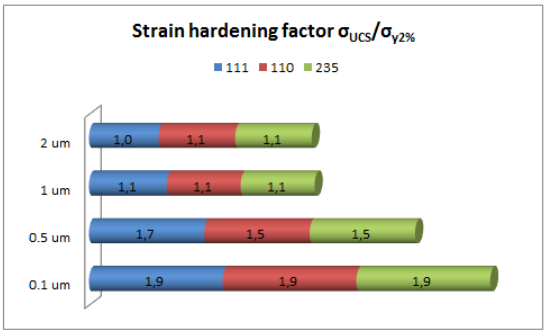

Figure 3.29: Strain hardening

Table 3.4: Schmid Factors for (111) (110) and (235) deformation

Plane	*Plane*	*FamilyPlane Direction*	*SchmidFactor*
(111)	{9 8 9}	{110} ⟨111⟩	0.3071
(111)	{9 8 9}	{112} ⟨111⟩	0.3576
(111)	{16 15 19}	{110} ⟨111⟩	0.3297
(111)	{16 15 19}	{112} ⟨111⟩	0.3629
(110)	{14 1 6}	{110} ⟨111⟩	0.4443
(110)	{14 1 6}	{112} ⟨111⟩	0.4829
(110)	{9 1 10}	{110} ⟨111⟩	0.4441
(110)	{9 1 10}	{112} ⟨111⟩	0.4895
(110)	{17 1 21}	{110} ⟨111⟩	0.4546
(110)	{17 1 21}	{112} ⟨111⟩	0.4772
(235)	{5 3 8}	{110} ⟨111⟩	0.4582
(235)	{5 3 8}	{112} ⟨111⟩	0.4570
(235)	{12 8 21}	{110} ⟨111⟩	0.4561
(235)	{12 8 21}	{112} ⟨111⟩	0.4449
(235)	{13 9 23}	{110} ⟨111⟩	0.4528
(235)	{13 9 23}	{112} ⟨111⟩	0.4411
(235)	{14 3 23}	{110} ⟨111⟩	0.4917
(235)	{14 3 23}	{112} ⟨111⟩	0.4695

In the power law equation, the exponent n describes the size effect dependency, which at low values (more negative) gives a steeper curve when $\log(\tau_{CRSS})$-$\log(d)$ is plotted. A steeper curve thus represent an enhanced size effect. The τ_{CRSS} is plotted against pillar diameter in fig.3.30. In this figure, it is shown that orientation (235) has the lower n-values when comparing to σ_{slip} and $\sigma_{y2\%}$ and thus a more prominent size effect behavior. When comparing σ_{UCS} though, the (111) orientation seems to have a more prominent size effect. These comparisons indicate that the n-value is strongly dependent upon the point of strain where it is calculated. As the pillar size decreases from 1000nm to 100nm, the yield strength at 2% strain is increased by a factor of 3.3 for (110) orientation and 6.4 for (235) orientation. In table 3.5, the corresponding n-values are plotted for σ_{slip}, $\sigma_{y2\%}$ and σ_{UCS}. In comparing these values to the literature, the n-value of 2% strain is used.

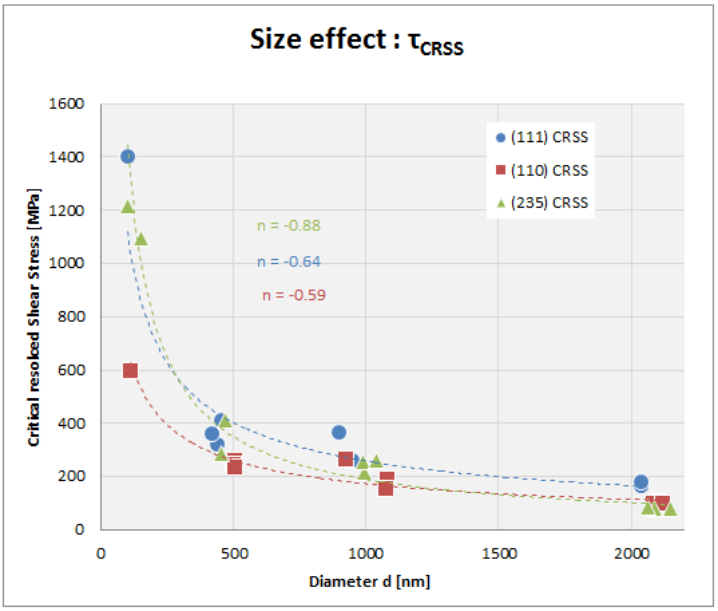

Figure 3.30: Fe-bcc: Size effect due to CRSS, with size dependence exponent n

Table 3.5: n values at σ_{slip}, $\sigma_{2\%yield}$ and σ_{UCS}

Orientation	σ_{slip}	$\sigma_{2\%yield}$	σ_{UCS}
(111)	-0.64	-0.67	-0.98
(110)	-0.59	-0.66	-0.87
(235)	-0.88	-0.76	-0.79

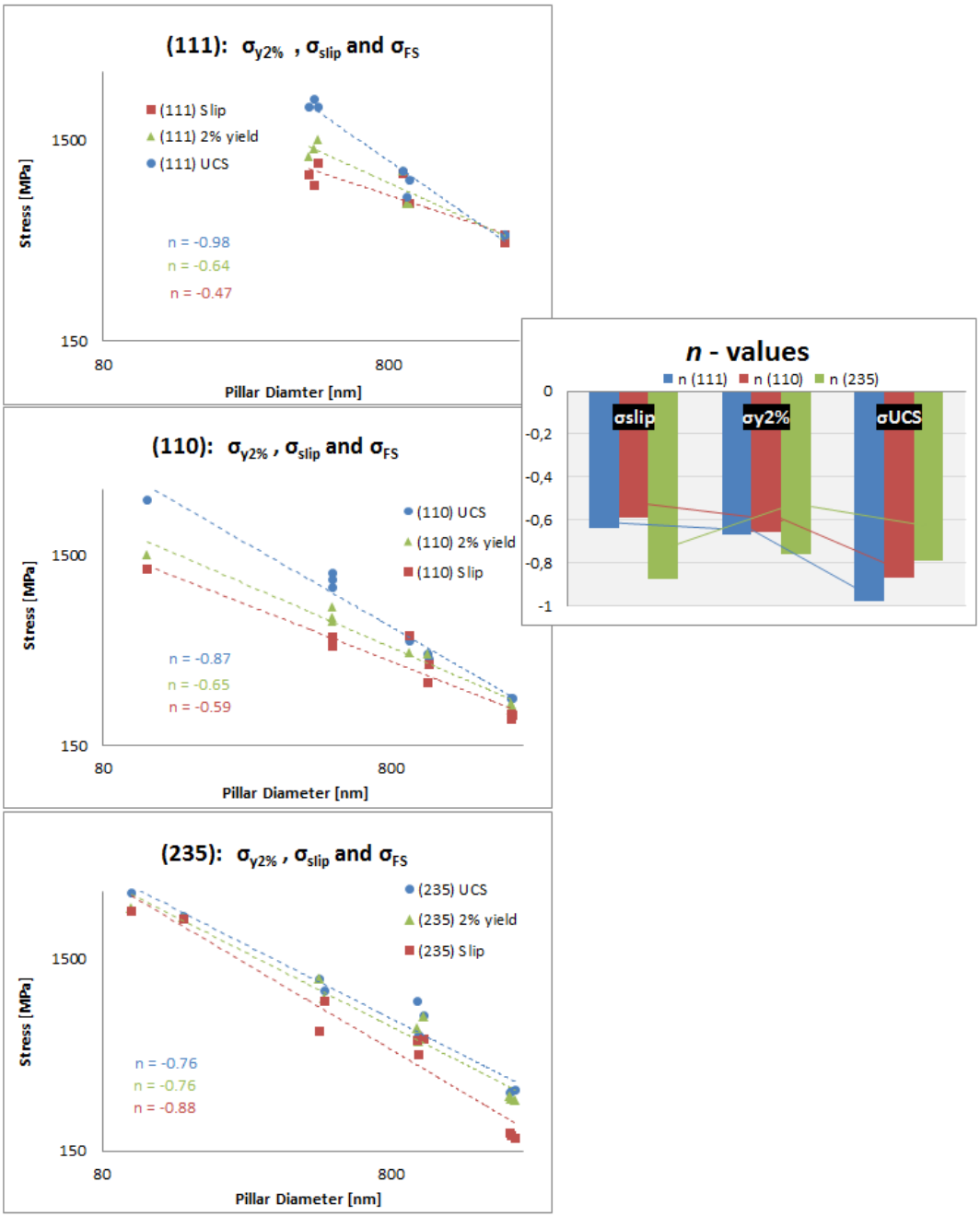

Figure 3.31: n-dependency at σ_{slip}, $\sigma_{y2\%}$ and σ_{UCS}

3.3.5 Discussion

SMALL EQUALS STRONG? Amorphization of a FIB-milled crystalline surface may occur, due to sufficient atom displacement within the collision cascade resulting in the loss of long-range order when the density of point defects reaches a critical value. Thus, FIB-machined compression pillars are not initially dislocation free. This, in addition to the fact that the Fe-sample can not possibly be totally free of impurities, the theoretical ideal strengths are not observed in the present work.
As the pillar size decreases, the critical length scale for which dislocation multiplication can occur, will eventually be larger than the sample itself. Dislocations may thus annihilate at the free surface before conventional dislocation multiplication can occur. Plastic deformation thus requires a continuous supply of fresh dislocations from Frank Read sources, such as by nucleation from the surface, which requires a high stress. This would leave the pillar in a dislocation starved state, hence the widely accepted Dislocation-Starvation model for fcc metals [4]. Atomistic modeling of bcc Fe [6] shows that multiplication does in fact occur in bcc-Fe. In fig.3.33, a simulation of bcc-Fe pillar compression in a (111) loading plane is presented. In a) the pillar diameter is 80Å, while it is 40Å in b) It seems like the disocation loops are activated in the bottom of the pillar. Screw dislocations is highlightned as red. In c, the same pillars are simulated (by Dr. Ersland), with pillar diameter ranging from 50Å to 400Å and the loading plane of (111) orientation. As the pillar is loaded, initial dislocation loops are moving through the pillar, leaving pure screw-dislocations behind, which would continue to stay within the pillar at the source upon loading. The screw-dislocations can be seen as red straight lines pinned out from the loops, and severe dislocation multiplication can be observed in Dr.Erslands figure. Computational simulation is also carried out for the (110) orientation (Author and Dr. Ersland). This can be seen in fig. 3.34. In a) the diameter is 80Å, and two glide planes are avtivated, highligthned by red atoms. In b) the pillar diameter is 40Å, and only one shear plane is activated. The process of initiated dislocation loops are seen in c). As time goes on, the screw-dislocations cross-sect, and hence imped each other, resulting in higher strength. Two shear planes are activated for which shear slip can occur. This result can also be seen in fig. 3.32. These simulations are done with a temperature of 5K. The deformation mechanism in the simulation of (111) and (110) orientation is compared with the corresponding orientations of the present experimental test. Equal mechanism can be observed, at least at the pillar surface. The comparison is seen in fig. 3.32. Still, the deformation mechanism within the pillar of the experimental tests, can not be concluded. The simulations of the interior deformation mechanism can hence give us the answers. Though, the pillar sizes are not comparable, as well as the strain rate. The effect of the very high strain rate in the simulations can hence induce processes which are not comparable with the sub-micro scale experiment. The comparison must therefore be done carefully. Atomistic simulation hence suggest that dislocation interaction causes the increased strength of small pillars.

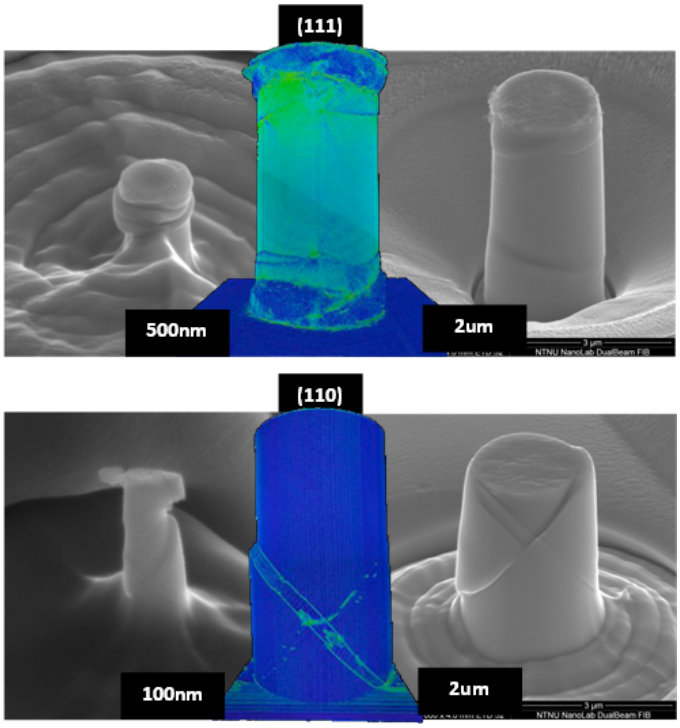

Figure 3.32: Computer simulation (Dr.Ersland) compared with experimental for (111) and (110) orientation. The pillar sizes are in the nano and micro scale for experimental, and at the Ångstrom scale for atomistic.

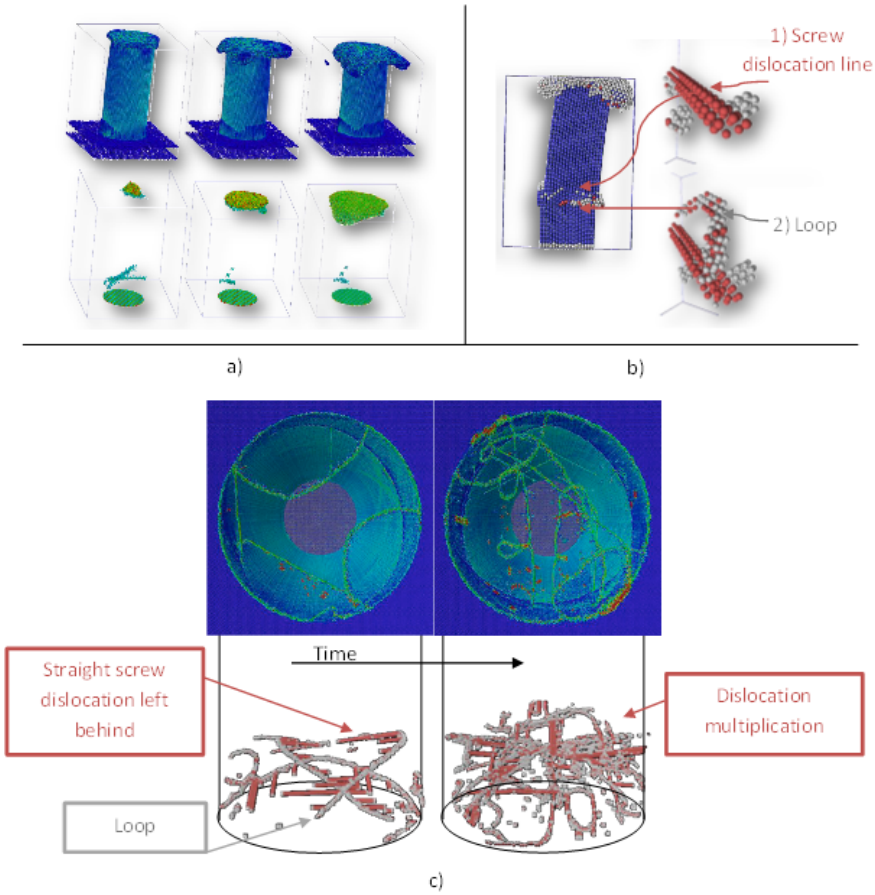

Figure 3.33: Atomistic Modeling bcc-Fe (111) Orientation: a) D=80A, Dislocation loops are activated in the bottom. b) D=40A, Screw dislocation highlight. c) Dr. Ersland MD: Straight screw dislocations are left within the pillar which acts as sessile locks for each other

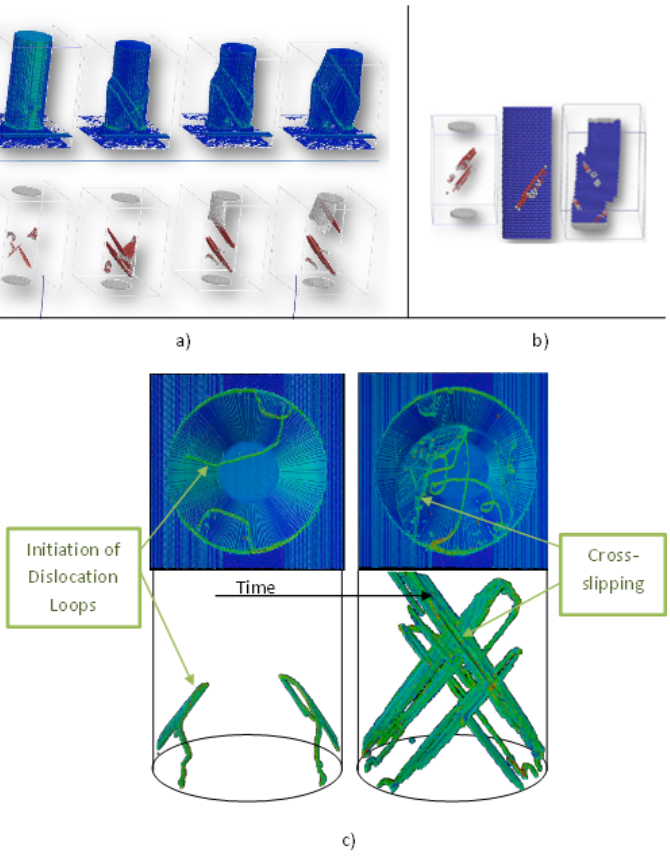

Figure 3.34: Atomistic Modeling BCC-Fe (110) orientation: a) D=80A, two activated shear planes as red highlit within the pillar b) D=40A, One activated shear plane as red atoms c) Dr.Erslands MD: Cross slipping and Screw dislocations within the pillar interior

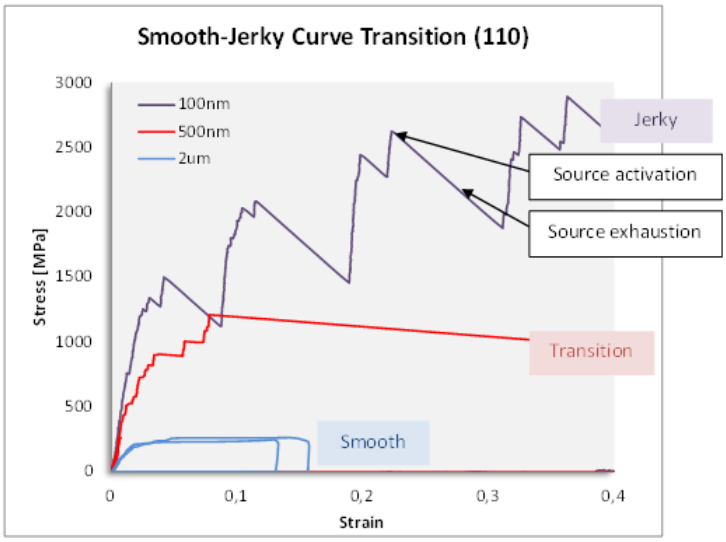

Figure 3.35: Smooth-to-jerky-transition in stress-strain curves due to pillar diameter

The stress-strain curves of the smaller pillars, behave in a jerky manner, due to the characteristic strain-energy exhaustions, which are likely correlated with the initiation of dislocation avalanches, activated in response to the shear stress in the glide plane. The larger pillar curves are smooth and shows significant strain hardening. For the largest pillars (d=2um), the scatter is reduced to almost zero, while the scatter increases as the pillar diameter is reduced. These plastic bursts, separated by elastic portions of deformation, has been attributed to the activation, followed by exhaustion of dislocation sources. As the pillar diameter is increased, and thus the volume of the pillar is increased, the pillar interior can contain more activated sources. As an increased amount of sources are activated, the effect of individual sources can be eliminated, which results in an average, smooth plastic transition, as can bee seen in the stress-strain curves for pillars with diameter equal or larger than 1um. This can bee seen in fig.3.35

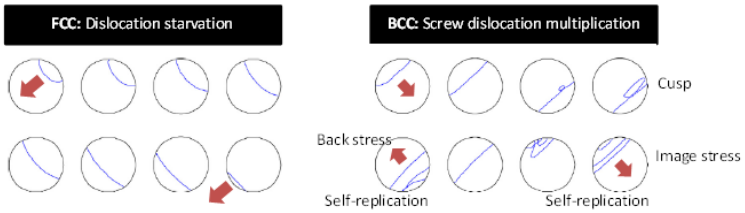

Figure 3.36: Greer et al. : Left: FCC starvation. Right: BCC multiplication

The dislocation multiplication strengthening theory of bcc metals is also supported by Brinckman et al. [**?**], Greer et al. [4], and Cai et al. [7], who has explained the size effect by dislocation-dislocation interaction through DD and MD. Greer et al. completed several bcc-Mo, and fcc-Au pillar experiments at which it was used DD to investigate the difference between fcc and bcc deformation mechanism at small-scale. In bcc metals, edge dislocations move up to 10 times faster than its screw counterpart, escaping the free bcc-pillar surface in an initial stage of loading. Hence, a pure screw line segment is left within the pillar with an increased residence time. A longer residence time enhances the formation of kinks and self-replication. The initial screw dislocation moves through the pillar at the spesific glide plane, before a cusp develops as it moves forward. The cusp then evolves into a dislocation loop which grows larger and eventually leave the pillar. The continued motion of screw dislocations around an internal pinning point sustain this self-replication and thus the plastic deformation process.
3.36In this figure, the fcc edge dislocation loop moves through the pillar cross sectional area, and disappear at the surface. Increased stress then has to be added to accumulate new edge dislocation lines (e.g. Frank Read sources) for further plastic movement. The fcc-pillar is thus starved of dislocations. The starvation model assumes the dislocation would quickly escape from the pillar. The single-arm source model requires dislocation junctions to provide internal pinning points. It is hence suggested that a single nucleation event in abcc pillar can trigger continued dislocation activities, resulting in a large amount of plastic deformation. If this theory holds, bcc micropillar is unlikely to be in a dislocation-starved state.
The theory of Greer et al. conclude that dislocation starvation is the size effect mechanism in fcc metals, while the strengthening in bcc metals are due to the increased residence time of screw dislocations, which, as a consequence, self-replicate and multiplies. The experiments and simulation by Greer et al. is done with pillars of diameter ranging from 300nm to 800nm, which is larger than the smallest pillars in this work. Though, this dislocation-dislocation interaction theory is mainly just a theory suggesting the difference in plastic deformation mechanism for fcc and bcc. It can not explain the transition from smooth stress-strain curves to the strain bursts which occurs in the smaller pillars, neither the origin of the size effect in bcc pillars when the pillar diameter is below 300nm, and where the initial line segment in the Frank-Read source is longer than the sample itself.

The n-values are compared with those from literature. Throughout literature, fcc materials are more pronounced than bcc, when it comes to size effect investigations. Fcc materials such as Au, has been observed to have a more prominent size-effect than bcc metals, such as Mo ([4]). The corresponding n-values for fcc crystals has been measured to be in the range of -0.6 - -1.0 for fcc metals, and about -0.2 - -0.5 for bcc metals. The results from this work, shows that bcc-Fe has n-values for 2% strain, in the range of -0.66 - -0.76, more similar to those for fcc ([4, 9]). It has been, in earlier literature comparing fcc and bcc, suggested that below a critical sample size, the deformation mechanism is similar for both of the crystals, indicating that the dependency of fundamental difference between the structures, collapse. There has also been done studies, where pillar strength where found to depend on the temperature of which they were tested under, T_{test}, correlated to a critical temperature, T_c ([8]). The critical temperature depends on the microstructure and atomic bonding (due to Peierls), so that bcc metals has substantially different T_c-values. Above T_c, the flow strength of the material becomes insensitive to temperature and strain rate. It is called an athermal state. As T_{test} approaches T_c, the mobility of screw and edge dislocations are equal, while below this temperature, screw dislocations are found to be less mobile than edge dislocations. If an amount of energy is added to the bcc screw-dislocation, equal the thermal activation energy for T_c, the mobility of the screw-dislocation increases, and the situation will be equal for that in fcc. In other words, as the pillar diameter is reduced, the effect of the mobility of each screw dislocation becomes less prominent, and both bcc and fcc is controlled by the same mechanism. $T_c = 340\ K$ for Fe (Suzuki 1994). The compression tests were done with a temperature of 22°C, which gives a ratio $T_{test}/T_c = 0.87$. This is a large ratio, or a relatively low critical temperature compared to other bcc metals. The result is compared to that for bcc single slip (235) Nb and W in the work of Schneider (2011), where $T_{test}/T_c = 0{,}85$ for Nb and 0,38 for W and corresponding n-values of -0.42 and -0.16 respectively. The values for Schneider et al. are measured at the point of 2.5% strain, while the values of this work are measured at 2% strain. T_c for Nb is quite similar to that for Fe, while there is a significant difference in the power-law exponent, -0.42 and -0.76 in the (235) orientation respectively. Hence, Fe is found to have an increased size effect, compared to Nb (and W). It is also to be mentioned that the smallest pillars in Schneiders work are 200nm, while for this work, they are 100nm. Hence, the trend of the size effect will result in an increased strength for this works pillars, which also affects the power law exponent. In the figure below, T_{test}/T_c is plotted against the power law exponent for the three different orientations of Fe, and compared to the results from Schneider et al. The orientation (235) for Nb and W is seen as black square markers. The plot shows that Nb and Fe has the same T-ratio, but differs in the power law exponent. The T-ratio, which is characteristic for the mobility of screw dislocations in bcc metals, is suggested to be the controlling factor regarding the different deformation mechanism in bcc compared to fcc. Fe exhibits an increased size effect than both of the other two bcc metals. From this plot, it is expected that Nb and Fe would have quite similar deformation behavior at small-scale compression, while T_C is high and n is low for W, the latter will have a reduced size effect. As T_{test}/T_c ratio decrease, the relative length of the screw dislocation segments increase. Hence, the dislocation mechanism in W is dominated by screw dislocations, where cross-slipping will occur. Because both Nb and Fe behaves similar to those of fcc metals due to stress-strain curves, and W do not, it is suggested that the deformation mechanism at high bcc T-ratios is

controlled by a thermal process as well as a athermal process. T_C is relatively low for both of these bcc metals, resulting in a relative reduced pure screw-dislocation segment, reducing the ability to cross-slip, which result in activation of specific defined glide planes.
It is indicated in the plot, separated by the darker triangle, which of the two processes, thermal or athermal, is expected to dominate the deformation process. Points within the dark triangle is more likely to be dominated by an athermal process, e.g. the mobility of screw dislocations are negligible. Hence, dislocation motion is activated by initial nucleation, as for fcc metals. The thermal process is likely to dominate in the lighter triangle, where the mobility of screw dislocations is the key factor. This will result in dislocation multiplication and forest hardening. If the testing procedure had been carried out at different test temperatures, it would be possible to extrapolate fitting curves between the points. It would then be interesting to see what the n-value of the corresponding $T_{test}/T_c = 1.0$ would be. This value would correspond to the point of where the deformation mechanism is fully dominated by athermal processes.

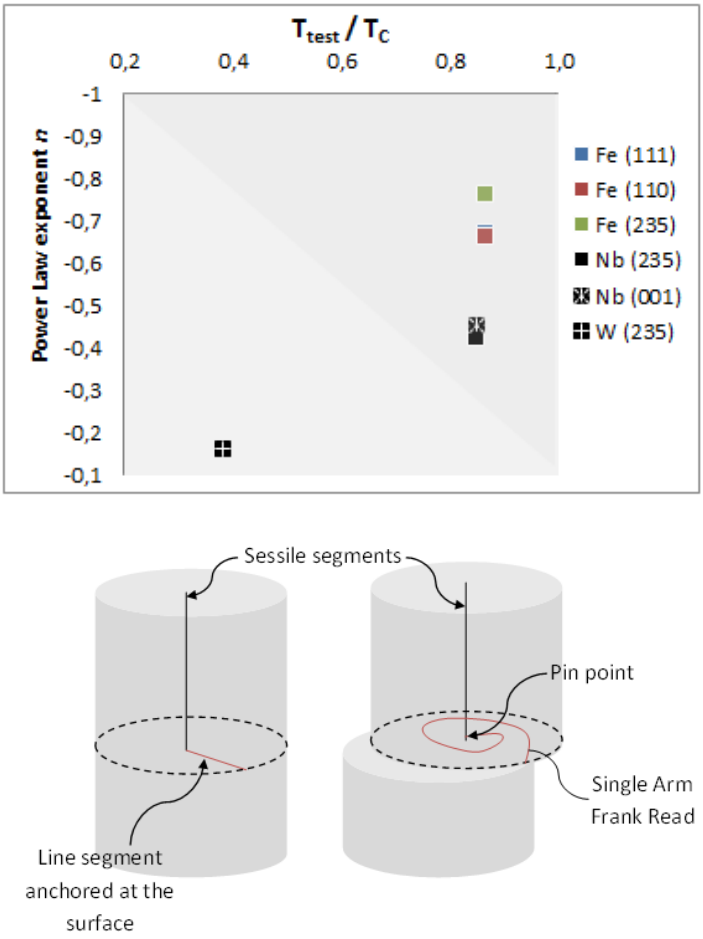

Figure 3.37: Single-arm Frank-Read dislocations nucleated by surface assisted kinks

If the observable size effect in Fe is due to a combination of a thermal and athermal processes, it is suggested that the hardening is not dominated by screw-dislocation immobility at high test temperatures (high T_{test}/T_c ratios). Because bcc-metals with high critical temperature, combined with a low n-value, also has shown a significant size effect at small pillar sizes (i.e. W), the strengthening of the smallest sizes must be caused by another factor than the athermal process. From [**?**] (2012), this can be explained by the phenomenon of kink nucleation at the pillar surface. The mobility of kinks on screw segments acts as the limiting mechanism due to dislocation motion in bcc. The nucleation and motion of kinks is thermally activated and, therefore, primarily controlled by the energy barriers corresponding to transitions between states. As the pillar area/volume ratio increase, the mobility for screw dislocation increase, approaching that for its edge counterpart. By assistance from surface kink nucleation, the initial screw dislocation can overcome the Peierls potential, and thereby approach a similar state such as the athermal state. Hence, the dislocation mechanism is similar to that for fcc and an athermal driven bcc deformation.

For the single slip orientation (235), the results has been compared to those for Schneider et al. (2009,2010 and 2011) [9]. In fig.3.38, post-compression pictures of the authors Fe pillars are shown in a) and Schneider et al. (235) Mo pillars are shown in b). The pillar diameter is approxmetly equal (respectively 2-3um and 400-500nm). Slip traces on the pillar surface can be observed, confirming single slip mechanism. Single slip lines at distinct slip planes indicates a minimal amount of cross-slipping. The corresponding n-values indicates that the behavior of size effect in single slip pillars are more sensitive for size-dependency than those for multi-slip (referring to (111) and (110) orientations). It has to be mentioned that results from (111) orientation with the smallest pillars are excluded, and thus the resulting n-value is reduced. The n-value of (235) is -0.76 compared to -0.66 for (110). In the work done by Schenider et al. (2011) on W and Nb, the power law exponent did not vary significantly due to different orientations ((235) and (001)). It was therefore concluded that the size effect is independent of orientation. In this work, by comparing the power law exponent of (110) and (235), it differs by an amount of -0.1 (-0.66 and -0.76 respectively). If this amount of -0.1 is enough to suggest that the orientation does, in fact, affect the size effect, is though not clear. To shed a light on this result, earlier experiments on bcc Mo pillars, found the power law exponent to vary between -0.22 and -0.36 for (001) and (235) respectively. This is also an increased amount of about -0.1. [**?**]

The theoretical ideal shear strength for bcc-Fe is calculated by D.M. Clatterburck et al. (2003) to be 7.8 GPa for (110)$\langle$111$\rangle$ systems. If this is compared to the stress-strain curves in fig.**??**, the smallest pillars are not in the range of these values. In the stress-strain curves of (111) pillars, there are not any pillar results from d = 100nm. The smallest ones are 500nm, which slips at an axial yield strength of 1 GPa, while the small pillar in (110) orientation slips at 1.25 GPa. This corresponds to a shear strength of 0.38 GPa and 0.245 GPa respectively. For (235) the highest shear strength for the smallest pillar is 1.25 GPa. The small pillar in (110) is thus reaching only 3.1% of its theoretical shear strength. Greer and Brinckman had n-value at -0.47 for bcc-Mo.

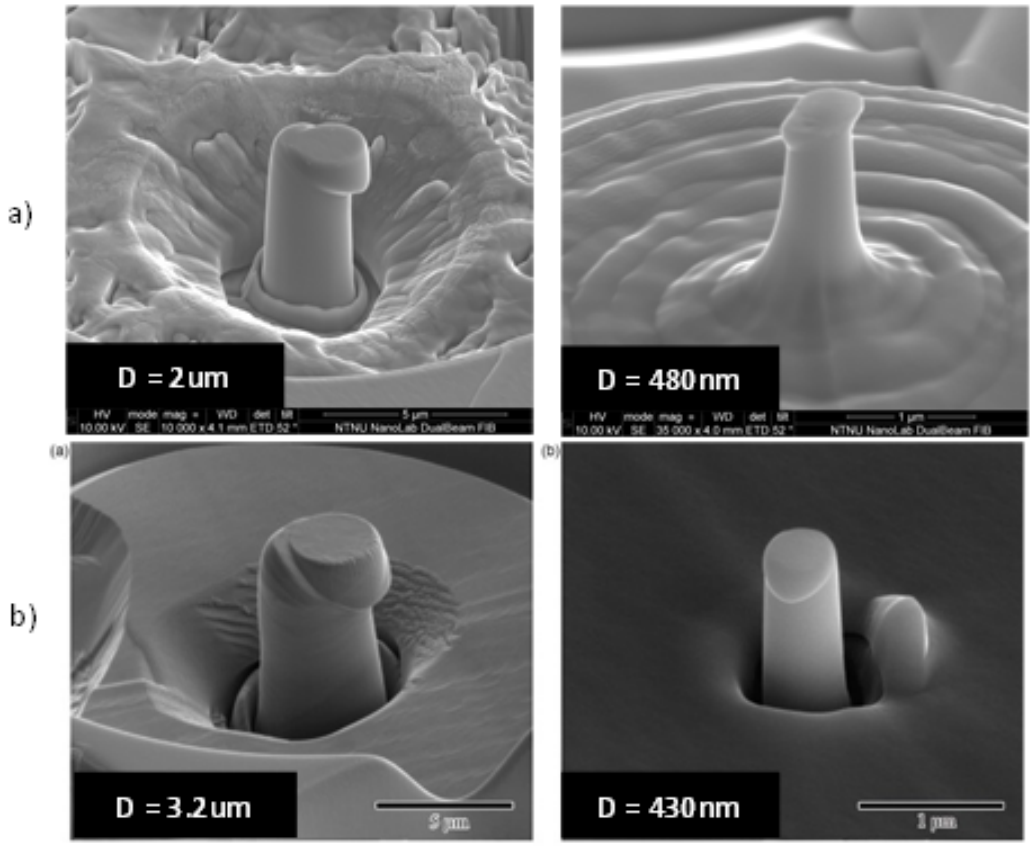

Figure 3.38: (235) bcc pillars: a) Authors compression results b) Schneider et al. post-compression image [235] Mo pillars

3.4 Comparing F70, bcc-Fe and EU Nb5

In bcc-Fe, a size effect is clearly present. For F70 steel, the size effect is not prominent until the pillar diameter is reduced to about 200nm. For the EU MultiHy steel, there are not enough data points to conclude any size effect. From the stress-strain curves seen in fig. , it can be speculated if there is a trend between the 1μm pillar and 500nm pillar, as the curves for the latter pillar situated above the ones of 1μm. To conclude if this is a trend, like for bcc-Fe, one more smaller pillar size should be investigated.

The comparing Post-Compression results from the bcc ferrite phase of MultiHy steel, single slip orientation (5 2 11) Nb5, and single slip orientation (2 3 5) of Fe, is presented in fig. 3.39. The pillar size of 1μm is marked as green curves, 500nm pillars are marked as red curves, while other pillar sizes are plotted as stapled lines. Two scale bars are presented, to be able to investigate closer the behavior at which slip occurs, while the corresponding graphs below, shows the amount of strain hardening. One can observe that there is a quite similar behavior, when the slip yield stress is concerned. Because MultiHy steel is an alloying steel, whereby contents of Nb should increase the strength by fine carbide precipitation or grain refinement, one should expect higher strength compared to bcc-Fe. The two different single slip systems might have a vastly different Schmid factors, hence, this effects the shear strength at the specific grain orientation. It can also be observed that the 500nm curves of both materials exerts a jerky deformation mechanism of energy exhaustion, while the corresponding 1um curves exhibits a smoother elastic-plastic transition deformation. It is clearly evident that that the toughness of Nb5 is more pronounced than for Fe. In the larger scale graphs below, the ductility of Nb5 can be seen as the large amount of strain hardening. This is caused by Nb. The trend of size effect is clearly prominent in the Fe results. The corresponding trend for Nb5 is very similar, but because there are no 200nm pillars or 2um pillars tested for the latter material, if the observed trend is caused by random scatter, or if it would follow that for Fe. The results from all three materials are compared, i.e. (111) Fe, F70 5 sec MA-phase and EU Nb5 martensite phase, at which the stress-strain curves are presented in fig. 3.40. The green curves corresponds to 1um pillars, while red curves corresponds to 500nm pillars. Other curve colors corresponds to other sizes, and are plotted just to see the whole picture of size effect. The dominating deformation mechanism in F70 MA-phase, was found to be uniformly axial flat, (although some pillars also had shear deformation). This mechanism is quite similar to that for (111) orientation of Fe. It is though interesting to see the difference in slip yield strength, which is much higher for F70. One can also observe the difference in the stress-strian curves for the smallest pillars. Fe exhibit jerky curves with a large amount of energy exhaustion, like stair cases, while there are a more smooth transition from elastic to plastic flow even at the smallest pillars for F70. This indicate that the deformation mechanism is very different at small samle sizes for a pure bcc metal, compared to an alloying steel. This is probably caused by the very distinct shear planes of Fe compared to the complex and chaotic slip planes of martensite/bct/hcp and pre-induces strain gradients. The martensite pillars of Nb5 are also compared to F70. In this case, shear slip was activated in three of four cases, although also in this case, there are two quite similar curve behavior, like for F70. The slip yield strength is lower for Nb5 compared to F70.

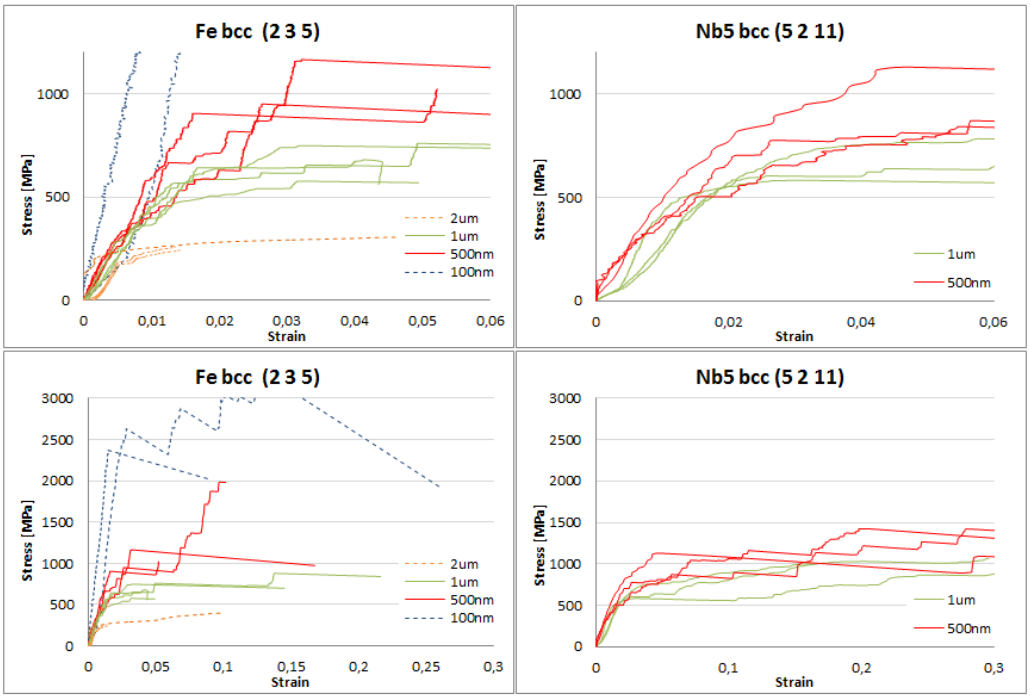

Figure 3.39: Comparing Nb (5 2 11) with Fe (2 3 5) single slip orientation of varying pillar diameter

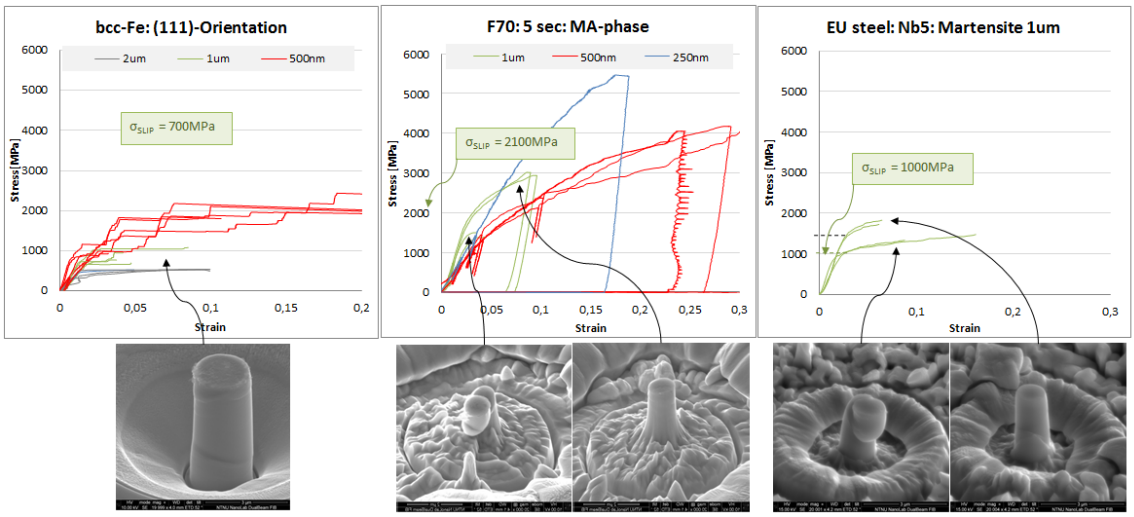

Figure 3.40: Comparing deformation mechanism and slip yield stress for Fe (111), F70 5sec and EU Nb5 martensite phase

Chapter 4

Conclusion

When comparing flow stress values for the three different orientations in bcc-Fe, the (111) orientation exhibit higher stresses relative to both (235) and (110) Fe pillars of comparable sizes. Regardless, for all three orientations, the flow stress is consistently larger with decreasing pillar diameter, indicating a size effect.
For all three orientations, the strength is shown to be inversely related to the pillar diameter, with a best fit of $\tau_{CRSS} \propto D^n$, where power law exponent, n, corresponding to orientation (111), (110) and (235) is calculated to be -0.67, -0.66 and -0.76 respectively. These are measured at 2% strain. This indicate a strong size dependence, for both multiple slip systems and single slip systems, hence, the deformation process is not strongly dependent on the crystal orientation. As expected, the smallest (235) pillars shows slip lines in one exclusively slip direction, hence, the cause of size effect can not be directly connected to dislocation-dislocation interaction. It is argued that the thermal activation energy (Peierls) is the dominating deformation factor.

Pure metals with long-range order of a homogeneous lattice structure, and without strain gradients present, is suggested to have a more pronounced size effect than for alloying metals with varying microstructure and induced strain gradients. It is also suggested that plastic deformation of pure bcc metals are dominated by its athermal temperature, which corresponds to the mobility of screw dislocations. At T_{test}/T_C ratios near 1.0, the mobility of screw dislocations approaches that for edge dislocations, which means that both dislocation types escape to the free surface quickly after initiation, leaving the material interior in a starved state. Further deformation is then dominated by surface nucleated kinks which initiates single-arm Frank-Read sources. The surface assisted kinks can also enhance the mobility of screw dislocations, so that they approach the mobility of edge dislocations. It is suggested that this happens at lower T_{test}/T_C ratios, where the deformation is dominated by the immobility of screw dislocations. The increased residence time results in screw dislocation self-replication. Cusps are formed as the dislocation moves, initiating a new screw dislocation which act as a sessile lock. Thermal energy is introduced (as applied stress), which can then move the screw dislocations further before it again self-replicate.

In contradiction to other bcc metals, as single crystal Mo, W, Ta and Nb, the smallest pil-

lar diameter tested in this work, is 100nm, which is less than for that in earlier work (where the smallest pillar diameter is 200nm [10]). There is not any available official investigations done on Fe, so this work is compared with other bcc metals. The size dependence of Fe is in the range of those for fcc metals (which is measured to be in the range from -0.6 to -1.0). For other bcc metals, the range varies between -0.12 - -0.6. The hardening is due to a source limiting behavior at small scales, where exhaustion of the weakest source leads to an increase in stress associated with the activation of less favorable dislocation sources.
Based on these results for bcc-Fe, it is proposed that the size effect is dominated by the mobility of screw dislocations, due to a high T_{test} / T_C ratio. Decreasing T_C combined with reduced pillar diameter, reduce the effect of screw dislocations and cross-slip, hence the strengthening mechanism approaches that for fcc metals (but not exactly the same).

The overall conclusion regarding size effect, is that it is dominated by two factors:

- Temperature
- Microstructure

Regarding F70 steel, the experimental conclusion indicate an increased strength of the 5 sec sample, when the MA-Phase is concerned. The matrix exhibit higher toughness, but lower strength, compared to the grain boundary, in both samples. F70 is an alloying steel, with a high degree of complexity within the microstructure. The size effect is not observable until a critical pillar size is reached, about 250nm. This indicate that the size effect is dominated by the microstructure, strain gradients and GNDs.
The post-compression result from the EU-project dual phase steel, indicates that an alloying amount of 0.05wt% Nb is the superior steel. The ferrite phase of single slip orientation (5 2 11) is compared in both samples. The mechanical properties are increased as Nb is added to the sample. This is also expected, as Nb retard the grain growth, and induce fine precipitation hardening within the ferrite matrix, enhancing toughness and strength. The martensite phase of Nb5 exhibit a significantly higher yield strength, but a lower ductility. It can not be concluded that a size effect is observed in the dual phase steel, because only two sample sizes are investigated, 1um and 500nm. The trend is though very similar for single slip bcc-Nb5 to single slip bcc-Fe. It can not be concluded if this is caused by random scatter or that it is an actual trend.
The Dual Phase steel has one sample containing 0.05wt% Nb and one without Nb. From the compression testing, it can be concluded that alloying with Niobium results in superior mechanical properties, as stress-strain curves shows an overall higher strength, both in increased yield strength and increased strain hardening.

4.1 Further Improvements

- **In situ compression**
  Nanocompression experiments should also be conducted in situ within a transmission electron microscope (TEM) for real time imaging, so that slip lines, and dislocation motion can be observed.

- **Investigation of FIB damage during pillar fabrication**
  Is the size effect caused by Ga+ implementations within the pillars? EBSD og EDX measurements could be done on cross sections of trenches, so that the effect of FIB damage at 9nA, 0.26nA and 26pA and 30keV, could be investigated. The FIB current should be varied, to investigate if there is any relationship, so that the damage can be calculated and reduced. Gas assisted removal injection needles can be used to eliminate redeposition of Ga ions. Also reduce ion beam current at last steps of fabrication to reduce damage.

- **Dual Phase Steel Size Effect**
  More pillar sizes should be made for MultiHy steel which phase components are martensite and ferrite, if the size effect in this material should be of interest to determine. The two different phases could then be compared to the ferrite in the pure iron sample, and the martensite could be compared with the martensitic phases of the arctic F70 steel.

- **Atomistic simulation**
  Simulation of bcc-Fe should be carried out with a taper angle of about 3 degrees and a pillar diameter of 1000Å (100nm). Single slip orientation as well as multislip orientation should be conducted. Comparing this with the experimental results for equal orientations will maybe reveal the real plastic behavior and the cause of size effects at small pillars. The link between atomistic and micro scale will then be made stronger.

Chapter 5

Appendix 1: Pillar Fabrication

5.1 Pillar Fabrication F70 steel

Table 5.1: F70: 10 sec sample; Grain Boundary and Interior Grain

d_{size} $[um]$	$Step$	d_{outer} $[\mu m]$	d_{inner} $[\mu m]$	$BeamCurrent$ $[nA]$	z $[\mu m]$	$Dwell$ $[ms]$	MD IO/OI	Passes
0.250	1	22	7	9	2	0.001	IO	-
	2	8	3	0.26	0.18	1	OI	1
	3	3.5	0.30	0.026	0.06	1	OI	1
0.5	1	22	7	9	2	0.001	IO	-
	2	12	3	0.26	0.18	1	OI	1
	3	3.5	0.5	0.090	0.10	1	OI	1
1	1	22	7	9	2	0.001	IO	-
	2	8	1.2	0.44	0.23	1	OI	1

Table 5.2: F70: 5 sec sample; Grain Boundary and Interior Grain

d_{size} $[um]$	$Step$	d_{outer} $[\mu m]$	d_{inner} $[\mu m]$	$BeamCurrent$ $[nA]$	z $[\mu m]$	$Dwell$ $[ms]$	MD IO/OI	Passes
0.250	1	22	7	9	2	0.001	IO	-
	2	7	3	0.26	0.18	1	OI	1
	3	3.5	0.30	0.026	0.06	1	OI	1
0.5	1	22	7	9	2	0.001	IO	-
	2	12	3	0.26	0.18	1	OI	1
	3	3.5	0.5	0.090	0.10	1	OI	1
1	1	22	7	9	2	0.001	IO	-
	2	12	5	0.90	0.28	1	OI	1
	3	6	1	0.44	0.23	1	OI	1

5.2 Pillar Fabrication Pure Iron

The fabrication in iron was done with four different pillar sizes; 100nm, 500nm, 1m̆ and 2m̆. In addition, three different orientations were selected to be analyzed; (111), (110) and the single-slip system of (235). Because of significant difference in tunneling effects due to different grain orientations, the procedure of pillar fabrication had to be adapted to each of the orientations.

Table 5.3: Iron; Phase/Orientation: Ferrite/(111)

d_{size} $[um]$	$Step$	d_{outer} $[\mu m]$	d_{inner} $[\mu m]$	$BeamCurrent$ $[nA]$	z $[\mu m]$	$Dwell$ $[ms]$	MD IO/OI	Passes
0.1	1	22	7	9	2	0.001	IO	-
	2	8	1.8	0.26	0.18	1	OI	1
	3	2	0.1	0.026	0.05	1	OI	1
0.5	1	22	7	9	2	0.001	IO	-
	2	7.5	0.5	0.26	0.18	1	OI	1
1	1	22	7	9	2	0.001	IO	-
	2	10	1.1	0.26	0.18	1	OI	2
2	1	22	7	20	2	0.001	IO	-
	2	11	2.2	0.26	0.18	1	OI	4

Table 5.4: Iron; Phase/Orientation: Ferrite/(110)

d_{size} $[um]$	$Step$	d_{outer} $[\mu m]$	d_{inner} $[\mu m]$	$BeamCurrent$ $[nA]$	z $[\mu m]$	$Dwell$ $[ms]$	MD IO/OI	Passes
0.1	1	22	7	9	2	0.001	IO	-
	2	8	1.8	0.26	0.18	1	OI	1
	3	2	0.15	0.026	0.05	1	OI	1
0.5	1	22	7	9	2	0.001	IO	-
	2	7	0.55	0.090	0.10	1	OI	1
1	1	22	7	9	2	0.001	IO	-
	2	9	1.2	0.44	0.23	1	OI	1
2	1	22	7	20	2	0.001	IO	-
	2	7	2.2	0.26	0.18	1	OI	2

Table 5.5: Iron; Phase/Orientation: Ferrite/(235)

d_{size} $[um]$	$Step$	d_{outer} $[\mu m]$	d_{inner} $[\mu m]$	$BeamCurrent$ $[nA]$	z $[\mu m]$	$Dwell$ $[ms]$	MD IO/OI	Passes
0.1	1	22	7	9	2	0.001	IO	-
	2	8	2	0.26	0.18	1	OI	1
	3	2.2	0.15	0.026	0.06	1	OI	1
0.5	1	22	7	9	2	0.001	IO	-
	2	8	0.55	0.26	0.18	1	OI	1
1	1	22	7	9	2	0.001	IO	-
	2	8	1.2	0.90	0.28	1	OI	1
2	1	22	7	9	2	0.001	IO	-
	2	10	2.3	0.90	0.28	1	OI	2

5.3 Pillar Fabrication EU-steel

Pillars fabricated in the dual phase steel is located within the phase of martensite and ferrite. The grain orientation within the ferrite is (5 2 11) for all the pillars. This is a single-slip system. Both in ferrite and martensite, the same pillar fabrication procedure was used, resulting in the following pillar geometries:

1. Diameter = $1\mu m$
2. Hight = $2.5\mu m$
3. Ratio $h/d = 2.5$

Table 5.6: EU-steel; Phase/Orientation: Martensite and Ferrite/(5 2 11)

Step	d_{outer} $[\mu m]$	d_{inner} $[\mu m]$	*BeamCurrent* $[nA]$	z $[\mu m]$	*Dwell* $[ms]$	*MD* *IO/OI*
1	22	7	9	2	0.001	IO
2	8	1.2	0.26	0.18	1	OI
3	6	1.2	0.09	0.10	1	OI

Chapter 6

Appendix 2: bcc-Fe: Pillar Deformation

6.1 Pure Iron: Pillar deformation

6.1.1 (110) Orientation

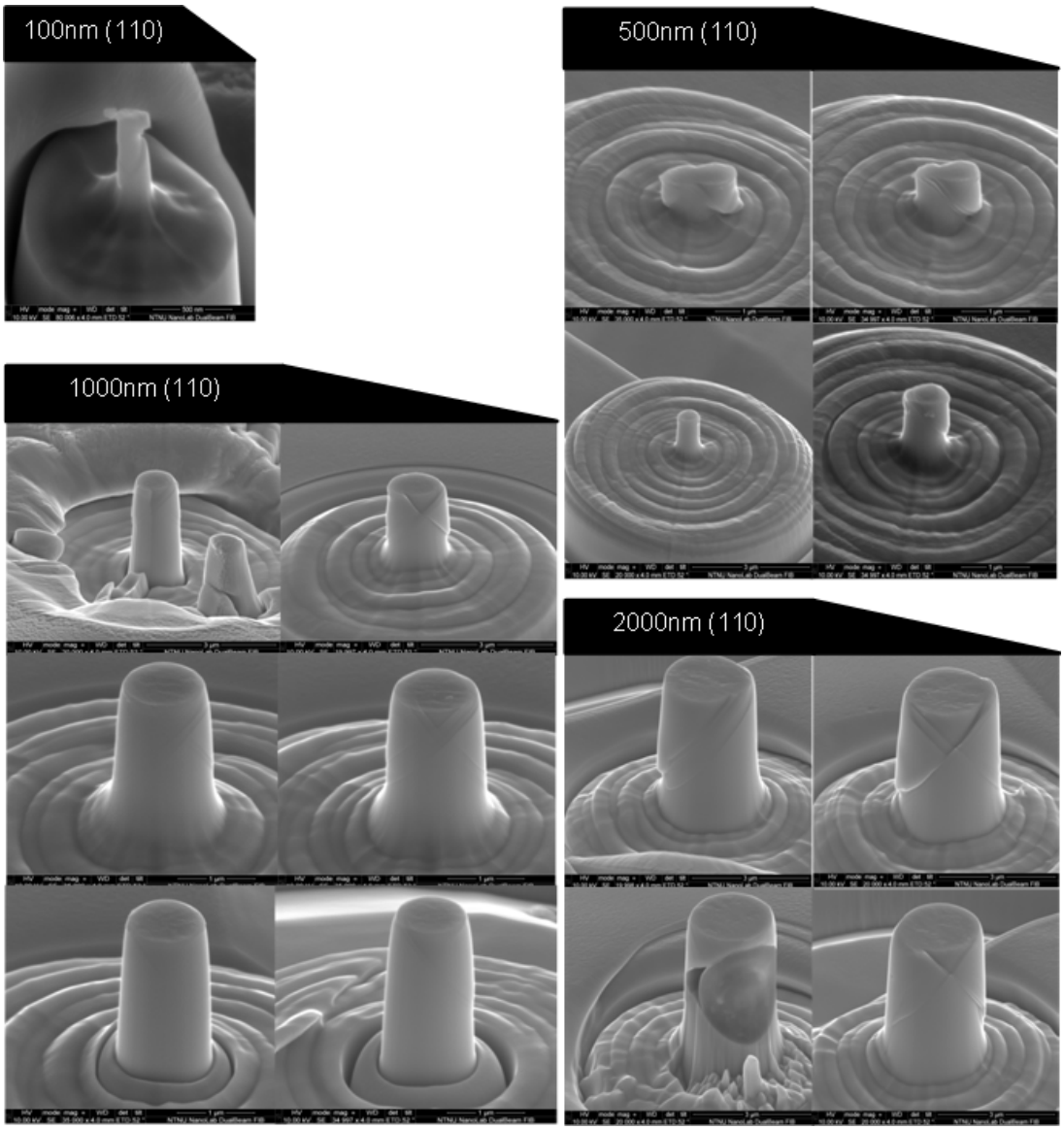

6.1.2 (111) Orientation

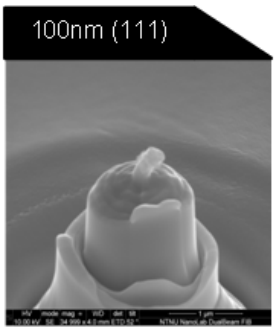

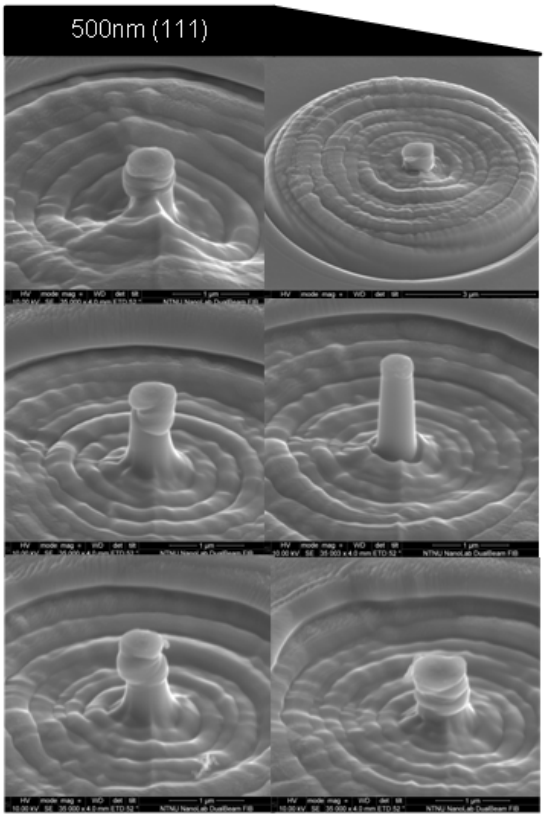

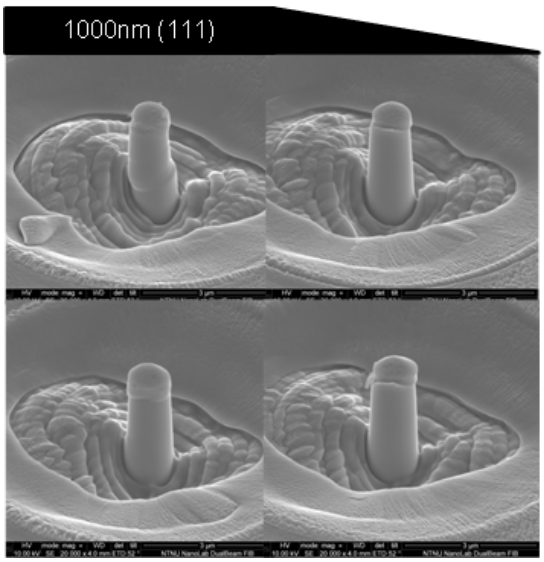

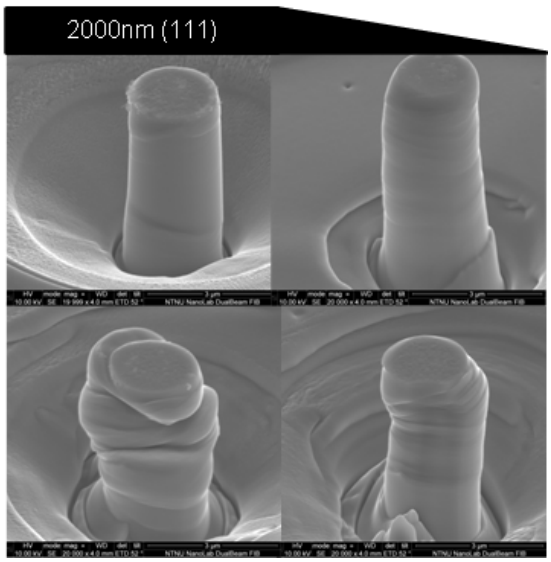

6.1.3 (235) Single Slip Orientation

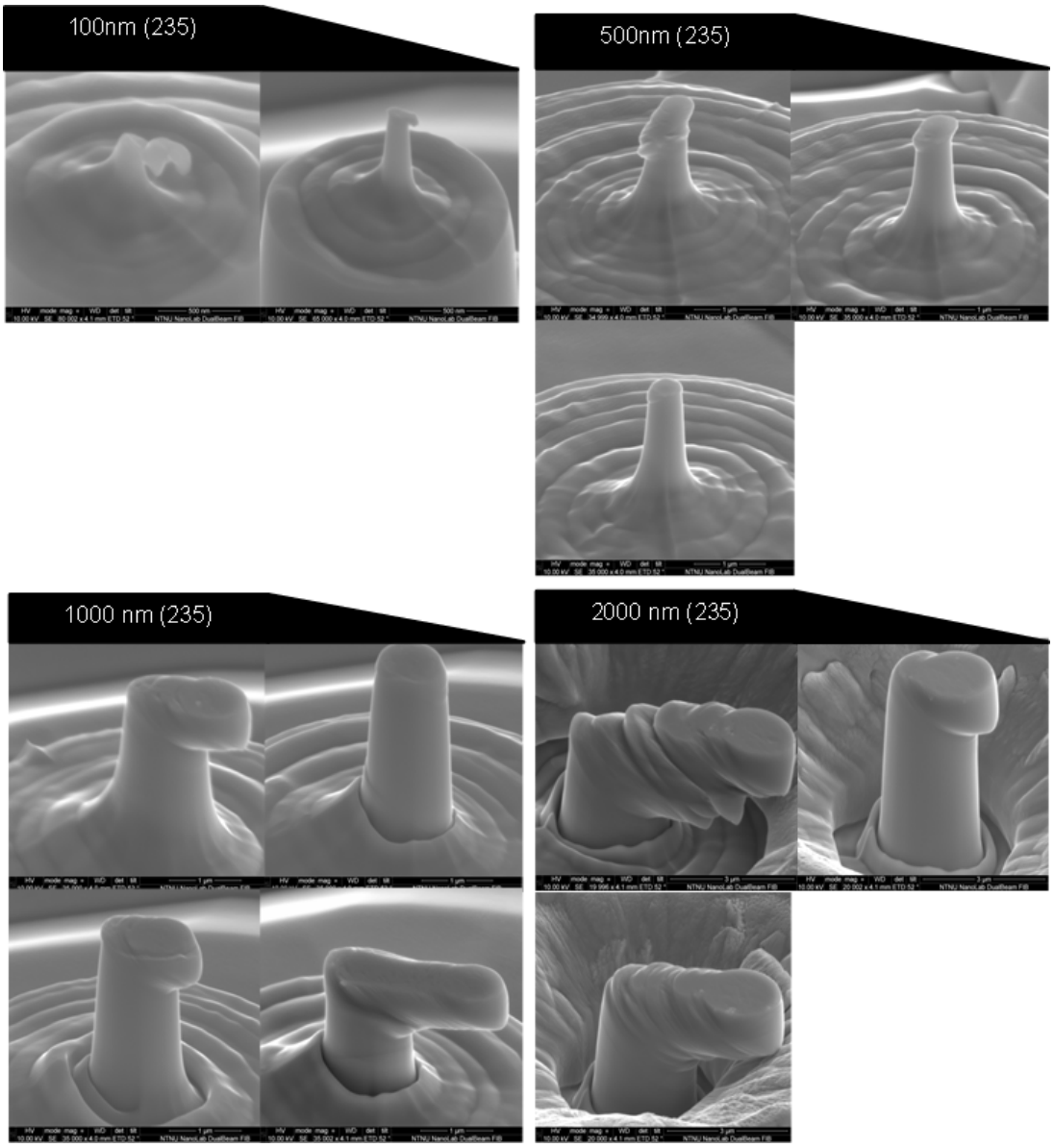

Chapter 7

Appendix 3: F70: Pillar Deformation

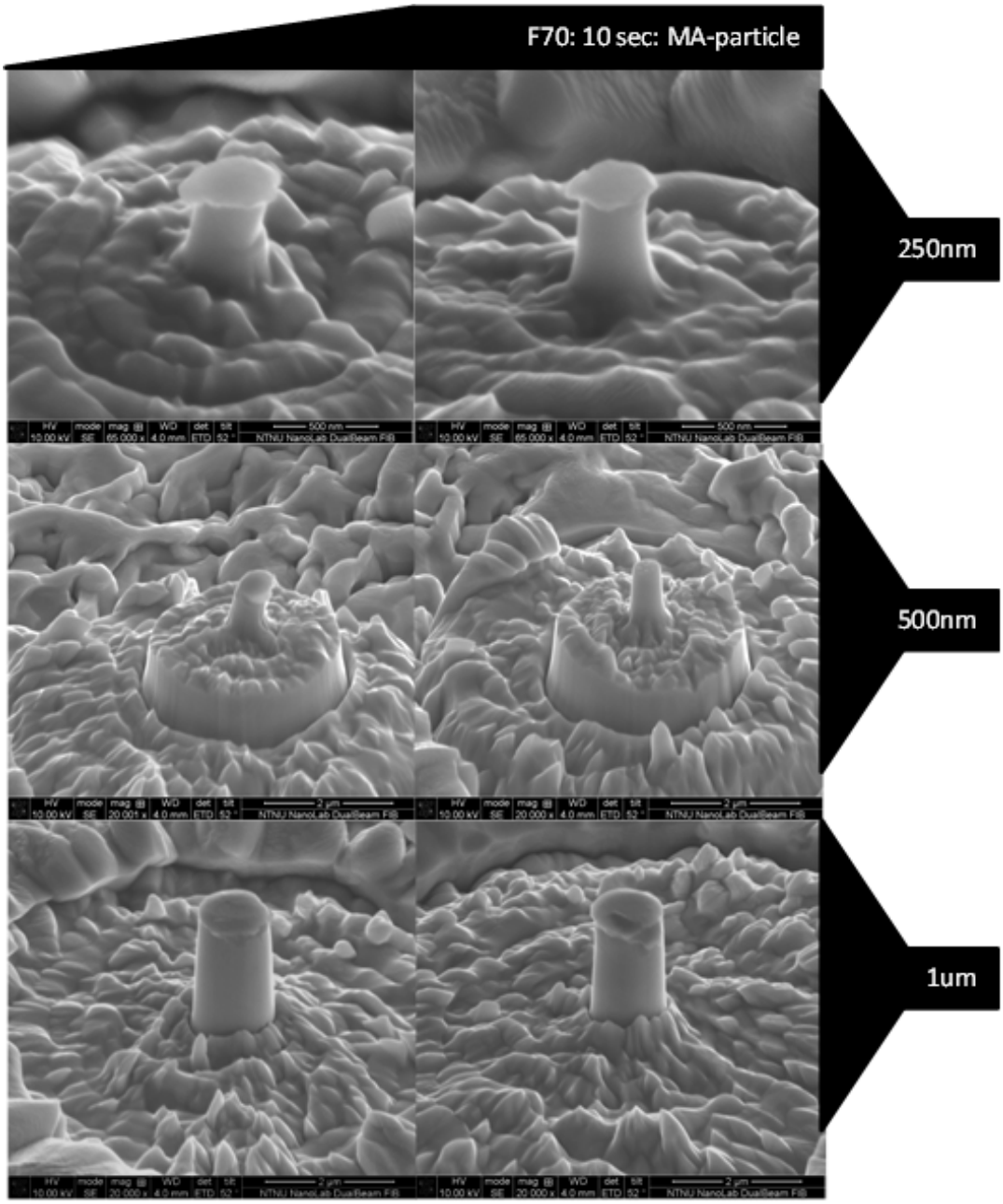

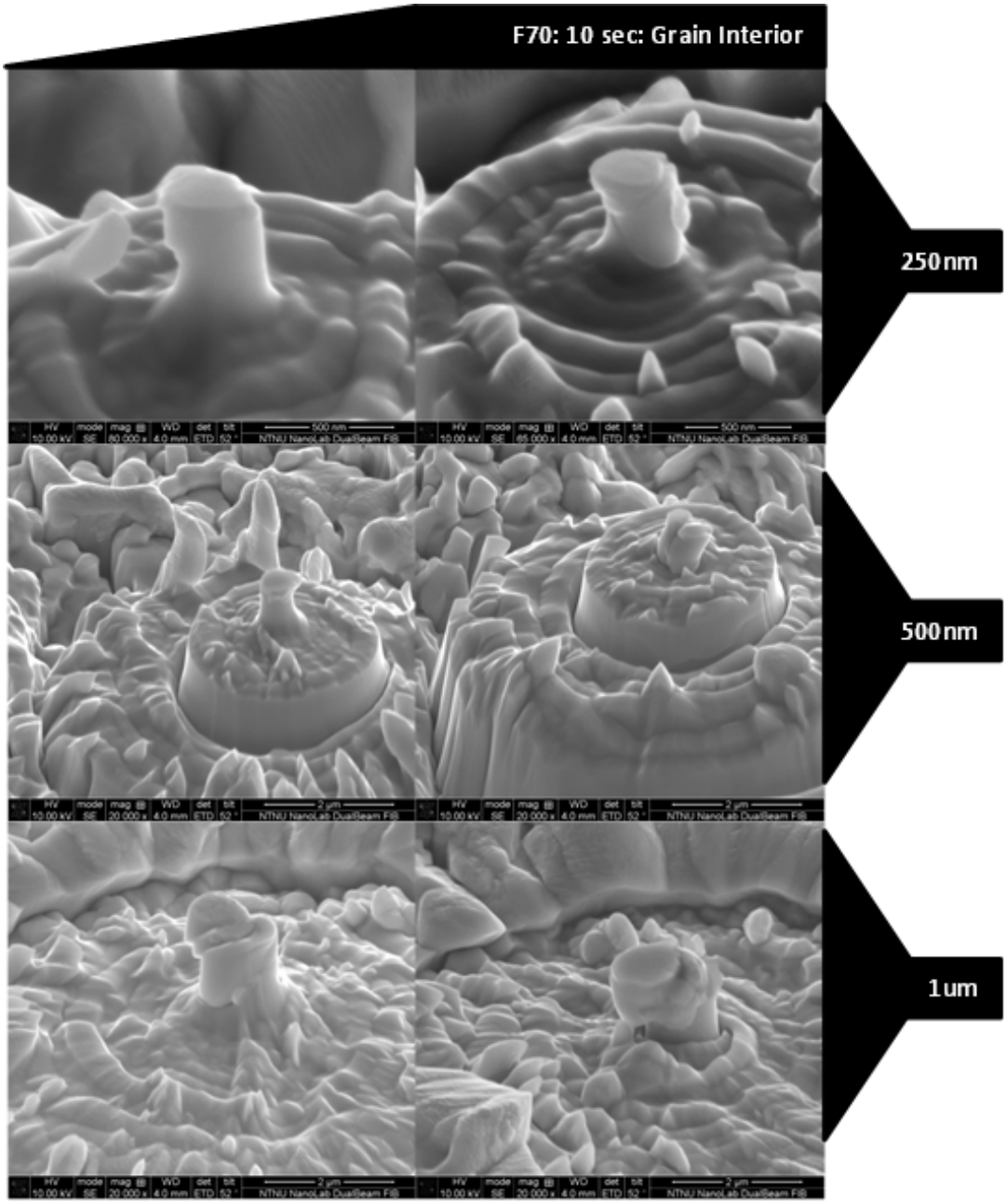
F70: 10 sec: Grain Interior
250nm
500nm
1um

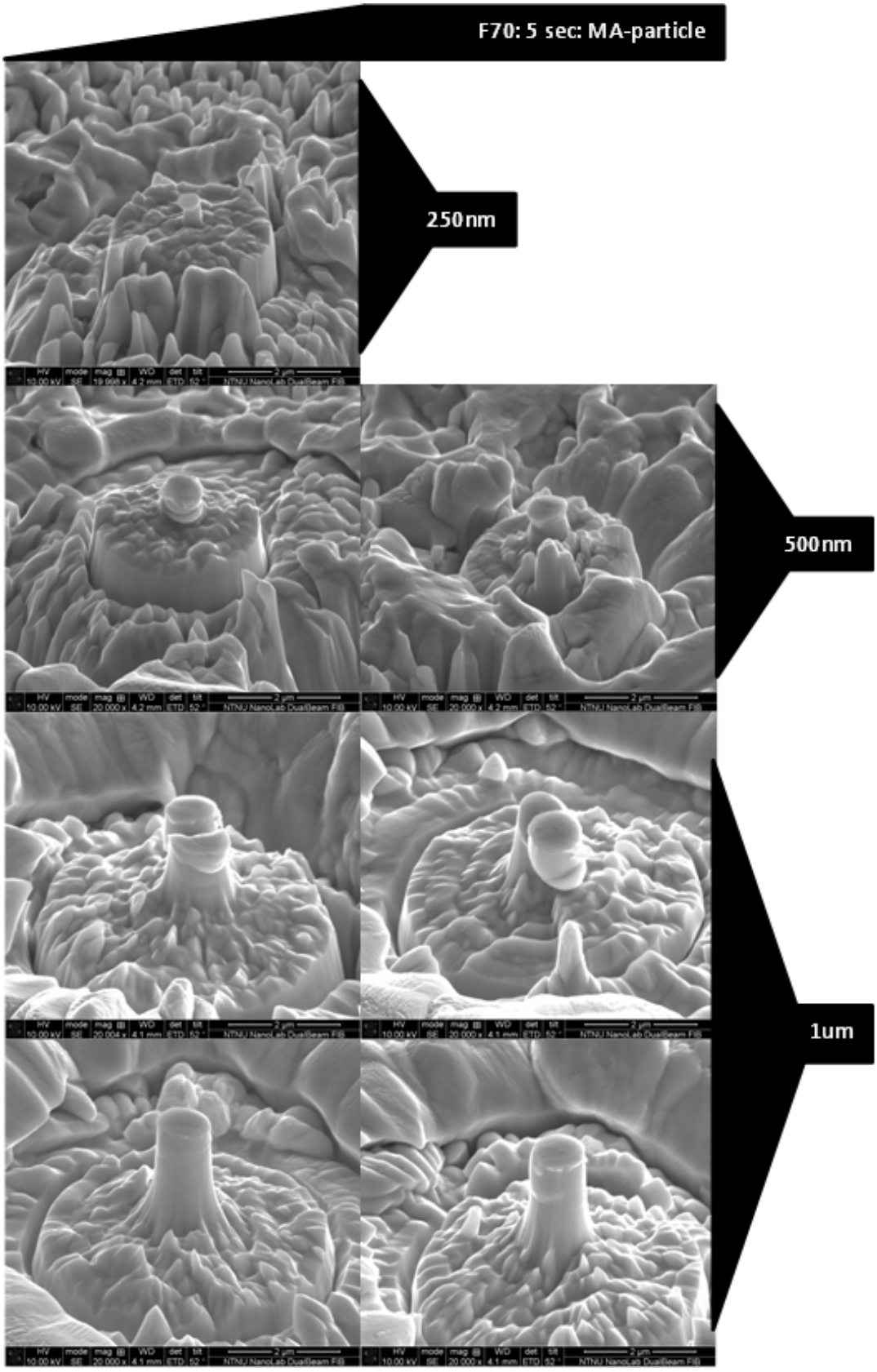
F70: 5 sec: MA-particle
250nm
500nm
1um

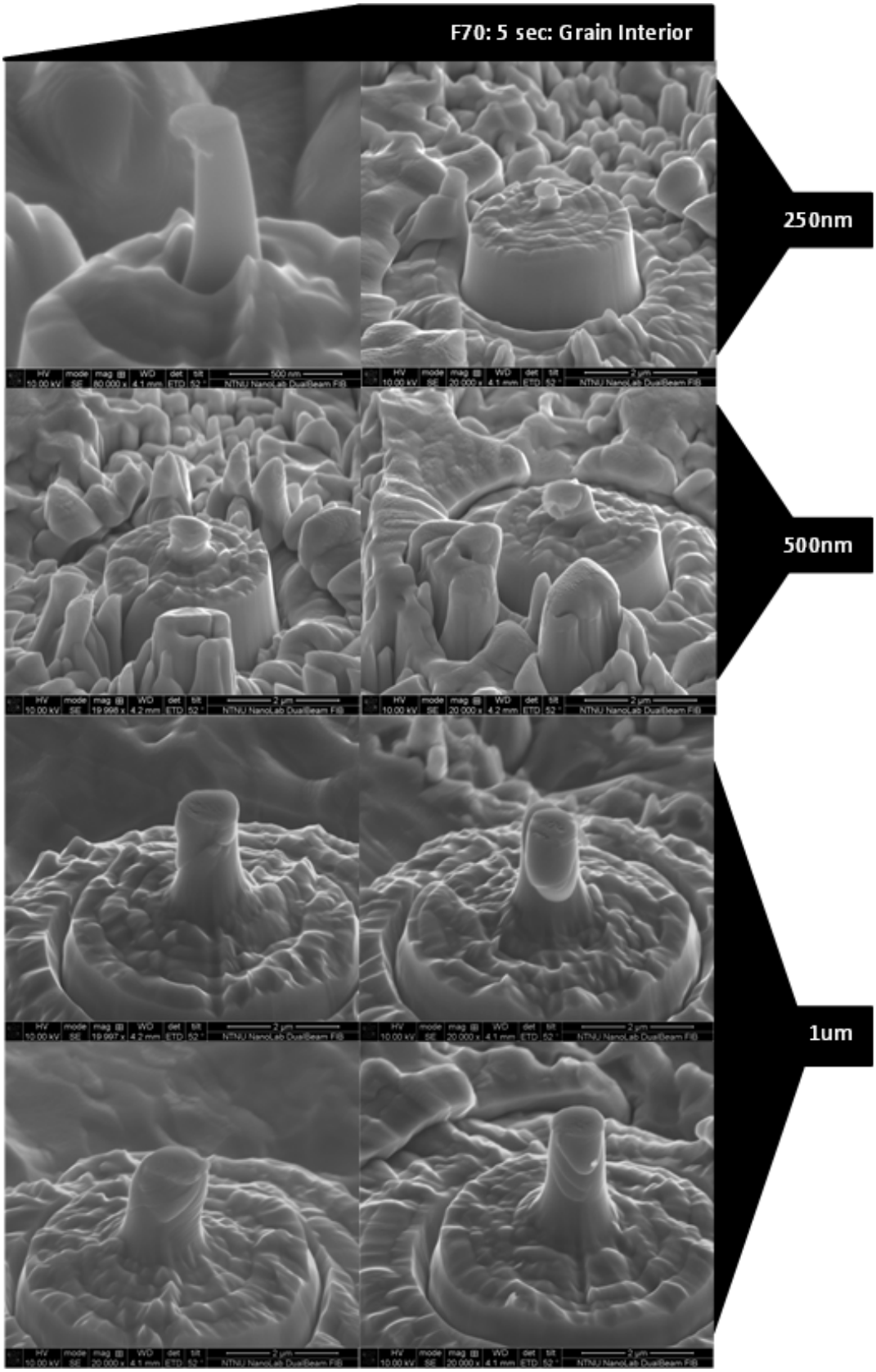
F70: 5 sec: Grain Interior
250nm
500nm
1um

Chapter 8

Appendix 4: EU: Pillar Deformation

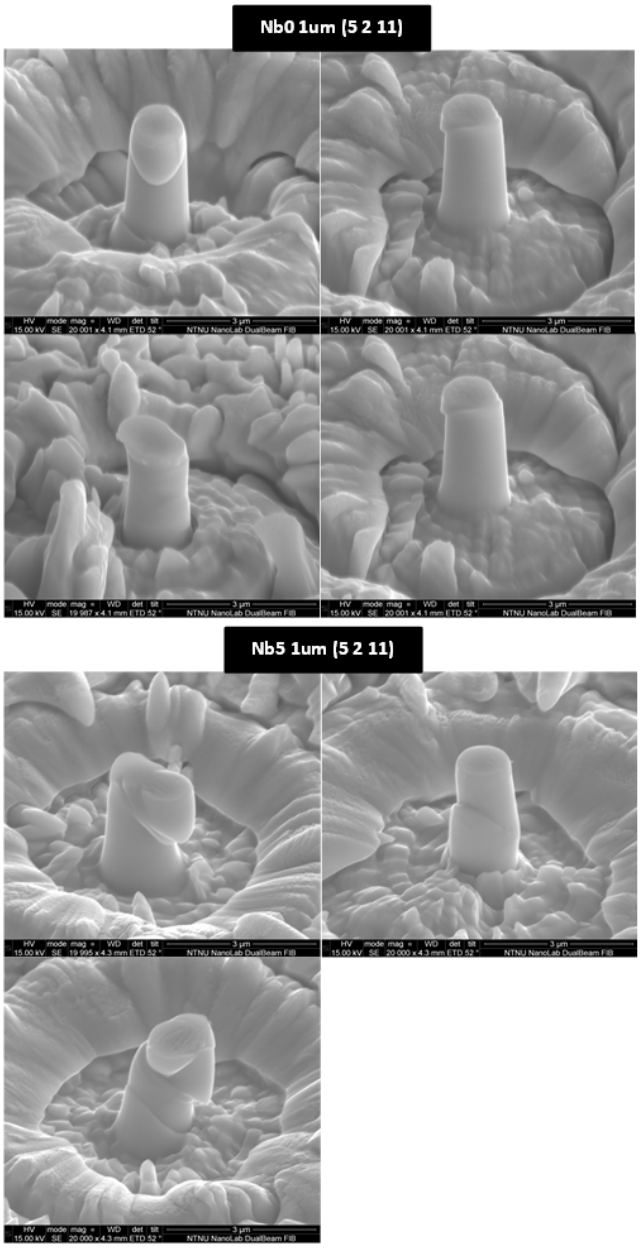

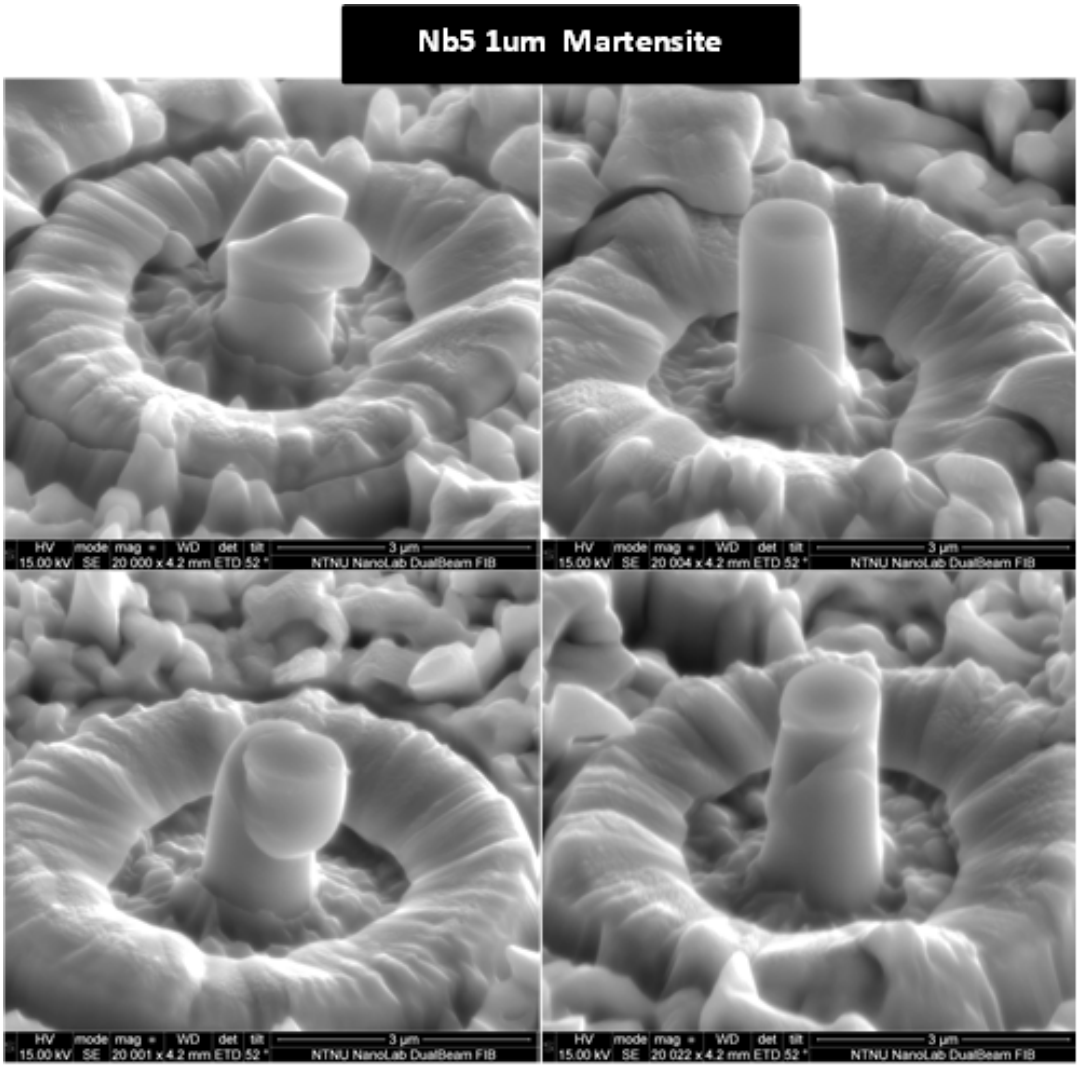
Nb5 1um Martensite
HV mode mag WD det tilt 3 µm
15.00 kV SE 20 000 x 4.2 mm ETD 52 ° NTNU NanoLab DualBeam FIB
HV mode mag WD det tilt 3 µm
15.00 kV SE 20 004 x 4.2 mm ETD 52 ° NTNU NanoLab DualBeam FIB
HV mode mag WD det tilt 3 µm
15.00 kV SE 20 001 x 4.2 mm ETD 52 ° NTNU NanoLab DualBeam FIB
HV mode mag WD det tilt 3 µm
15.00 kV SE 20 022 x 4.2 mm ETD 52 ° NTNU NanoLab DualBeam FIB

Bibliography

[1] A. M. M. O. M.P. Ariza, E. Tellechea. Double kink mechanisms for discrete dislocations in bcc crystals. California Institute of Technology (2012).

[2] l.Bortoloni et al. Statistically stored dislocations in rate-independent plasticity. EMIS (2000).

[3] N. F. Kostas Danas, Vikram Deshpande. Discrete dislocation dynamics and strain gradient formulations: a way to model size effects in plasticity. UPMC (2010).

[4] W. C. J.R.Greer, Christopher R. Winberger. Comparing the strength of fcc and bcc sub-micrometer pillars: Compression experiments and dislocation dynamics simulation. Elsevier (2007).

[5] V. G. Haugen. Nanomechanical testing of the heat affected zone of steel. Internal NTNU (2011).

[6] C. H. Ersland. Modeling of size and strain rate effects in compression tests of iron nanopillars. PhD thesis, Department of Engineering Design and Materials, Norwegian University of Science and Technology, (2012).

[7] W. C. C.R. Weinberger. Surface-controlled dislocation multiplication in metal micropillars. PNAS (2008).

[8] A.S.Schneider. Influence of orientation on the size effect in bcc pillars with different critical temperatures. Elsevier (2011).

[9] F. G. A. A.S.Schneider, B.G. Clark. Effect of orientation and loading rate on compression behavior of small-scale mo pillars. Elsevier (2009).

[10] B. C. P. G. E. A.S.Schneider, C.P. Frick. Influence of orientation on the size effect in bcc pillars with different critical temperatures. Elsevier (2010).